Three Dimensional Investigation of Hydrate Formation in Natural Gas Pipelines

Dissertation

Submitted to the Department of Mineral Resources and Petroleum Engineering and the Committee on Graduate Studies of Montanuniversität Leoben, Austria In Partial Fulfilment of the Requirements for the Degree of Doktor der Montanistischen Wissenschaften

Author:

Muhammad Naseer

Supervisor:

A.o. Univ.Prof. Dipl.Ing.Dr. Wilhelm Brandstätter

May,2012

Dedication

To my parents who instilled in me a passion to improve always, to my wife who has always been understanding and supportive during my tenure here and to my daughters Musabbeha and Haadya.

Affidavit

I declare in lieu of oath, that I wrote this thesis and performed the associated research myself, using only literature cited in this volume.

Muhammad Naseer

Abstract

Gas hydrates can undermine the flow assurance programs by blocking the pipelines. The stoppage in the production results in wastage of time and resources. A gas pipeline may pass through regions with topographic variations and elevation differences. In winters the ground temperatures may fall resulting in colder pipelines walls. If water vapour concentration in the natural gas mixture is such that temperature of the gas at the walls falls below the saturation temperature, condensation of water vapour may ensue. The condensed water flows along the pipe and tends to accumulate at the bottom section of the pipe. In addition to being accumulated at the bottom section of the pipeline, the water also gets entrapped at the sagging/ uphill sections, or trap-like portions of the pipelines. During the winter season, the deposition may be at different sections along the pipeline separated by large distances. The deposits may be circumferential and axial, reducing the effective flow rate of the gas. At the start of summers or during transient pipeline operations, the deposited hydrates may sloughen at the walls and travel along the pipe to eventually get trapped at pipe bends (for example) plugging the cross-section completely. The deposition in this manner has an appearance of packed ice [1].

While one dimensional (1-D) Computational Fluid Dynamics (CFD) codes can identify the hydrate prone zones along the length of the pipeline, the effects of condensation, hydrate formation and deposition along axial-radial directions (growth morphology) can only be ascertained with a three-dimensional (3-D) analysis. However, hydrate formation, deposition and blockage are complex multifaceted phenomena and require a synergistic approach, including various submodels to capture the whole phenomenon in totality. The work presented is an effort to model the mechanisms that lead to hydrate formation so that temporal and spatial phenomena related to hydrate formation can be understood. This in turn can help to ascertain critical sections of the pipe line with respect to hydrate deposition and blockage.

Kurzfassung

Gashydrate sind Einschlussverbindungen (Clathrate), die aus verschiedenen Gasen und Wasser bestehen. Sie sind fest und weisen eine Eis ähnliche Struktur auf. Methangashydrate können in kalten Regionen in Produktionsanlagen gebildet werden und unter Umständen die Flow Assurance, d.h. die Kontinuität der Förderung beinträchtigen. Im schlimmsten Fall werden durch Gashydrate Piplinesektoren blockiert und die Produktion kommt zum Stillstand.

Gaspipelines verlaufen meist über Hunderte von Kilometern durch verschiedene Geländeformen, die Höhenunterschiede aufweisen. Am Beginn der Hydratbildung steht die Kondensation von im Erdgas befindlichem Wasser. In der kalten Jahreszeit können die Wandtemperaturen unter die Tau punktstemperatur des Erdgases fallen und begünstigt durch den in der Pipeline vorherrschenden Druck kann die Kondensation von Wasser einsetzen. Dieses Wasser sammelt sich dann in den tieferen Bereichen einer Pipeline zwischen fallenden und aufsteigenden Leitungsabschnitten. In diesen Bereichen, die oft große Distanzen von einander entfernt sein können, kann nun Hydratbildung einsetzen. Die entstehenden Hydrate lagern sich zunächst sichelförmig und in weiterer Folge ringförmig entlang der Piplinewände an. Sie bewirken damit eine Reduktion des Leitungsquerschnittes und führen daher zu einer Verringerung der Produktionsrate.

Wenn zu Sommerbeginn die Temperaturen wieder ansteigen oder während transienter Förderprogramme können sich die an den Wänden abgelagerten Hydrate ablösen und mit dem strömenden Gas weiterbewegen. Dadurch besteht die Gefahr, dass feste Hydratgebilde in gewissen Sektionen einer Pipeline (z.B. in Rohrkrümmern) akkumulieren und diese vollständig blockieren. Dies kann einen Totalausfall der Produktion bewirken.

Ziel der vorliegenden Arbeit war es, die bei der Hydratbildung auftretenden Prozesse in einem Simulationsmodell abzubilden und ein tieferes Verständnis für die dabei ablaufenden komplexen physikalischen Phänomene zu entwickeln. Die in der Leitungssimulation häufig verwendeten eindimensionalen (1D) Modelle erlauben lediglich die Identifikation von Sektionen innerhalb einer Pipeline in denen die Gefahr von Hydratbildung besteht. Diese Modelle versagen jedoch, wenn das Wachsen der Hydratzone in Piplinequerschnitten und in der Strömungsrichtung simuliert werden soll. Daher wurde erstmals versucht mit

Hilfe von instationären dreidimensionalen (3D) Simulationen mehr Licht in den Vorgang der Methanhydratbildung zu bringen. Die Modellierung der Bildung und Ablagerung sowie gegebenenfalls die Blockierung von Leitungsabschnitten durch Hydrate erfolgte dabei mit Hilfe von Sub-Modellen, die in ein kommerzielles Computational Fluid Dynamics (CFD) Programm integriert wurden. Aufgrund des enormen Rechenaufwandes und der vorhandenen Computerkapazitäten war die Berechnung von Blockierungsvorgängen in Pipelines durch Hydrate nur eingeschränkt möglich. Die Simulationen betreffend Bildung und Wachsen von Hydraten ergaben jedoch neue Erkenntnisse, die in der Arbeit ausführlich beschrieben werden.

Acknowledgements

I would like to highly appreciate and acknowledge **Professor Wilhelm Brandstätter** for giving me an opportunity to carry out research in the field of Computational Fluid Dynamics. His diligent, consistent supervision made it possible for me to achieve this feat. His huge breadth and depth of knowledge always helped me steer in the right direction. He has always demonstrated patience and encouraged me to develop my skills. He has also always supported me regarding any problem that I have shared with him. I cannot find enough words to thank him

I like to thank **Professor Herbert Hofstätter** for showing his concern and providing an open and friendly environment required for the research. I would like to thank **Professor Ruthammer** for his painstaking efforts to ensure liaison with the industry in order to provide an input. I thank my colleagues **Petr Vita, Gebhard Kastner, Ries Bouwman, Johannes Leixnering, Claudia Gruber** and **Michael Klug** to provide their ever ready help through their expertise and cooperation. I also acknowledge the efforts of **Miss Irene Jauck** for her help and support regarding administrative matters. I would avail the opportunity to thank OEAD Austria for the efforts regarding the administrative aspects. Last but not the least, I thank my wife **Sobia** for being supportive and understanding and my daughters **Musabbeha and Haadya**.

Contents

List of Figures

List of Tables

Chapter 1

Overview

1.1 Historical preview

Continuous uninterrupted supply of natural gas through onshore and offshore pipelines is the job of production engineers. One of the things that pose problems to the flow assurance programs is the formation of natural gas hydrates in pipelines. They may reduce the effective cross-section areas of a pipeline at various places along the length or may completely block. The formation of hydrates in natural gas pipelines may result in damage to equipments and injury to personnel [1]. For any kind of solution related to hydrates, first of all it is necessary to have an idea on the conditions which lead to hydrate formation.

In the mid 30's, the problem was identified by Hammer Schmidt in the natural gas industry [7]. The natural gas hydrates were known to exist in nature before that. Since the discovery of hydrates there have been many efforts to circumvent the hydrate formation problem. Just after the discovery of hydrates, the thrust of research was doing lab experiments in controlled environments to determine the thermo-physical characteristics and to identify different structural arrangements of hydrates [7]. Due to more exploration and improved methods in the gas industry in addition to the increased demand, the gas suppliers were going to operate at higher pressures. Operating at higher pressures has associated problems that appear with it. Natural gas hydrates usually are formed at high pressures and low temperatures if sufficient water is present in the pipelines [7, 13]. If the natural gas stream has a high fraction of water vapour in it, then condensation might occur in the pipeline, where the temperature of the pipeline falls below the dew point of the water vapour. It is much likely that the condensed water may accumulate at the lowered sections of pipelines and if the temperature and pressure conditions are right, the hydrate nucleation may start.

Natural gas hydrates are not chemical compounds but consist of a 'guest' molecule (usually a lighter gas molecule) entrapped in a structure formed by the hydrogen bonded water molecules. The name 'Clathrate hydrates' comes

from the word 'clathratus' which means to encage. Physically, hydrates resemble ice, and have similar physical properties, but hydrates can form well above the freezing point of water at higher pressures. Hydrates are non-stoichiometric and the hydrate formation phenomenon is a complex process to capture in its entirety. There are many phenomena accompanying hydrate formation which makes it very difficult to ascertain the hydrate formation phenomenon.

In gas pipelines the primary hydrate formation may be deposition along the walls of the pipeline but the site of hydrate blockage may not be the same as the initial deposition. It is asserted by many experts that the hydrate deposited in the gas pipe walls may sloughen due to transient pipeline conditions. The loosened hydrate may travel along the pipe until it finds a certain natural obstacle in the pipeline (due to abrupt change in pipe direction). The resulting blockage finally appears to be packed snow [1, 14].

Different scientists and researchers have focused on different aspects of hydrate formation. The formation and decomposition kinetics of hydrate formation was addressed by Bishoni et. al. [15] at conceptual level. The work highlighted different stages of hydrate formation and growth. An excellent paper by Riberio et. al. [16] gives a critical review of the modelling efforts by different researches to address the hydrate formation and decomposition kinetics. Nicholas et. al. [17] proposed a hydrate deposition and plugging model in gas dominated pipelines and asserted that the mechanism of hydrate plugging inside them is entirely different from that of oil dominated systems. Jassim et al. [18] developed a model based on particle dynamics theory to address hydrate particle migration and deposition. Balakan et al. [19] studied the Freon R11 hydrate deposition in a turbulent flow of water and compared the experimental data with Computational Fluid Dynamics (CFD) results. To ascertain the feasibility of natural gas production from hydrate deposits in nature, Ahmedi et al. [20] proposed a one-dimensional model for hydrate decomposition by depressurisation. The flow characteristics of hydrate-water slurry were studied by Gong et al. [21] and factors influencing mass transfer and growth of hydrate crystals were also discussed. Industrial scale flow loops were setup by ExxonMobil Upstream Research Company and at Tulsa University to actually monitor different hydrate formation parameters during real flow conditions [22, 23]. Davies et. al. [24] developed a hydrate formation model based on a hypothetical/conceptual picture of hydrate formation in pipelines and validated their computational results with data derived from the aforementioned flow loops.

1.2 Areas of Hydrate Research and Development

Presently, hydrate research is being carried out in different areas. The motivation for research of each particular area is different. Given below is a general

classification of the hydrate research areas:

- Hydrates in oil and gas industry (avoidance, risk management, remediation)
- Gas hydrates in nature
- New applications
- Environmental issues (green house effect, determination of ancient earth environment)

1.2.1 Hydrates in the Oil and Gas industry

Hydrate formation is a very serious problem in the oil and gas industry since blockage of gas pipelines can translate in to a lot of economic loss in addition to posing threat to the personnel. The flow assurance programs initially aimed at total hydrate avoidance by controlling the pressure and temperature conditions. With more and more exploration, the pipelines had to be operated at higher pressures so total hydrate avoidance became expensive and impractical. Modern methods make use of chemicals that either delay the hydrate formation (thermodynamic inhibition) or inhibit the agglomeration of hydrates so that they flow in form of slurry (kinetic inhibition). If the hydrate plugs form in the pipelines, then remedial measure have to be taken to remove the blockages by various methods. Figure 1.1 shows a hydrate plug removed from a pipeline section.

Figure 1.1: Hydrate blockage in oil and gas pipelines [2]

1.2.2 Gas hydrates in nature

With the discovery of hydrates in earth's permafrost region, geological surveys and estimates show large amounts of hydrocarbon gases entrapped (see figure 1.2 a). The estimated hydrate reserves have a wide range (the range of estimates grew from 2×10^{14} to 1.2×10^{17} between 1990-2005) [7]. However, even with the lower side of the estimates, hydrates seem to be the solution of the energy problems of the world. A maximum of about 184 volumes per unit volume of hydrate are possible [7]. Figure 1.2 b shows an example of the hydrocarbon content of hydrates. The issues hindering the rapid development are unknown environmental effects (due to greenhouse gases), effects on the settlement of the earths crust (once the cementing provided by hydrates is removed) and the research regarding hydrate kinetics and thermodynamics (which is still undergoing) before huge capital is invested on (full throttle) energy production from hydrates.

(a) (b)

Figure 1.2: (a) Hydrate on ocean floor, (b) Burning Ice [2]

1.2.3 New Applications

With the increase in the knowledge of hydrate physical and time dependent properties new applications of gas hydrates for useful purposes are emerging. A few applications of hydrates are described below:

1.2.3.1 Transportation and Storage of Natural gas

As the hydrogen bonded water molecules encapsulate the gas molecules, hydrate provides natural storage for the gas. Gas storage in this form is energy

and space efficient. Methane hydrate for instance has an energy density equivalent to a highly compressed gas [7]. Natural gas can be transported in form of hydrates and there have been studies indicating the economic viability of the natural gas hydrates as a replacement to the conventional, compressed natural gas transportation mode [25, 26].

1.2.3.2 CO_2 separation from flue gas

Various studies have been done regarding the CO_2 separation from the flue gas using the hydrate formation. The fact that CO_2 can be captured in the hydrogen bonded structure of hydrates initiated an interest in this direction as the CO_2 hydrates can be formed at lower pressures and higher temperatures (compared to hydrates of hydrocarbon gases). These studies have been done to determine the economic viability of the process in order to limit the release of the green house gas to the environment [27,28]. Figure 1.3 shows a conceptual picture of the process, where flue gas is bubbled through chilled water and CO_2 is captured from the mixture in form of hydrates.

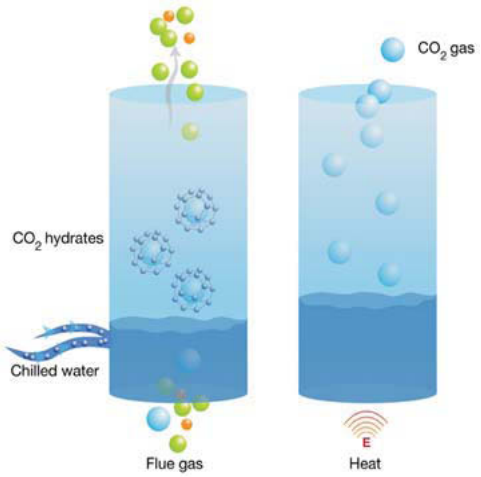

Figure 1.3: CO_2 removal from flue gas [3]

1.2.3.3 Excess electrical energy storage

The use of hydrates as means of electrical energy storage has been widely investigated. During the hours of the day when excess electrical energy is available (but not being used), the excess energy can be used to form hydrates. During the hours of peak load, energy can be obtained by endothermic melting of hydrates [7].

1.2.3.4 Sea Water De-salination

The principle involves mixing sea water and gas to form hydrate and thick brine slurry [7]. The hydrated water is thus devoid of salt. The process has been studied with economic viability perspective by many researchers [7, 29].

1.2.4 Environmental issues

Hydrates are also naturally present in the earth's crust, beneath deep oceans (see figure 1.2 a) and in the permafrost regions since millions of years. Research suggests that water depths of 300-800m are sufficient to stabilize (with respect to pressure and temperature) the hydrates. Inside oceans, natural gases (primarily methane) are present near the sea floor as a result of bacterial activity (methanogenesis), the gas present in the low temperature environment under high pressure gets converted to hydrates [7,13]. One of the issues that is hindering the rapid exploration and extraction of natural gas from the subsea reserves is that methane is a green house gas and its excess release in to the environment during drilling can cause harm to the environment. Moreover there is evidence that the hydrate formed provide cementing for the ocean floor, thus release of methane can destroy the natural cementing causing land slides for the slope regions of the ocean floors [4].

Figure 1.4 shows (hydrate) cemented zone of the ocean floor. If the gas is released, it can escape to the atmosphere with potential harmful environmental effects and furthermore there is a probability of landslide in the (unstabilized) slope planes as depicted in the figure.

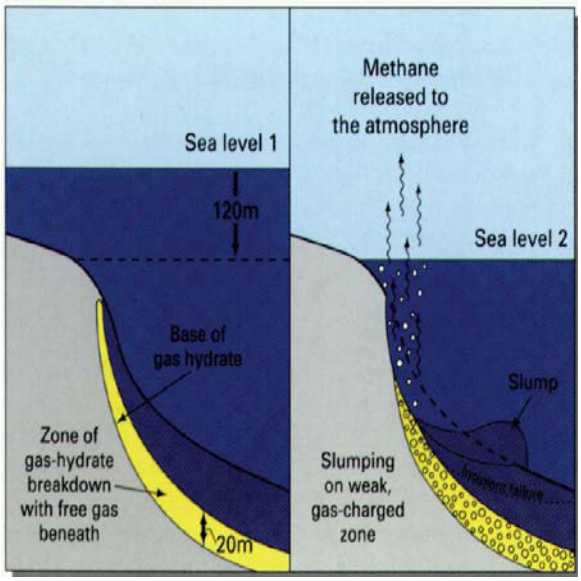

Figure 1.4: Risks of methane release to atmosphere and landslides [4]

1.3 Thesis Outline

This thesis is organised in a way to touch all the areas of basic knowledge before model development is discussed. Chapter 1 gives a historical overview of hydrates and discusses various aspects of hydrate research and development. Chapter 2 contains a theoretical overview of hydrates with the description of hydrates starting from the molecular level, including hydrate properties to the macroscopic behaviour of hydrates. Chapter 3 contains the nucleation theory and thermodynamic derivations for the model development. Chapter 4 delineates the Computational Fluid Dynamics (CFD) methodologies to form an algebraic system of equations and their solution strategies. Chapter 5 describes the model development, results and discussion. Chapter 6 lists the conclusions and an scope for future development.

Chapter 2

Introduction

2.1 What are hydrates?

Hydrates are mixtures of water and gases in a way that the resulting mixture takes the form of crystalline solid. The word 'clathrate' is from 'clathratus' which literally means 'to encage'. In Clathrate hydrates, guest molecules get entrapped in the hydrogen bonded water molecule structure. The guest stabilises the cage of water molecules, which surround the guest due to the hydrogen bonding between them. Typical lighter natural gases such as methane, ethane, propane and carbon dioxide are known to form hydrates more easily than the heavier gases (with higher molecular weights) [7]. A conceptual picture of a guest molecule entrapped in a cage formed of water molecules is shown in the figure 2.1.

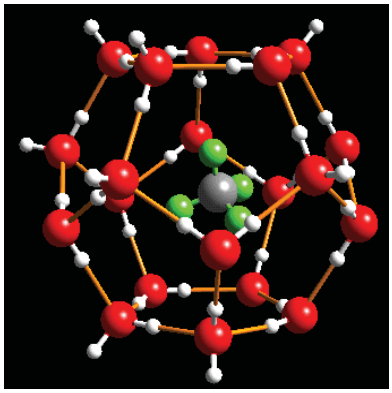

Figure 2.1: Guest molecule trapped inside cage of water molecules [5]

2.2 Hydrate Structures

2.2.1 Crystalline Structure

Hydrates exhibit crystalline structure similar to ice. The H_2O molecules form hydrogen bonds with each other, with the gas molecule as the stabilizing agent. The H_2O molecule arrange themselves in such as way that a hydrogen atom is in between two oxygen atoms (and has covalent bond with one and hydrogen bond with the other). In this way, each water molecule is linked to four water molecules in a fashion as depicted in figure 2.2.

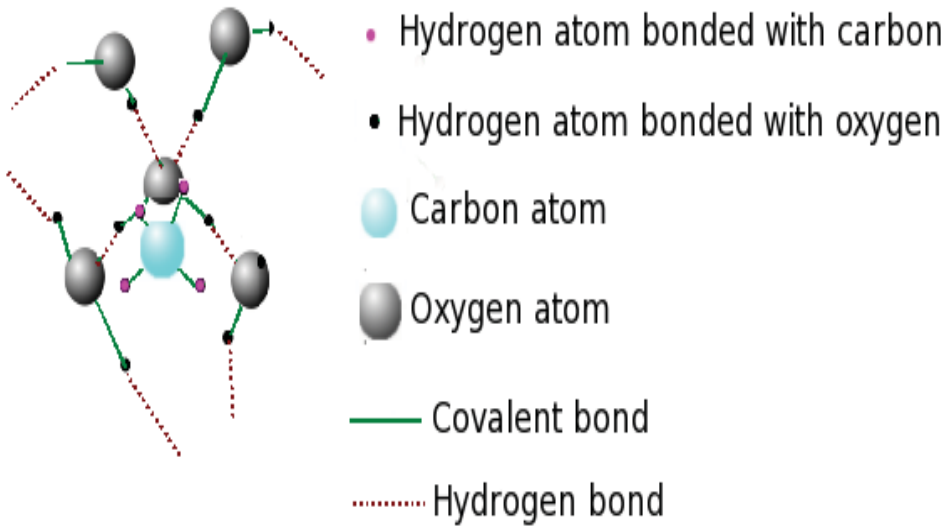

Figure 2.2: Crystalline arrangement of water molecules in hydrate

Due to the crystalline arrangement, the H_2O molecules in hydrate (solid form) are farther apart from the (same number of) H_2O molecules in the liquid state and hence there is an increase in volume of the hydrated bulk. Under suitable conditions of pressure and temperature, a hydrophobic gas may assist (and accelerate) the crystalline structure formation. The pattern continues in a repetitive manner in three dimensions resulting in gas molecules being entrapped in the cages formed by hydrogen bonded network of water molecules as depicted in figure 2.3.

It is important to mention here that only a small number of cages are filled in by gas molecules and most of the cages are empty. The cages of water molecules may share faces (or molecules) so that in a bulk of hydrate solid, there is a continuity of interconnected networks of hydrogen bonded water molecules.

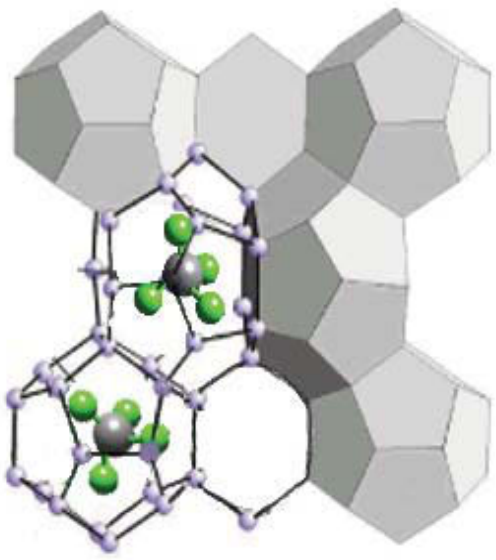

Figure 2.3: Repitive array of crystalline arrangement [6]

2.2.2 Hydrate cavities

The majority of work on hydrate structures was done by Jefferey, McMullan, Davidson, Ripmeester, Udachin, Mehta, and Mooijer-van den Heuvel [7]. The hydrate structures have been broadly categorised in to structure I, structure II and structure H, based on the specific combination of different type of cavities. The different hydrate structures are formed by the combination of five polyhedra. The most common types are pentagonal dodecahedron 5^{12}, tetrakaidecahedron $5^{12}6^2$, hexakaidecahedron $5^{12}6^4$, irregular dodecahedron $4^3 5^6 6^3$ and icosahedron $5^{12}6^8$ structures. The method for the description of these polyhedra was proposed by Jeffery. Polyhedra 5^{12} represents cavity formed by 12 pentagonal faces whereas $5^{12}6^2$ represents cavity formed by 12 pentagonal and two hexagonal faces. Figure 2.4 [1, 7] describes the structures I, II and H by combination of these cavities.

From the figure, it is clear that for a unit (lattice) cell of structure I (for example), there are two (02) 5^{12} cavities and six (06) $5^{12}6^2$ cavities. It means that a maximum of eight (08) gas molecules can accommodate a unit cell which have sizes small enough to fill the cages and big enough to stabilize them (otherwise the cages would collapse). In a similar manner, maximum possible accommodation for structure II and structure H hydrates can be ascertained. A general formula for the structure I hydrates (unit cell) would be:

$$8G + 46H_2O \Leftrightarrow \ 8G.46H_2O$$

The structure I unit lattice is formed of eight (08) hydrate building units (eight cages all assumed to be filled with gas). The formula for a single hydrate

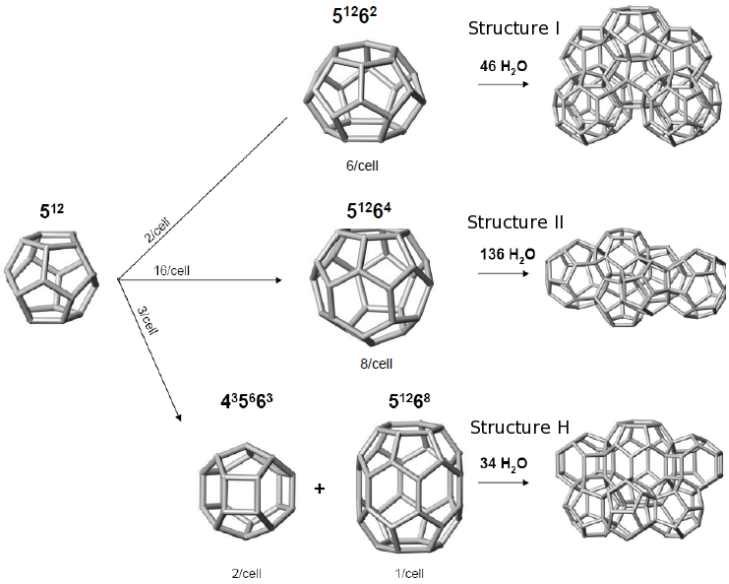

Figure 2.4: Hydrate structure with combination of cavities [7]

building unit would look like:

$$G + 5.75H_2O \Leftrightarrow \ G.5.75H_2O \tag{2.1}$$

Similarly, formulae for structures II and structure H can be worked out easily. The number '5.75' here is the hydration number for structure I hydrates, and tells us the water molecules consumed per hydrate building unit. The equation in the form of equation 2.1 is useful when dealing with the thermodynamics of the reactions to form hydrates. On the same lines, a generalized equation would look like:

$$G + n_wH_2O \Leftrightarrow \ G.n_wH_2O$$

where n_w represents the hydration number.

It is important to emphasize the role of the guest molecule in hydrate structure. Natural gas molecules (guests) are generally 'hydrophobic' and do not form any bond with the water molecules, rather they are free to rotate inside the cavities. The role of guest molecules is just to stabilise the hydrate structure. Most commonly found structures of hydrates are structure I and structure II. Structure I is usually found in nature (for example methane hydrates beneath oceans), whereas in natural gas industry almost in all the cases the hydrates formed are structure II hydrates [1]. The most optimal guest to host ratio is between 0.84 and 0.98 (by volume) and any amount of larger molecule (such as propane and butane) converts the structure I hydrate instantaneously to structure II [7]. As in the natural gas and oil industry there are always heavier components of the gas present, therefore structure II hydrates

are found in all the cases. Structure H hydrates have very extreme conditions of formation (forms at extremely high pressure) so there is very rare chance of the formation of structure H in the natural gas industry.

The structure-I, structure-II show cubic lattice arrangement and structure-H shows hexagonal lattice arrangement in the bulk.

Modern day high-tech computer simulations can also be used to ascertain the specific lattice arrangement of different hydrate structures. Figure 2.5 shows some instantaneous snapshots of molecular dynamics computer simulations.

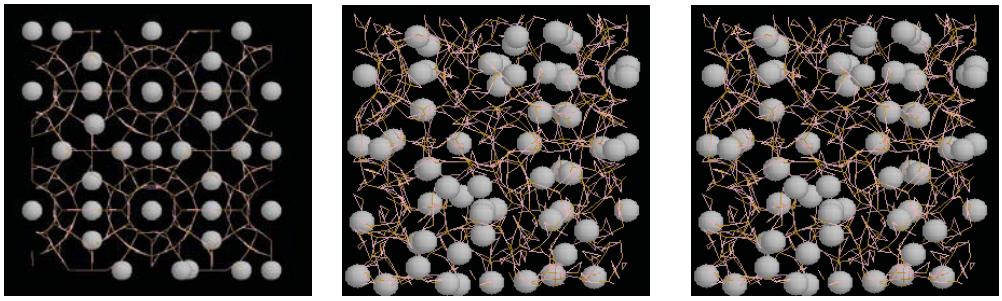

(a) (b) (c)

Figure 2.5: Hydrate structure as a result of computer simulations (M. Walsh, CHR., Colorado School of Mines [7])

The figure 2.5 (a) shows the final result of the Molecular Dynamics (MD) simulation if hydrate formation from an initial liquid and gas phases is computed. The picture shows clearly the arrangement of gas and water molecules in structured lattice form. Figures 2.5 (b) and 2.5 (c) show the water and (diffused) gas molecules in disorderly pattern.

In the MD simulation methodology, initially, a fixed number 'n' of water molecules is placed in a computational cell of fixed volume 'V'm^3 [30]. The atomic arrangement of water molecule is fully represented for each water molecule. Moreover the effect of all the inter-moleculer and intra-molecular forces (e.g Coulomb, short range, van der Waals et.) are incorporated in the model. The computational cell is under fixed pressure and temperature (with in hydrate equilibrium zone). The calculations are carried on until the water molecules achieve equilibrium (with respect to the orientation). In the next step, 'm' gas molecules (guest) are placed inside the previously equilibriated water molecules (and some water molecules are removed from the positions where guest molecules are inserted). The calculation is carried out again until equilibrium is achieved. The final results shows cages of hydrogen bonded water molecules enclatherating the gas molecules.

2.3 Hypotheses regarding Hydrate Initiation

The molar composition of hydrates indicate that hydrates are about 85 mole percent water and 15 mole percent gas. The solubility of natural gases in the water is extremely low and also the water molecules in the gas stream may be extremely low for the hydrate formation. Its is argued by Sloan [1, 7] that the most probable site for the formation of natural gas hydrates is the gas water interface. However, according to Dimo Kashchiev et. al [31] even though at their incipience, the hydrates are observed at the gas water interface, there is a probability that the hydrate is formed just in the (gas-water) solution adjacent to the gas-water interface, moreover, in dynamic fluid systems, the hydrate formed at the interface (or just beneath it) may be transported in to the bulk liquid due the effects of convection and diffusion. There are in general three hypotheses regarding hydrate nucleation addressing the possibilities of hydrate formation positions. [7].

- Labile cluster nucleation hypothesis [7, 32, 33]
- Local structuring hypothesis [34]
- Nucleation at interface hypothesis [7, 35]

All three of these hypotheses assisted with the modern experimental techniques, molecular dynamics simulation etc. were developed to describe the initiation and positioning of the nucleation phenomena. The labile cluster nucleation hypothesis asserts that there are unstable (very short lived $\sim 10^{-9} sec$) structures (pentamer, hexamers etc.) which exist in the bulk of water all the time, which form and disintegrate continuously. During an event in which a guest molecule (such as dissolved hydrocarbon gas molecule) comes in the vicinity of these structures, they arrange themselves around the guest and attain stability if critical size is achieved.

Local structuring hypothesis rejects the notion of labile cluster hypothesis and describes the structuring of water molecules as local to the guest (hydrocarbon) molecules only. The hypothesis states that for very low solubility of hydrocarbon gases, the water molecules only start forming branched structures (e.g pentamers, hexamers) in the vicinity of the dissolved molecules in order to attain equilibrium. This structuring is thus only localized to the position of the dissolved water molecule.

Nucleation at interface hypothesis is schematically shown in figure 2.6;

It states that the nucleation process starts by a guest molecule (of a hydrophobic gas) approaching the gas water interface, and then it is adsorbed on to the surface of water such that water molecules start arranging themselves in an orderly fashion around the guest. Any hydrate formation process starts at the gas-water interface and the formed hydrate then can be transported to any position in the bulk water by diffusion or convection.

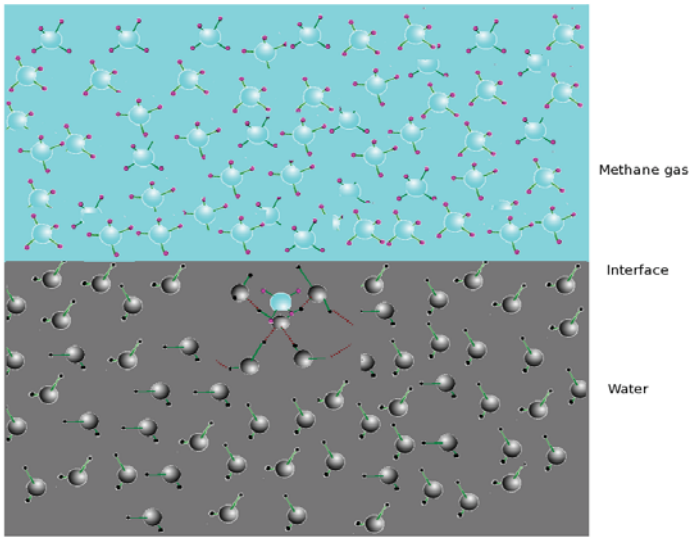

Figure 2.6: Adsorption of gas molecules on the surface [1]

2.4 Hydrate properties

There have been big efforts to ascertain hydrate properties in order to predict and exploit the behaviour of hydrates in flow assurance, energy and other industrial applications. The properties of prime interest have been density, elasticity, electrical resistance, heat capacity and heat of formation.

2.4.1 Density of Gas Hydrates

The method to determine the density of hydrates is dependent on spectroscopic techniques. Knowledge of hydrate lattice parameter 'a', filling ratios of the cavities by guest molecules (α_1 and α_2) and molecular mass of the guest 'M' is necessary. Mathematically [13]:

density of structure I hydrate:

$$\rho^I = \frac{(46H_2O + 6M\alpha_1)(1/N)}{a^3} \tag{2.2}$$

density of structure II hydrates:

$$\rho^{II} = \frac{(136H_2O + 8M\alpha_2)(1/N)}{a^3} \tag{2.3}$$

In the above equations 'N' represents the Avogadro's Number.

The formula gives good results for hydrates at equilibrium pressure at temperature of 273 K. For higher pressures and temperatures the density can be determined from the general formula [13];

$$\rho = \frac{\sum M_{hi}}{\sum V_i 18 n_i} \tag{2.4}$$

where 'M_{hi}' represents the molecular weight of the hydrate of i-th component, 'V_i' is the specific volume of water in a hydrate state, 'cm^3/g' and 'n_i' is the ratio of the water molecules to the number of i-th component gas molecules. The expression for the ratio 'n_i' for structure I and structure II are given as;

for structure I [13],

$$n^I = \frac{23}{\sum \Theta_1 + 3\sum \Theta_2} \tag{2.5}$$

for structure II [13],

$$n^{II} = \frac{17}{2\sum \Theta_1 + \sum \Theta_2} \tag{2.6}$$

where 'Θ_1' and 'Θ_2' are the filling ratios of small and large cavities in the hydrate lattices respectively.

2.4.2 Heat of Hydrate Formation

For engineering purposes, the method to find the heat of hydrate formation is by using Clausius-Clapeyron equation. Mathematically [7]:

$$\frac{dlnP}{d(1/T)} = -\frac{\Delta H}{zR} \tag{2.7}$$

where 'z' is the compressibility factor of the gas at the hydrate formation conditions and 'R' is the universal gas constant. The semi-logarithmic plots of hydrate formation pressure and inverse of corresponding temperatures can be found in literature and for a wide range of temperatures (see figure 5.4). Once the slope of the graph is determined, heat of hydrate formation can be determined using equation 2.7.

In general, hydrates are similar to ice in structure and hence have similar properties. A comparison of properties of structure I and structure II with that of ice is given in the table below;

No.	*Property*	Ice	St-I	St-II
1.	Poisson's ratio	0.33	0.31	0.31
2.	Bulk modulus (GPa)	8.8	5.6	8.5
3.	Shear Modulus (GPa)	3.9	2.4	3.7
4.	Linear thermal expansion at 200 K (K^{-1})	5.6E-5	7.7E-5	5.2E-5
5.	Thermal conductivity at 263 K (W/(m-K))	2.23	0.51	0.50
6.	Heat capacity (J/(kg-K))	1700	2080	2130

Table 2.1: General properties of hydrates [7].

2.5 Ascertation of Equilibrium Conditions for Hydrate Formation

Hydrates are generally formed under high pressures and low temperatures. From the time of the discovery of hydrates until today, the researchers have been devoted to understand the properties of hydrates and the conditions under which they form [7]. After the discovery of hydrates in the natural gas industry, the main thrust was to prevent the conditions which are conducive to the formation of hydrates.

2.5.1 Early Methods

All research activities aimed at identifying the pressure and temperature conditions of hydrate formation. The earliest attempt was by Hammerschmidt who published a summary of 100 hydrate formation data points [7]. Initial attempts to find out the hydrate equilibrium conditions led to the development of equilibrium charts for individual phases. However in the natural gas industry there is always a mixture of gases with varying composition and it is highly impractical to measure the data points for all the gases and their mixtures. Due to these difficulties, a team led by Katz [7] devised two methods (gas gravity method and K-factor method) in order to ascertain the hydrate equilibrium conditions. There were further attempts by Baillie and Wichert to account for the sour gas ('H_2S') which can cause accelerated hydrate formation. The methods developed are listed below:

- Equilibrium curves for individual phases
- Gas gravity method
- K-factor method
- Baille-Wichert method

2.5.1.1 Equilibrium Curves for Individual Phases

One of the methods to ascertain the equilibrium conditions for individual gases is the experimental determination of pressure, temperature conditions for hydrate formation. Figure 2.7 gives a depiction of pressure-temperature (equilibrium) curves for methane, ethane and propane. To the left of the curve for each particular curve, the pressure temperature states are conducive for the hydrate formation while to the right, the hydrates cannot form. The vertical line at 273.15 K is the ice formation line. The intersection of any curve with this line gives the lower quadruple point Q1. At this point, all the phases in equilibrium can co-exist. For example at Q1, the state might be H-I-Lv-V meaning hydrate, ice, liquid water and vapour. In the hydrate equilibrium

curves for ethane and propane, a second quadruple point indicates the presence of four phases co-existing in equilibrium i.e hydrate, liquid hydrocarbon, liquid water and vapour.

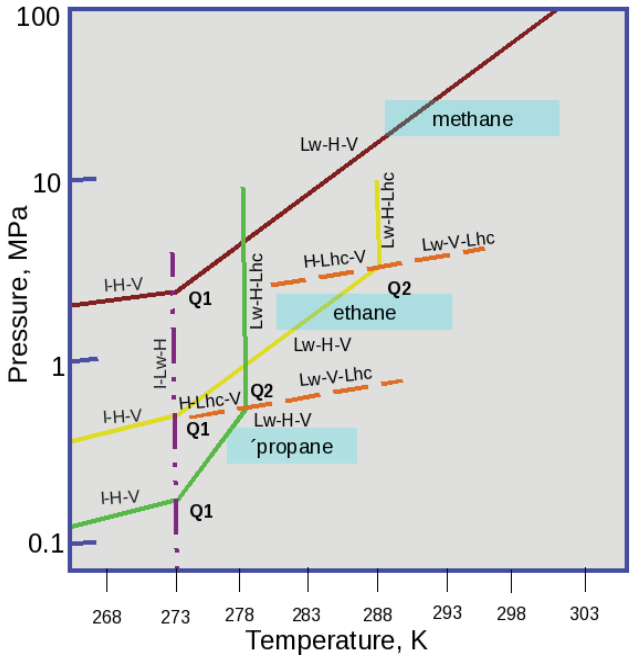

Figure 2.7: Pressure temperature curves for hydrates [7]

2.5.1.2 Gas gravity method

The simplest method that is still used today is the gas gravity method. The gas gravity method gives the equilibrium conditions based on the specific gravity of the gas (see fig 2.8). It is the simplest method to determine the equilibrium pressure, temperature conditions of a mixture of gases. As the gases ensuing from a gas well can have varying molar compositions, this method gives estimates of the equilibrium conditions. Gas gravity is determined by dividing the (average) molecular weight of the gas with the molar mass of air. Mathematically:

$$\gamma = \frac{M}{28.966} \tag{2.8}$$

where γ represents the specific gravity of the gas, M is the molecular mass of the gas mixture and the value 28.966 is the standard molar mass of air [36].

Once the gas gravity is determined, equilibrium conditions can be obtained directly determined from the chart (by reading pressure against temperature or vice versa). The original gas gravity chart was created only for the hydrocarbon

gases and can have errors if the gas mixture contains other non-combustibles gases in substantial amounts [7].

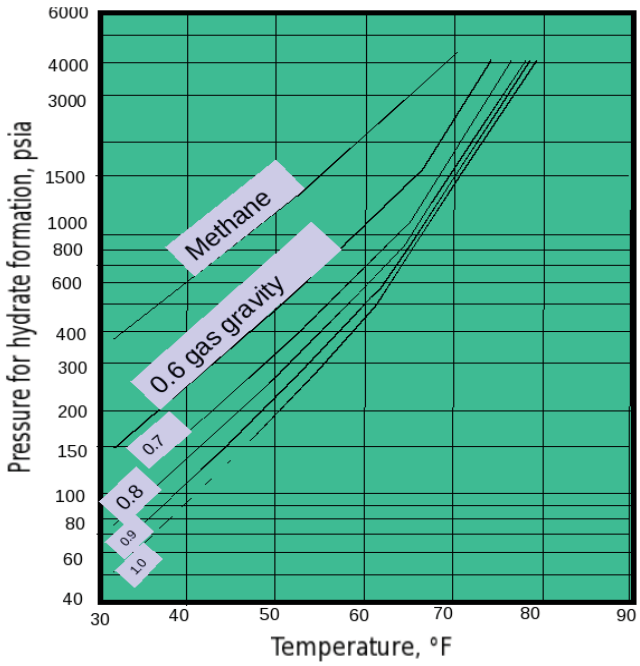

Figure 2.8: Gas gravity chart for estimation of hydrate formation [7]

Based on the gas gravity method, 'Hydrate Joule Thomson' charts were developed (see figure 2.9) for a number of different (gravity) gases to ascertain the 'expansion limit' (before hydrate formation) of the gases (during isenthalpic expansion) [7]. The basic aim of the charts was to ascertain the pressure limit during expansion (through chokes, orifices etc.) after which there is a possibility of hydrate formation. These Joule Thomson charts were created from Mollier charts for natural gases. During expansion of gases, pressure and temperature of gases usually decrease. The expansion curves were finally obtained by joining the intersection points of the isenthalpic expansion curve (starting at initial pressure and temperature) with the gas gravity equilibrium curve.

2.5.1.3 Distribution Coefficient (K factor) method

While the gas gravity method gives (an approximate) idea of the hydrate formation conditions for a specific composition of a gas, it does not give an idea of the composition of the hydrate formed for the gas mixture. A relatively more advanced method in this regard is based on the charts developed by Carson and Katz [36]. The charts help to determine pressure at given temperature or temperature given at pressure for a specific composition of a gas to start with.

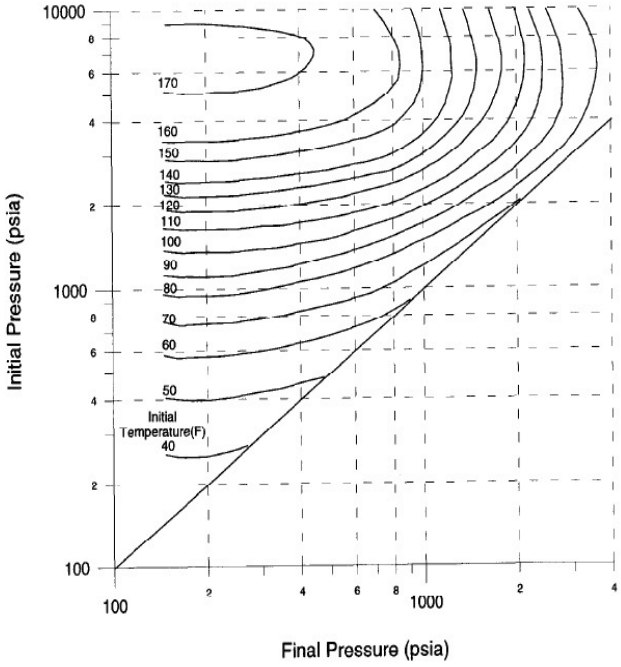

Figure 2.9: Joule Thomson limits to 0.6 gravity gas expansion [7]

Charts are available for each gas component e.g. methane, enthane, propane etc. which gives the factor 'K' as;

$$K_i = \frac{y_i}{s_i} \tag{2.9}$$

where y_i is the mole fraction of a ith component in gas and s_i is the mole fraction of ith component in hydrate. Given the temperature 'T' for instance, assumption is made about the pressure, and K_i is determined from the charts. As the composition y_i of a particular gas is known, the following equation is solved iteratively;

$$f(T) = 1 - \sum \frac{y_i}{K_i} \tag{2.10}$$

The equation is solved iteratively in order to seek f(T) = 0. If the temperature is known initially, a pressure value is assumed and K_i for each gas component is read from the 'K' charts and inserted in equation 2.10. The pressure guess is improved each time until f(T) becomes zero. The final pressure at which f(T)$\equiv$ 0 is the pressure at which hydrate formation begins. In case, pressure is known, similar function is repeated to get temperature;

$$f(P) = 1 - \sum \frac{y_i}{K_i} \tag{2.11}$$

The calculations are made on water free basis assuming that there is enough

water present to form hydrate. Another use of this method is to obtain equilibrium composition of the co-existing phases in the system.

2.5.1.4 Baillie-Wichert Method

This method involves usage of a chart developed by Baillie and Wichert in 1987 [36]. The chart also uses gas gravity to account for the mixture of gases and gives the temperature of hydrate formation for given pressure. It also takes in to account the effect of sour gas (H_2S) and propane gas, which significantly effect (accelerate) the hydrate formation. The effect is incorporated by correcting the temperature according to the percentage of sour gas present. In effect, this method is an improved gas gravity method. Moreover, the method also assumes that there is sufficient water present for hydrate formation to start.

If the temperature and composition of the hydrate are known, the chart can be used to ascertain the pressure using an iterative procedure. An assumption is made about the pressure value and temperature is calculated until the actual value is obtained.

2.5.2 Modern Methods

Modern methods of obtaining the hydrate equilibrium conditions are based on statistical thermodynamic treatment to hydrates. The idea was introduced by Barrer and Stuart (1957) [7, 37] but the first successful attempt was by van der Waals and Platteeuw (1959) [7] who succeeded in linking the macroscopic properties of gases (e.g pressure and temperature) to the microscopic properties (e.g intermolecular potential). The method devised is the basis for most of the modern methods. The advantage of the method was that the microscopic properties of the (finite number of) component gases can account for infinite number of different composition (mixtures) of these gases without performing costly and time consuming experiments.

2.6 Hydrate Kinetics

While there was an extensive research earlier on (from mid 1930s to 1960s)to ascertain the equilibrium (thermodynamic conditions) of hydrate formation in order to avoid the hydrate formation in the oil and gas industry, the focus also started to shift towards the area of time dependent studies of hydrate formation and dissociation. The initial work was performed by a Russian research group led by Makogon [7, 13, 36]. The interest in the time dependent studies of hydrates grew because the sub-sea hydrate reserves offered a new promising area of energy resource. The knowledge of the time dependent properties highly facilitated in the shift of the flow assurance programs focused on the hydrate avoidance to hydrate risk management. Initially the job of the flow assurance

engineers was to ensure that the system thermodynamic properties were in the hydrate free zone all the time, but lately the assurance programs focus on delaying the hydrate formation, preventing the agglomeration of hydrate crystals etc. in order to prevent the hydrate blockages in the flow lines. As the sub-sea oil and gas exploration is moving deeper and deeper, the state of the fluid is always most certainly in the hydrate formation zone and it is highly impractical to use prevention approach for economic reasons. In this case, the knowledge of the time dependent properties of the hydrates is extremely important.

With the new and state of the art technology emerging, the techniques of studying hydrates are becoming more sophisticated and the scope of hydrate research is increasing due to new possibilities. Hydrate formation and decomposition has been studied recently with modern techniques using light scattering, calorimetry, meso-scale imaging techniques, Magnetic Resonance Micro- imaging, X-ray computed tomography etc [7, 36].

2.6.1 Time Dependent Behaviour

A system of water and a gas housed in a chamber (e.g) autoclave with constant pressure and temperature (in the hydrate prone zone) and a constant supply of gas to make up for the gas consumption by the hydrate formation shows the behaviour as depicted in figure 2.10 [7, 36]. The initial time where the small hydrate nuclei start forming but are undetectable (nano-scale) and unstable is known as induction time. The pressure and temperature conditions in the induction period are well within the hydrate zone but the system exhibits metastability and the nuclei (or cluster) form and decay at a rate that they are not detectable macroscopically. Induction time is followed by growth period where the gas consumption is increased substantially and proportionally to hydrate growth rate. The growth period is followed by the saturation period where the gas consumption gradient with time decreases and this marks the saturation of the hydrates with the gas.

If an experiment is conducted where the system of water and gas in an autoclave chamber is cooled down continuously and no gas is supplied, the behaviour of the system is as depicted in figure 2.11 [7, 36].

As the temperature of the system is dropped from temperature at ‘A’ to temperature at ‘B’, the hydrates do not start to form until point ‘B’ (system showing metastability). At ‘B’ the drastic pressure drop indicates the hydrate formation process to start until the state of the system is at point ‘C’. At point ‘C’ if the system is heated, the start of the dissociation process is marked with the increase in the pressure of the system, until all the hydrates dissociate at point ‘D’.

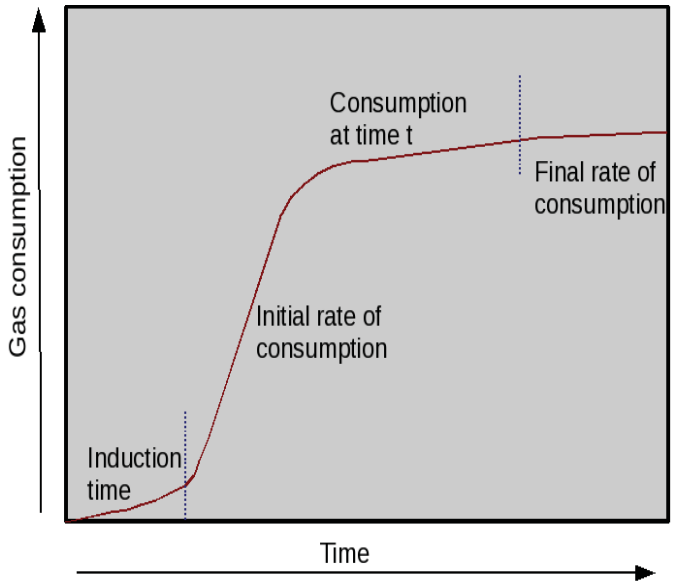

Figure 2.10: Stages of hydrate formation with time [7]

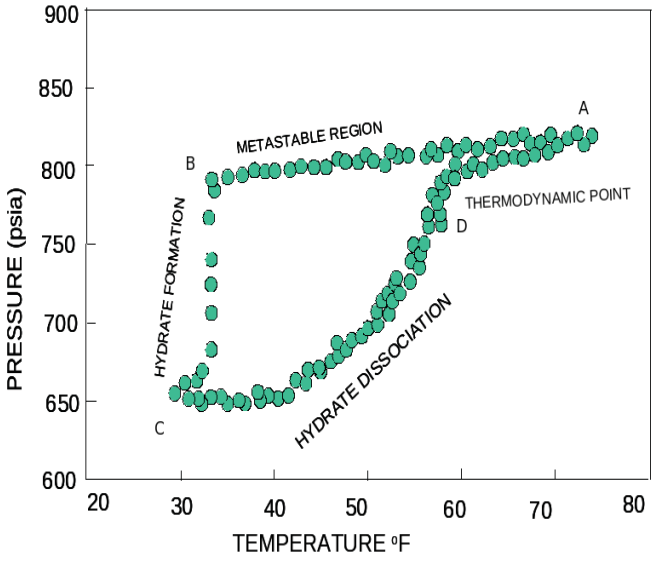

Figure 2.11: Hydrate formation and dissociation highlighting metastable behaviour [7]

Chapter 3

Phase Change and Hydrate Nucleation

3.1 Phase Change

The term 'phase' of a system relates to its state at the prevalent thermodynamic conditions. Change of phase is characterised by creation of distinct boundary in an old phase. A newly created phase has same molecules , but now the phase boundary encapsulates a volume with different density. Due to the difference in the densities between the phases there is a difference in the properties of the phases. There are various phenomena associated with the phase change which pertain to the thermodynamics and kinetics of the system. The phase change phenomenon is explained extensively in the theory of nucleation [8].

The examples of nucleation phenomenon resulting in phase change are wide spread in nature. The formation of ice from water, rain drops from vapour, bubbles in water during boiling, ice-flakes from frozen water droplets etc. Nucleation is a key concept in fields like chemistry, biophysics, metallurgy. In spite of the wide spread examples of nucleation in nature and science, the basic under-laying concept and science of nucleation is the same in each case.

3.1.1 Gibbs Energy

By definition, Gibbs energy is defined as the potential that is available for a process initiating work at constant pressure and temperature. Mathematically,

$$G = U + PV - TS \tag{3.1}$$

where G represents the Gibbs energy of a system at a particular thermodynamic state, U represents the internal energy, P stands for pressure, T stands for temperature, V stands for total volume of the system and S stands for entropy.

The sum of the first two terms on the right hand side of equation 3.1 is equal to the enthalpy of the system under consideration H. Gibbs energy is an important thermodynamic state variable, as it defines the state of the system with measurable state variables like temperature and pressure. The Gibbs energy per molecule μ is known as chemical potential of the system. Mathematically:

$$\mu = \frac{G}{M} \tag{3.2}$$

where M represents the number of molecules in the system.

Consider a reaction taking place where a system consisting of gas and water at pressure P and temperature T gets converted in to hydrate. In symbolic form, the reaction is given as [7];

$$1\,G_h + n_w H_2O \rightarrow 1[G_h.n_w H_2O] + H_f \tag{3.3}$$

Where G_h represents one molecule of gas and n_w represents the number of water molecules to form the particular form of hydrate (also known as hydration number). The right hand side of the equation shows that the 'reaction' results in formation of a single hydrate building unit and H_f represents the heat (or enthalpy) of formation for it.

In order for the reaction to go from left side of equation 3.3 to the right side, the Gibbs energy per molecule (or energy available per molecule to initiate reaction) of the reactants must be higher than the Gibbs energy per molecule of the products i.e $G_{old} - G_{new} > 0$. If ΔG is equal to zero, the forward and backward rate of reaction are equal and all the species are in chemical equilibrium. If ΔG is less than zero, then the reaction is not possible.

It is important to mention here that equation 3.3 does not represent a chemical reaction, rather it is a reaction whereby phase change occurs.

3.1.1.1 Thermodynamic Equilibrium

Thermodynamically, a system in an unstable or metastable state seeks to attain a volume at which the Gibbs energy of the system is minimum. If successful, the fluid is said to have achieved stable thermodynamic equilibrium.

Figure 3.1 is a generalised depiction of the change of the state of a fluid during phase change. The molecules of fluid in state 1 (vapour for example) have to overcome an energy barrier (depicted as $\triangle G$) in order to assume the Gibbs energy at which the volume of the system is minimum. This barrier is known as the *activation energy* of the reaction. Moving to the left side, the reaction beyond the ridge is spontaneous. For a system with M molecules a decrease in volume means an increase in the density of the system. Therefore, phase change in general is characterised by a change in the density of the system.

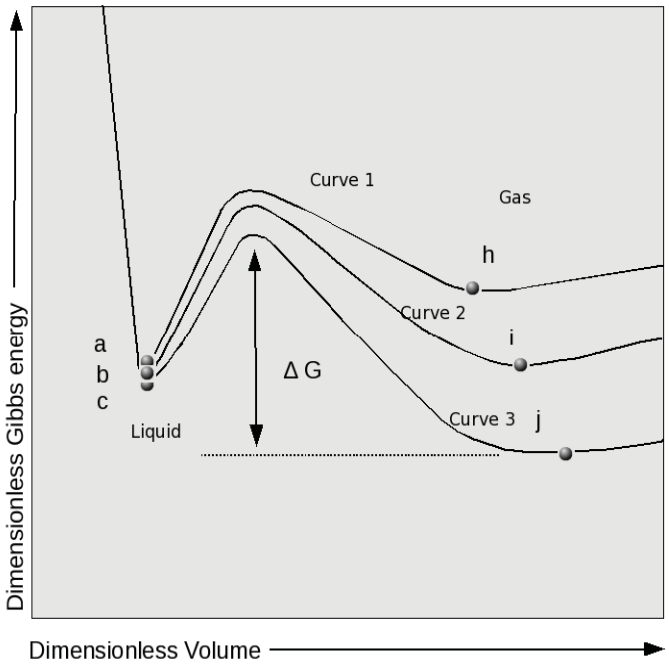

Figure 3.1: A generalised depiction of energy associated with phase transitions

If the minima of Gibbs energy of both phases of the fluid (gas and liquid for example) are equal in magnitude, the fluid is said to be in stable thermodynamic equilibrium. It can be seen in curve 2 (figure 3.1) that both the liquid state and gas (labelled b and i respectively) have equal Gibbs energies. Both phases with equal Gibbs energy can co-exist with each other and the forward and backward reactions are equal. Both of the points 'b' and 'i' lie on the binodal curve. The pressure at which the system achieves the stable thermodynamic equilibrium is called the equilibrium pressure. If the state of the fluid is such that the phases correspond to their respective minimum Gibbs energies, but the minima are not equal in magnitude, then the fluid is said to be in 'metastable thermodynamic equilibrium'. In curve 1 (figure 3.1), liquid (point a) is in stable thermodynamic equilibrium (and lies on the binodal curve) but the gas is in metastable thermodynamic region (lies in the region between spinodal and binodal curves). Similarly, in curve 3 (figure 3.1), the liquid phase corresponds to the metastable state and the gas phase is in the stable thermodynamic equilibrium. The system seeks to achieve stability and at some point and time overcomes the barrier to move towards stability. Change of phase from metastable thermodynamic equilibrium to stable thermodynamic equilibrium is known as *phase transition of first order* [8].

When the gas phase is in metastable state, the chemical potential μ_g is greater than the liquid phase chemical potential μ_l and vice versa.

Consider the case where a gas phase in metastable state is changed to liquid phase in stable thermodynamic equilibrium as depicted in figure 3.2. If the

reaction moves from right to left (from gas to liquid), the barrier that has to be overcome will be:

$$\Delta G_{initial} = (G_{ridge} - G_{gas})$$

and once the fluid crosses over the unstable state, the change in the Gibbs energy, as it attains the liquid state will be:

$$\Delta G_{final} = (G_{Liquid} - G_{ridge})$$

If the absolute value of ΔG_{final} (which is negative according to figure) is greater than the $\Delta G_{initial}$, the reaction will be energetically favourable from right to left.

On the contrary, if the fluid moves from left to right (according to figure 3.2), the activation energy encountered initially will be larger (according to figure 3.2).

Ideally the phase molecules crossing the activation barrier results in an increase in the Gibbs energy of the system and this cannot happen theoretically, but in actual phenomena, a few molecules in the system may acquire enough energy to climb the barrier, therefore it is a random process in which all the molecules of the system do not change phase spontaneously, but the phase change process starts with few phase change fluctuations.

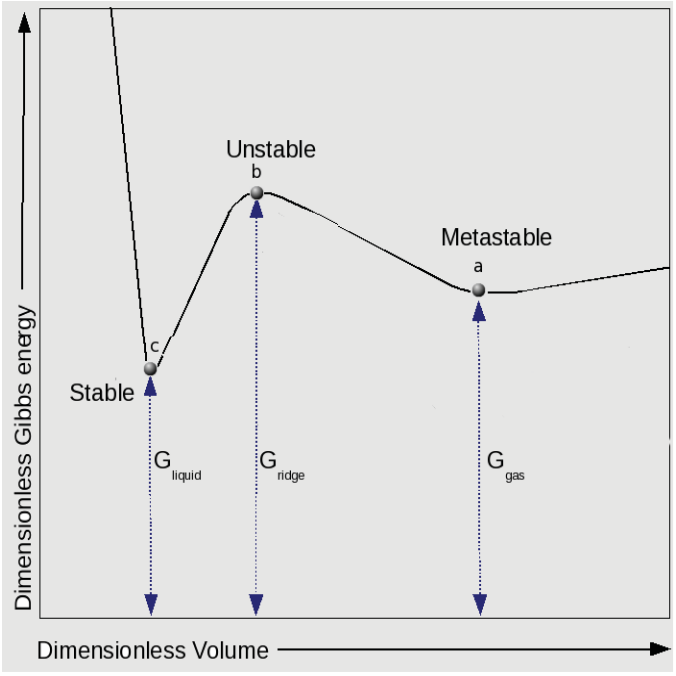

Figure 3.2: Energy diagram depicting favourable direction of reaction

3.2 Thermodynamics of Nucleation

The thermodynamic approach to nucleation considers a certain cluster of n number of molecules to be in thermodynamic equilibrium with the old phase (or substrates) but is not concerned with the temporal evolution of the cluster so that its precursors and successors are not important. In this regard, the system is considered to be *static* as far as time is involved.

3.2.1 Two Approaches to View Nucleation

The development of the nucleation theory from thermodynamical point of view has been approached in two ways in the literature. In the first approach (depicted in figure 3.3 a), the new phase is considered to have a fixed number of molecules n enclosed by an imaginary dividing surface (or boundary), so that the exact distinction can be made between the old and the new phases. In the second method (figure 3.3 b), the newly formed phase is characterized not by a distinct boundary, but rather a density fluctuation in the region in space. The schematics of both approaches are shown in the figure 3.3 [8].

In the cluster approach to nucleation, a dividing surface is assumed to encapsulate n molecules, such that the number of molecules in the cluster and outside sum equal to the total number of molecules in the system before nucleation phenomenon. Cluster approach is the most common and extensively developed approach and will be considered in the next sections.

3.2.2 Nucleation driving force

The mechanism by which the phase transition takes place is nucleation and the force which makes it possible is the difference in the chemical potential of the old and the new phases. The most general driving force expression is given as [8, 38];

$$\triangle\mu = (G_o - G_n)/M = \mu_o - \mu_n \tag{3.4}$$

where μ_o and μ_n represent chemical potential of the old and the new phase respectively and quantitatively correspond to Gibbs energy per molecule at the respective states. The expression for the driving force $\Delta\mu$ takes various forms based on the mode of the phase transition (e.g condensation, boiling, crystallisation etc.). However, the final expressions always depend on the macro state variables and physical properties of the fluid.

3.2.3 Graphical Insight to Nucleation

The cluster formed during a nucleation event may have a shape which is energetically most probable, but for the sake of brevity, consider the case of a spherical nucleus (small cluster). An expression for free energy G is given as [9]

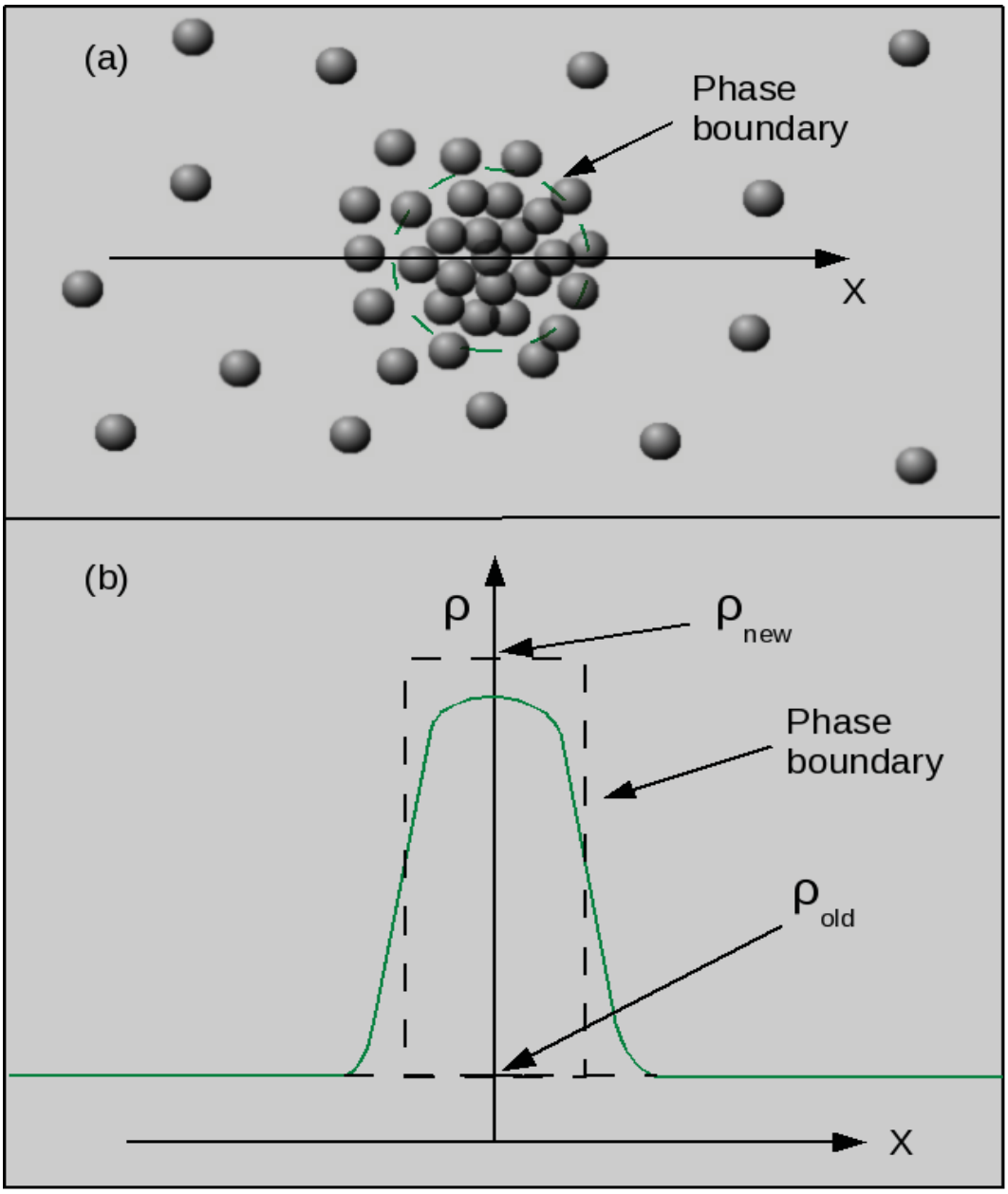

Figure 3.3: (a). Cluster approach to nucleation (b). Density functional approach to nucleation [8]

$$G = \underbrace{\frac{4}{3}\pi r^3 G_v}_{Volume\ Gibbs\ energy} + \underbrace{4\pi r^2 \sigma}_{surface\ Gibbs\ energy} \tag{3.5}$$

Here r is the radius of nucleus and σ is the interfacial tension with the evolution of the new phase. The first term in the equation represents the volume Gibbs energy and the second term represents the surface Gibbs energy [9].

$$G_{vol} = \frac{4}{3}\pi r^3 G_v \tag{3.6}$$

$$G_s = 4\pi r^2 \sigma \tag{3.7}$$

The radius of the cluster at which the slope of Gibbs potential ΔG is zero is known as the critical radius r_c. Differentiating equation 3.5 with respect to radius r and equating it to zero gives us the critical radius .

$$\frac{d}{dr}\left(\frac{4}{3}\pi r^3 G_v + 4\pi r^2 \sigma\right) = 0$$

$$\Rightarrow r_c = -\frac{2\sigma}{G_v} \tag{3.8}$$

The equation is a form of the Thomson-Gibbs equation [10] and it shows that the critical radius has a direct dependence on the surface tension i.e. the greater the surface tension, the bigger the critical radius. It has an inverse relation to the volumetric Gibbs energy G_v i.e. the greater the G_v (-ve) value, the smaller the critical size of the cluster. The nuclei with size smaller than the critical radius (with positive slope of Gibbs potential) are unstable and more likely to degenerate whereas beyond the critical radius the nuclei become stable (with negative slope of Gibbs potential).

Equation 3.5 can describe the physics of a nucleation event that is happening (considering spherical particles). The volume Gibbs energy always contributes as a negative component and the second term in equation 3.5 contributes as a positive Gibbs energy to create an interface. When the radius of the cluster is smaller than the critical radius, the surface to volume ratio is greater, so the surface tension term is scaled with higher values (than the volume Gibbs term), but as the radius increases, the surface to volume ratio starts decreasing with the effect that the volumetric (negative) component of the Gibbs energy starts dominating the surface component of the overall Gibbs energy.

Figure 3.4 depicts the situation, where to the left of the critical radius, the probability of growth for the cluster is less, and the nucleus formed may disintegrate back in to constituent particles. Towards the right, nucleation is instantaneous and crystals start growing.

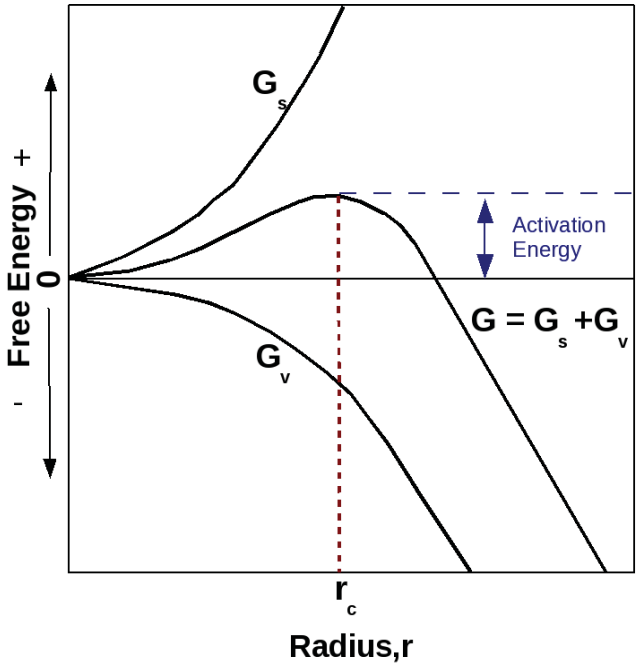

Figure 3.4: Gibbs potential variation with nucleus size [9]

3.2.3.1 Probability of Reaction

Due to the barrier, ideally the reaction should never take place, however, it is observed that the nucleation even takes places randomly over the system that is undergoing nucleation. The probability that a random event of nucleation will take place in the system is given by:

$$P_{reac} = e^{\frac{-A}{kT}}$$

where A represents the activation energy, k is the Boltzmann constant and T represents the absolute temperature.

3.3 System Description

Consider a cross-section at a certain segment of a pipe as shown in figure 3.5. The system consists of hydrocarbon gas, condensed water at the walls and a hydrate cluster. The system is assumed to be a constant pressure. Due to proximity with the gas, the liquid water also has some gas absorbed, so the liquid can be considered as gas solution. When temperature of the solution (gas-water mixture) drops, phase change results in hydrate clusters to form. The system if open with respect to mass and permeable with respect to energy.

A general relation for Gibbs energy of the system is given as:

$$G = U + PV - TS$$

Where G represents the Gibbs energy of the system at a particular state, U is the internal energy, S represents the entropy and P, V, T are pressure, volume and temperature of the system respectively. Dividing the expression by the number of moles gives the chemical potential or, Gibbs energy per mole is given as:

$$\mu = u + Pv - Ts$$

where μ is the chemical potential, or Gibbs energy per molecule of the system. v and s are specific volume and entropy of the system respectively.

Suppose that due to a small change in pressure or temperature of a system, the chemical potential of the system changes, then for an infinitesimal change in chemical potential of the system, the following equation holds:

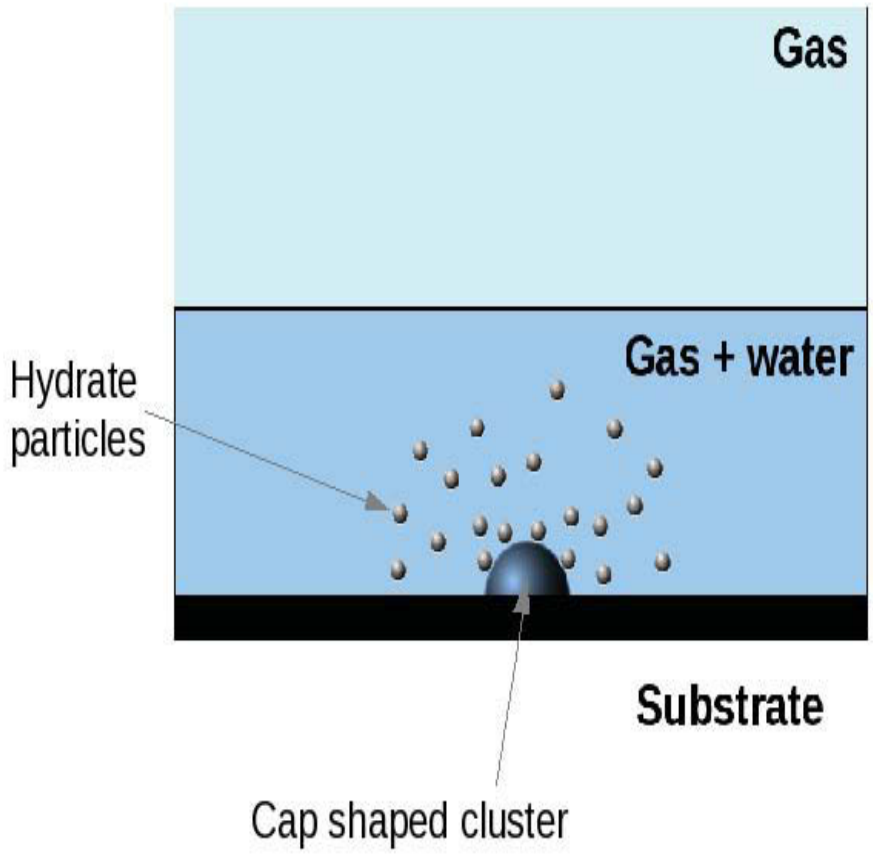

Figure 3.5: Schematic showing system of gas, water-gas solution and hydrate

$$\mathrm{d}\mu = \mathrm{d}u + \mathrm{d}(Pv) - \mathrm{d}(Ts)$$

Assuming the system to be reversible we get:

$$\mathrm{d}\mu = \mathrm{d}u + P\mathrm{d}v + v\mathrm{d}P - T\mathrm{d}s - s\mathrm{d}T$$

In case of an isobaric process:

$$\mathrm{d}\mu = \mathrm{d}u + P\mathrm{d}v + v\cancelto{0}{\mathrm{d}P} - T\mathrm{d}s - s\mathrm{d}T \tag{3.9}$$

The change in specific enthalpy of the system is given as:

$$\mathrm{d}h = \mathrm{d}u + P\mathrm{d}v + v\cancelto{0}{\mathrm{d}P} \tag{3.10}$$

and for a constant pressure process, heat added or removed from the system is given as;

$$\begin{aligned} \mathrm{d}Q &= du + \mathrm{d}W \\ &= \mathrm{d}u + \mathrm{d}(Pv) \\ &= \mathrm{d}u + P\mathrm{d}v + v\cancelto{0}{\mathrm{d}P} \end{aligned}$$

From equation 3.10 we have:

$$\mathrm{d}Q = \mathrm{d}h = T\mathrm{d}s \tag{3.11}$$

It is important to mention here that equations used above are valid for a reversible process while our system may be irreversible, but as we will be only dealing with the state functions and we are not concerned with the intermediate states or path that the system follows, so we are allowed to use the equations to achieve our objective. Using equations 3.9, 3.10 and 3.11, the equation we get is:

$$\mathrm{d}\mu = -s\mathrm{d}T \tag{3.12}$$

So the entropy of the system after infinitesimal change at constant pressure is given as:

$$s = -\frac{\mathrm{d}\mu}{\mathrm{d}T}$$

Which means that if hydrate forms from its constituents then ($\mathrm{d}\mu > 0$ and $\mathrm{d}T > 0$), there is more order in the system (negative entropy value) which obviously for a crystalline arrangement in form of a cluster results in decrease in disorder. While in the opposite case $\mathrm{d}\mu > 0$ and $\mathrm{d}T < 0$ so that there is an

increase of disorder in the system which is evident by an increase in randomly moving molecules in the bulk. Re-arranging the terms we get:

$$\mathrm{d}\mu = -s\mathrm{d}T$$

Now consider the equilibrium curve in figure 3.6, where one gas molecule and n_w water molecules under sub-cooling $(T_e - T)$ transform to a single hydrate building unit. Heat is released in the process which is known as *heat of hydrate formation*. Integrating the above equation with the limits of integration from equilibrium temperature T_e to final temperature T :

$$\int_{T_e}^{T} \mathrm{d}\mu = -\int_{T_e}^{T} s\,\mathrm{d}T$$

$$\mu(T) - \mu_e = \int_{T}^{T_e} s(T')\,\mathrm{d}T'$$

$$\mu(T) = \mu_e + \int_{T}^{T_e} s(T')\,\mathrm{d}T' \tag{3.13}$$

Consider the system experiencing a phase change from a solution (old phase) to a hydrate cluster (new phase) at constant pressure, schematically shown in figure 3.6.

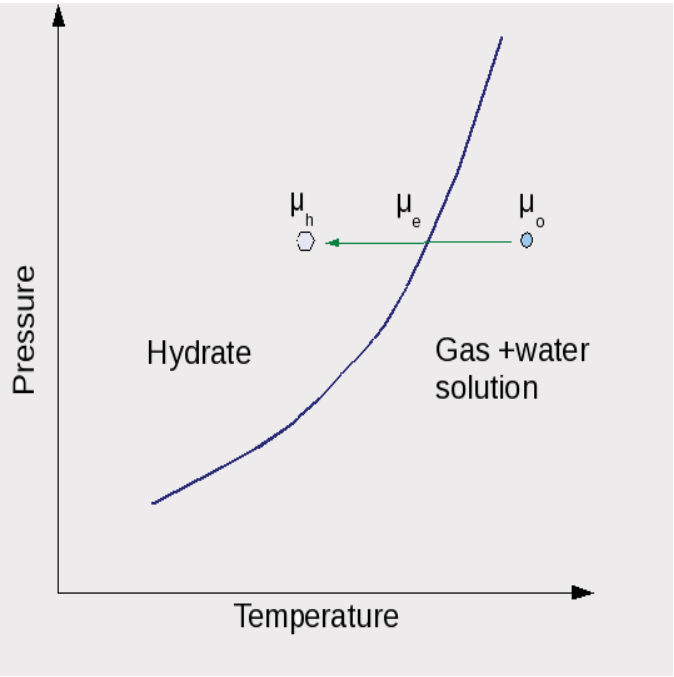

Figure 3.6: Change of phase from old (liquid) to new phase (solid)

Then the total change in Gibbs energy per molecule of the system is given as:

$$\Delta\mu(T) = \int_{T}^{T_e} \Delta s(T')\,\mathrm{d}T' \tag{3.14}$$

where $\Delta s(T') = s_{old}(T) - s_{new}(T)$. Using a Taylor series expansion about equilibrium temperature T_e we get for equation:

$$\Delta\mu(T) = -\Delta s_e(T - T_e) - (\frac{1}{2})(\frac{\mathrm{d}\Delta s}{\mathrm{d}T})_e(T - T_e)^2 - ..... \tag{3.15}$$

Truncation of the higher order terms (considering small undercoolings) results in an equation for ascertaining the change in the chemical potential for our system as:

$$\Delta\mu(T) = -\Delta s_e \Delta T \tag{3.16}$$

Equation 3.11 implies that at constant pressure we have:

$$\Delta s_e = \frac{\Delta h_e}{T_e} \tag{3.17}$$

Inserting equation 3.17 in to 3.16 we get

$$\Delta\mu(T) = -\frac{\Delta h_e}{T_e}\Delta T \tag{3.18}$$

3.4 Determination of Heat of hydrate Formation Δh_e

Consider a system consisting of hydrate nucleus (a single hydrate building unit) inside a solution of hydrocarbon gas and water. If the system if in equilibrium, the chemical potential of both the phases are equal.

$$\mu_{sol} = \mu_{hyd} \tag{3.19}$$

Now due to very small change in the pressure or temperature of the system, it rearranges itself to obtain equilibrium again so that the equation is given as:

$$\mu_{sol} + \mathrm{d}\mu_{sol} = \mu_{hyd} + \mathrm{d}\mu_{hyd} \tag{3.20}$$

The situation is depicted in figure 3.7.
The equations 3.19 and 3.20 imply that:

$$\mathrm{d}\mu_{sol} = \mathrm{d}\mu_{hyd} \tag{3.21}$$

Now remembering that:

$$\mu = u + Pv - Ts$$

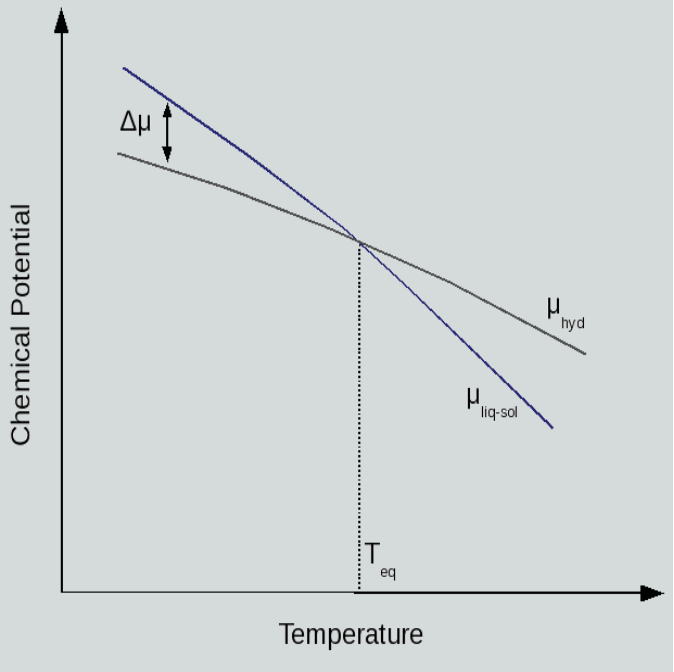

Figure 3.7: Chemical Potential due to change in pressure and temperature conditions [10]

$$\mathrm{d}\mu = \mathrm{d}u + P\mathrm{d}v + v\mathrm{d}P - s\mathrm{d}T - T\mathrm{d}s$$

which reduces to the Gibbs-Duhem form of the equation [39] :

$$\mathrm{d}\mu = v\mathrm{d}P - s\mathrm{d}T \tag{3.22}$$

inserting equation 3.22 in 3.21, we get:

$$-s_{sol}\mathrm{d}T + v_{sol}\mathrm{d}P = -s_{hyd}\mathrm{d}T + v_{hyd}\mathrm{d}P$$

rearranging the equation above gives:

$$\frac{\mathrm{d}P}{\mathrm{d}T} = \frac{\Delta s}{\Delta v} \tag{3.23}$$

where:

$$\Delta v = v_{sol} - v_{hyd}$$

Specific volume of water and hydrate are very small as compared to that of gas, so that:

$$\Delta v = v_{gas} + v_{wat} - v_{hyd} \approx v_{gas}$$

we get:

$$\frac{\mathrm{d}P}{\mathrm{d}T} = \frac{\Delta s}{v_{gas}} \tag{3.24}$$

which gives the slope of the phase equilibrium curve (between solution and hydrate)

Now considering the equation of state $v_{gas} = zRT/P$ and taking to account equation 3.23 and 3.17, we can write:

$$\frac{\mathrm{d}P}{\mathrm{d}T} = \frac{\Delta h_e P}{zRT^2}$$

re-arranging the terms we get:

$$-\frac{\mathrm{d}P/P}{T^{-2}\mathrm{d}T} = -\frac{\Delta h_e}{zR}$$

Finally we get the Clausius-Clapeyron equation in order to estimate the heat of hydrate formation:

$$\frac{\mathrm{d}ln\, P}{\mathrm{d}(1/T)} = -\frac{\Delta h_e}{zR} \tag{3.25}$$

With this equation we can estimate the heat of hydrate formation if the pressure temperature conditions and gas compressibility factor are known. The gas compressibility factor as a function to temperature (at constant pressure) was determined by deriving a relationship from curve fit with data obtained by using Redlich -Kwong method [40], and solving a third degree equation of compressibility factor iteratively. The chart of compressibility factor (of gas mixture) as a function of temperature at constant pressure is given in Appendix A.

3.5 Work of Cluster Formation

Consider a more detailed schematic of the phenomenon that occurs inside our stated system for cluster formation. In case of the system under consideration, as the water- gas solution is just touching the pipe wall, the surface of the wall will act as substrate. Literature [8] shows that the most probable mode of nucleation in this situation is the cap shaped nucleation. This is due to the fact that the pipe wall acting as substrate assists the nucleation process so that this mode of nucleation is most energetically favourable.

The surface energy of the cap shaped cluster is given as [8]:

$$\Phi = \sigma A_{sh} + \sigma_i A_b - \sigma_s A_b \tag{3.26}$$

where σ is the interfacial tension of the cluster/bulk phase, σ_i is the surface energy of the droplet at the interface and σ_s is the substrate surface energy . The relation ship between the interfacial tensions of a cap shaped cluster on a substrate is given by Young's equation [8]:

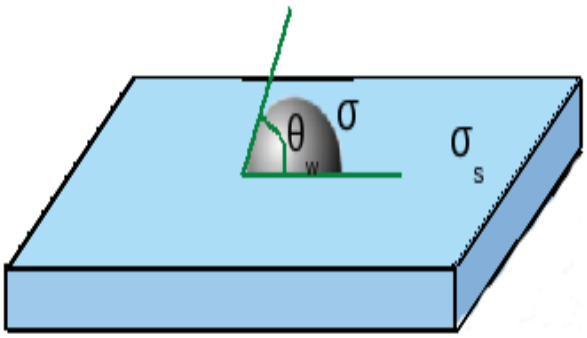

Figure 3.8: Schematic showing the mode of cluster formation

$$\sigma_s = \sigma_i + \sigma cos\theta \tag{3.27}$$

The interfacial area between cluster and substrate, and the surface area of the cluster exposed to the bulk phase is given as [8]:

$$A_{sh} = \pi r^2 sin^2\theta \tag{3.28}$$

$$A_b = 2\pi r^2(1 - cos\theta) \tag{3.29}$$

Inserting the expressions of area in to equation 3.21, we get:

$$\Phi = 2\pi r^2(1 - cos\theta)\sigma + \pi r^2 sin^2\theta(\sigma_i - \sigma_s) \tag{3.30}$$

Assuming the spherical cap shape to be the equilibrium shape, the volume of the cluster is given as [10]:

$$V_c = \frac{4}{3}\pi r^3 \frac{(1 - cos\theta)^2(2 + cos\theta)}{4} \tag{3.31}$$

where the factor:

$$\psi = \frac{(1 - cos\theta)^2(2 + cos\theta)}{4}$$

is the shape factor based on the contact angle θ which the cluster makes with the wall.

The change in the Gibbs energy of the system (which is actually the work of cluster formation) upon formation of cluster on the surface of the substrate is given as:

$$\Delta G = G_2 - G_1 \tag{3.32}$$

where G_1 represents the Gibbs energy of the system before nucleation and G_2 represents the Gibbs energy of the system after the nucleation event took place.

Suppose the system has M molecules of the bulk phase before the cluster is formed, then [8]:

$$G_1 = M\mu_{sol} \tag{3.33}$$

At a certain time, due to fluctuations in the system , a few molecules n combine to form a cluster so that Gibbs energy of the system after the nucleation event is [8]:

$$G_2 = (M-n)\mu_{sol} + n\mu_{hyd} + \Phi \tag{3.34}$$

Where n is the number of molecules in the cluster, $M-n$ is the number of molecules of the bulk phase that remain after the cluster formation and Φ represents the total surface energy of the cluster.

Inserting equations 3.33 and 3.34 in 3.32, we get,

$$\Delta G = -n\Delta\mu + 2\pi r^2(1-cos\theta)\sigma + \pi r^2 sin^2\theta(\sigma_i - \sigma_s) \tag{3.35}$$

where n is the number of molecules in the cluster which can be written in the form $n = V_c/v_c$, where V_c is the volume of the cluster and v_c is the volume of a single building block of the cluster of n building blocks. Inserting in the above equation the value of n and $\sigma_s - \sigma_i = \sigma cos\theta$, we get an expression of the form:

$$\Delta G = \frac{4}{3}\pi r^3 \frac{(1-cos\theta)^2(2+cos\theta)}{4}\frac{\Delta\mu}{v_c} + 2\pi r^2(1-cos\theta)\sigma -, \\ \pi r^2 sin^2\theta\sigma cos\theta \tag{3.36}$$

Finding the critical radius by differentiating the above equation with respect to r and equating it to zero, we get:

$$r^* = \frac{2\sigma v_c}{\Delta\mu} \tag{3.37}$$

Which is again a form of the Thomson-Gibbs equation.

Inserting the critical radius expression in equation 3.35 we get the maximum work of cluster formation (activation energy) in case of cap shaped cluster on substrate [8, 10]:

$$\Delta G^*_{het} = \psi(\theta)\frac{16\pi\sigma^3 v_c^2}{3\Delta\mu^2} \tag{3.38}$$

3.6 Nucleation rate

Assuming that initially there is a concentration fixed for nuclei with different sizes up to critical size n^* present in the system. The equilibrium shape of the nuclei is assumed to be spherical and it is further assumed that the reactions taking place for change in the concentration of nuclei are aggregation type reactions in which only a monomer (single hydrate building unit) attaches or detaches to the cluster belonging to a size group to form a new nuclei. The methodology adopted follows the basic nucleation approach given in theory [8, 10].

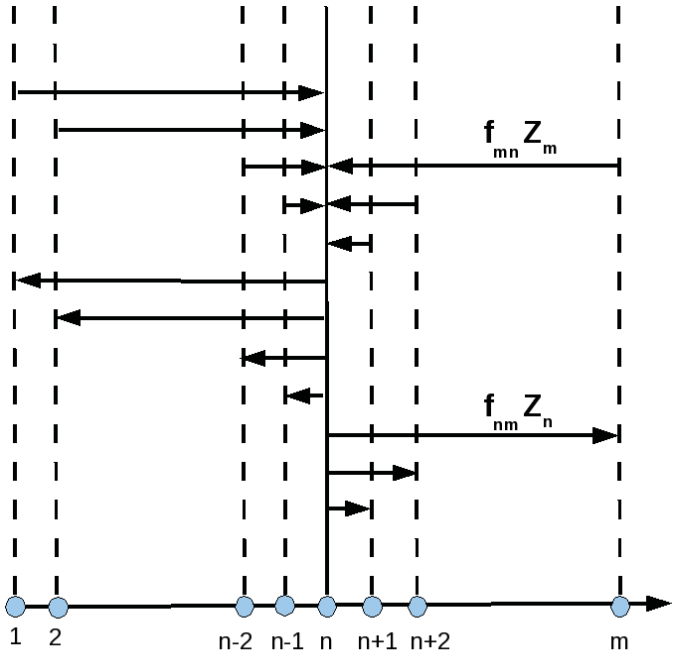

Figure 3.9: Schematic showing attachment and detachment balance [8]

The attachment or detachment mechanism is described in form of equations below:

$$
\begin{aligned}
A_1 + A_1 &\underset{w_{2-}}{\overset{w_{1+}}{\rightleftharpoons}} A_2 \\
A_2 + A_1 &\underset{w_{3-}}{\overset{w_{2+}}{\rightleftharpoons}} A_3 \\
&\vdots \\
A_n + A_1 &\underset{w_{n+1-}}{\overset{w_{n+}}{\rightleftharpoons}} A_{n+1}
\end{aligned}
$$

Where A_1 which represents a monomer (a single hydrate building unit) attaches to or detaches from a cluster of another size group (class) to form

a cluster with size different from both. The assumption of aggregation by monomers is reasonable when the concentration of multimers is still low and the probability of a monomer- multimer attachment/ detachment is higher than multimer-multimer interactions. In the reactions above w_{1+}, w_{2+}... represent the attachment attempt frequency and w_{1-}, w_{2-}... represent detachment frequency of monomers.

Writing a balance equation for clusters containing n number of building units (molecules etc.) according to the assumptions above, we get:

$$\frac{\mathrm{d}Z_n(t)}{\mathrm{d}t} = w^+_{(n-1)}Z_{n-1}(t) - w^-_{(n)}Z_n(t) - w^+_{(n)}Z_n(t) + w^-_{(n+1)}Z_{n+1}(t) \tag{3.39}$$

where the term on the left hand side represents the rate of change of concentration $Z_n(t)$ of clusters of class n. If we denote the flux through size n as:

$$J_n(t) = w^+_{(n-1)}Z_{n-1}(t) - w^-_{(n)}Z_n(t) \tag{3.40}$$

Where $w^+_{(n-1)}$ represents the attachment frequency of monomer to $n-1$ class of cluster. $Z_{n-1}(t)$ is the concentration of the $n-1$ size cluster at time t. Inserting in equation 3.39 we get:

$$\frac{\mathrm{d}Z_n(t)}{\mathrm{d}t} = J_n(t) - J_{n+1}(t) \tag{3.41}$$

Under steady state conditions $\frac{\mathrm{d}Z_n(t)}{\mathrm{d}t} = 0$ and equation 3.41 is reduced to:

$$J_n(t) = J_{n+1}(t) = J_o \tag{3.42}$$

where J_o is the steady state rate of formation of cluster of any class (size). Using equation 3.40 we can write, for steady state nucleation rate:

$$\begin{aligned}
J_o &= w^+_1 Z_1 - w^-_2 Z_2 \\
J_o &= w^+_2 Z_2 - w^-_3 Z_3 \\
&\vdots \\
J_o &= w^+_n Z_n - w^-_{n+1} Z_{n+1} \\
&\vdots \\
J_o &= w^+_{N-1} Z_{N-1}
\end{aligned}$$

Where $Z_1, Z_2, ...$ represent steady state concentrations of different cluster. Multiplying first equation by $1/w^+_1$, second by $w^-_2/w^+_1 w^+_2$ and so on, and after certain operations we get:

$$J_o = Z_1 \left[\sum_{n=1}^{N-1} \left(\frac{1 w^-_2 w^-_3 \dots w^-_n}{w^+_n w^+_1 w^+_2 \dots w^+_{n-1}} \right) \right]^{-1} \tag{3.43}$$

Considering equilibrium state in a supersaturated state (approximating metastable equilibrium with $\mu_{old} \approx \mu_{new}$), we can consider $J_o = 0$ so that we get:

$$w_{n-1}^{+} N_{n-1} = w_n^{-} N_n \tag{3.44}$$

where N_n represent equilibrium concentrations of the clusters of class n in the absence of flux (of hydrate building units). The equation can be re-arranged as:

$$\frac{N_n}{N_{n-1}} = \frac{w_{n-1}^{+}}{w_n^{-}} \tag{3.45}$$

multiplying the ratios N_n/N_{n-1} from $n = 2$ to n gives us:

$$\frac{N_n}{N_1} = \prod_{1=2}^{n} \left(\frac{w_{i-1}^{+}}{w_i^{-}} \right) = \left(\frac{w_2^{-} w_3^{-} \dots w_n^{-}}{w_1^{+} w_2^{+} \dots w_{n-1}^{+}} \right)^{-1} \tag{3.46}$$

3.6.1 Attachment Frequency

For 3-D nucleation of clusters in form of caps where diffusion of hydrate building units to the cluster is the mechanism by which the hydrate building units attach to the cluster , the frequency factor for attachment is given in form:

$$w_{n-1}^{+} = \epsilon J_{d,n}(t) 4\pi r^2 \tag{3.47}$$

where $\epsilon \leq 1$ is the sticking coefficient of the particles (hydrate building units) to the cluster as all the building units diffusing to the surface of cluster do not succeed in attaching to the surface. A value of $\epsilon = 1$ means all the incoming particles sticking to the surface and $\epsilon = 0$ means no particles sticking at all. $J_{d,n}(t)$ is the incoming diffusion flux of the particles and r is the radius of curvature of the cap-shaped cluster. The diffusion flux is calculated from the Fick's law with appropriate initial boundary conditions for cap shaped cluster.

$$Jd, n = DZ_1(t)/R \tag{3.48}$$

Where D is the diffusion coefficient of the hydrate building units to the cluster which can be regarded as diffusion coefficient of the gas in water. Inserting the above equation in equation 3.47, we get,

$$w_{n-1}^{+} = \epsilon_{n-1} 4\pi r Z_1(t) \tag{3.49}$$

In a quasi-static system, $Z_1(t)$ can be replaced by equilibrium concentration of monomers (single hydrate building units) N_1 . The equilibrium concentration N_1 is actually the concentration of gas molecules in the system as according to equation 3.3, number of moles of gas and hydrate building unit are equal. Replacing the radius with the expression $r = (c/4\pi)^{1/2} v_{hyd}^{1/3} n^{1/3}$ where

$c = (36\pi)^{1/3}$ is the shape factor for spherical nuclei, we get the frequency factor for attachment as:

$$w_{n-1}^{+} = \epsilon(4\pi c)^{1/2} v_{hyd}^{1/3} D N_1 n^{1/3} \tag{3.50}$$

In the equation w_{n-1}^{+} is the attachment attempt frequency of a single hydrate building unit to a cluster of size n. The factor takes in to account the physics of gas diffusion in water, equilibrium concentration of hydrate building units, probability of attachment upon contact etc.

3.6.2 Detachment Frequency

The detachment process of a hydrate building unit from the cluster of class n is dictated by the chemical potential difference between the cluster μ_n and bulk phase μ_e. The relationship is given by the Thomson-Gibbs equation:

$$\mu_{sol} - \mu_{hyd} = \frac{2\sigma v_{hyd}}{r} \tag{3.51}$$

which is actually the work gained when a hydrate building unit is attached to the hydrate cluster. The probability that a hydrate building unit breaks free from the cluster of size n to form the $n-1$ size cluster, overcoming the surface tension, is given by:

$$prob = exp\left(\frac{-\Delta\mu}{kT}\right)$$

We can get the detachment frequency w_n^{-} by the probability of detachment given in equation above.

so inserting the expression 3.45, we get

$$N_n = N_{n-1} exp\left(-\frac{\Delta G(1))}{kT}\right) \tag{3.52}$$

Rearranging the equations leads to:

$$\frac{N_n}{N_{n-1}} = exp\left(-\frac{\Delta G(1))}{kT}\right) \tag{3.53}$$

Using equation 3.53 for all n in expression 3.46, we get:

$$N_n = N_1 exp\left(-\frac{\Delta G(n)}{kT}\right) \tag{3.54}$$

Which gives the equilibrium concentration of any size class n based on Gibbs energy.

In case of critical sized clusters, the equilibrium concentration is given as:

$$N^* = N_1 exp\left(-\frac{\Delta G^*}{kT}\right) \tag{3.55}$$

3.6.3 Steady State Nucleation rate

Expression for steady state nucleation rate can be written as [10]:

$$J_o = w^* \Gamma N^* \tag{3.56}$$

where w^* is the frequency of attachment to critical sized cluster, N^* is the concentration of critical sized cluster at equilibrium and Γ is the Zeldovich factor which describes how far the system is from equilibrium, and it is given as [8, 10]:

$$\Gamma = \left(\frac{\Delta G^*}{3\pi k T n^{*2}} \right)^{1/2} \tag{3.57}$$

The Zeldovich factor scales N^* which is the equilibrium concentration of critical nuclei, when the system is not in equilibrium.

So using equation 3.50 with $n = n^*$ i.e for critical cluster size and equation 3.57 in equation 3.56, we get for the steady nucleation rate:

$$J_o = \Gamma \epsilon (4\pi c)^{1/2} v_{hyd}^{1/3} D N_1 n^{*1/3} N_1 exp\left(-\frac{\Delta G^*}{kT} \right) \tag{3.58}$$

Now for the equilibrium concentration of monomer (N_1) nuclei we have an expression [8, 10]:

$$N_1 = N_o \mathbf{exp}\left(\frac{-\Delta \mu}{kT} \right) \tag{3.59}$$

where N_o is the concentration of sites (on substrate) initially in heterogeneous system where nuclei can start nucleating. Inserting equation 3.59 in 3.58, we get:

$$J_o = \Gamma \epsilon (4\pi c)^{1/2} v_o^{1/3} D N_1 n^{*1/3} N_o exp\left(-\frac{\Delta \mu + \Delta G^*}{kT} \right) \tag{3.60}$$

In case of heterogeneous nucleation at a pipe wall or at a liquid gas interface when other microscopic impurities are not present, $N_0 \approx 1/a_w \approx 8 \times 10^{18} m^{-2}$ [8], where a_w is the area that a single water molecule occupies on a substrate.

The terms inside the exponential represent the probabilities of molecules from bulk fluid overcoming the activation barrier to form an n sized cluster and a single hydrate building unit overcoming the activation energy of the surface formation.

All the physics capturing the diffusion phenomenon, attachment and detachment attempt frequencies, probability of successful attachment, dimensions of particles/ substrate, surface energy effects and probabilities of overcoming the activation barriers of surface attachment and volume formation are embedded in the equation.

3.7 Growth of Nuclei

So far we assumed that an initial concentration of nucleation sites was present for nucleation process. In order to incorporate the growth rate of nuclei, consider a initial volume of gas-water solution V_s which is under supersaturation condition. At time t', a nucleus is born and it strives to attain a critical size. This nucleus may disintegrate or it will surmount the critical activation barrier. In a similar manner different nuclei are born at different instances and start growing at a constant growth rate. The situation is depicted graphically in figure 3.10. The derivations are used from the work in induction time and growth theory in literature [41].

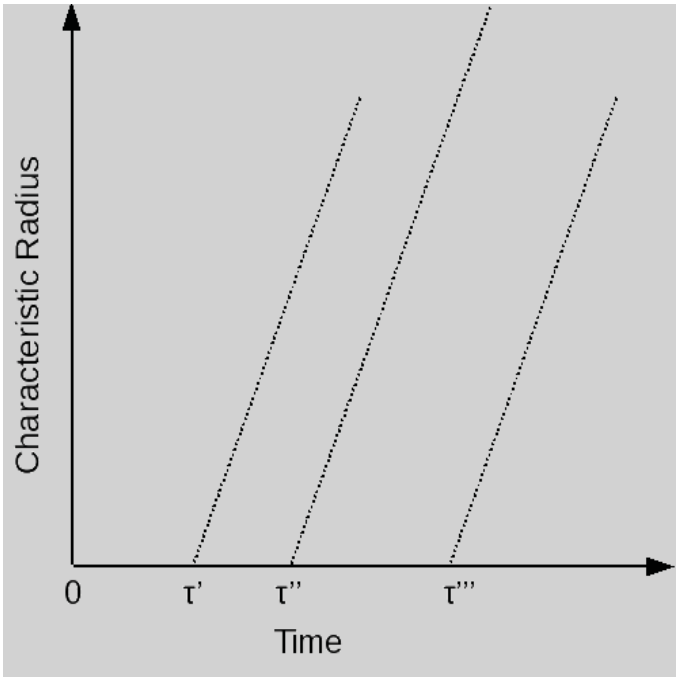

Figure 3.10: Schematic showing the incipience of nuclei and growth

The figure is showing a linear growth rate, with the same slope for all the nuclei. However the growth rate can follow some other trend e.g parabolic. Then the growth rate of increase in the volume fraction $\alpha(t)$ of the hydrate crystals is given as:

$$\alpha(t) = \frac{V(t)}{V_s} \tag{3.61}$$

where $V(t)$ is the total volume of all the hydrate crystals at time t. Assuming that the growth of the crystallites is isomorphic and that they do not touch each other during the course of growth (very dilute at initial stages), the change in the volume of a crystal between time t' and $t' + \mathrm{d}t'$ is given as:

$$\mathrm{d}V = Vc(t', t)J(t')A_s\mathrm{d}t' \tag{3.62}$$

where $Vc(t', t)$ is the volume of crystal which grows following some growth rate expression , $J(t')$ is the nucleation rate at the instant t' , A_s is the area of the substrate. The product $J(t')A_s\mathrm{d}t'$ gives the nuclei born between time t' and $t' + \mathrm{d}t'$. integrating the equation 3.62 from initial time $t_i = 0$ to some later time t , we have:

$$V(t) = A_s \int_0^t j(t')Vc(t', t)dt' \tag{3.63}$$

Putting equation 3.63 in equation 3.61, we get:

$$\alpha(t) = \frac{A_s}{V_s} \int_0^t j(t')Vc(t', t)dt' \tag{3.64}$$

A crystal volume born at time t' and assumed to retain the same shape during growth can be characterised using a radius:

$$\begin{aligned} Vc(t', t) = br^3(t', t) &= b\left[\int_0^t g(t'')\mathrm{d}t'' - \int_0^{t'} g(t'')\mathrm{d}t''\right]^3 \\ &= b\left[\int_0^{t-t'} g(t'')\mathrm{d}t''\right]^3 \end{aligned} \tag{3.65}$$

where b is a shape factor e.g $4/3\pi$ for spheres, $g(t) = \frac{\mathrm{dr}}{\mathrm{d}t}$ is the crystalline growth rate. Inserting equation 3.65 in equation 3.64 we get:

$$\alpha(t) = \frac{bA_s}{V_s} \int_0^t j(t') \left[\int_0^{t-t'} g(t'')\mathrm{d}t''\right]^3 dt' \tag{3.66}$$

Expressing radius $r(t)$ as a function of time as:

$$r(t) = (Gt)^m \tag{3.67}$$

which implies that:

$$g(t) = mG^m t^{m-1} \tag{3.68}$$

where G is the growth constant and m is a number. Both are defined for specific cases of nucleation event. For example for growth by diffusion of gas molecules towards a cluster [41]:

$$G(m^2/s) = 2\epsilon v_h DC_e \left[\exp\left(\frac{\Delta\mu}{kT}\right) - 1\right], m = 1/2 \tag{3.69}$$

Assuming the nucleation rate to be stationary (not dependent on time) given by equation 3.60, and using in equation 3.66 while integrating it, we get:

$$\alpha(t) = \left(\frac{bA_s}{V_s}\right) J_o \left[\int_0^{t-t'} mG^m t^{m-1} \mathrm{d}t\right]^3 \tag{3.70}$$

using $m = 1/2$ (as in eq. 3.69) we get:

$$\alpha(t) = \left(\frac{bA_s}{V_s}\right) J_o G^{3/2} \left(t - t'\right)^{3/2} \tag{3.71}$$

where $(t - t')$ is the time elapsed since the birth of nuclei.
As the overall rate of reaction for equation 3.3 is given as:

$$R(t) = \mathrm{d}N(t)/\mathrm{d}t \tag{3.72}$$

Realizing that $\alpha(t) = \frac{V(t)}{V_s} = \frac{N(t)}{N_s}$:

$$R(t) = N_s \mathrm{d}\alpha(t)/\mathrm{d}t \tag{3.73}$$

inserting 3.71 in 3.73 we get:

$$R(t) = \frac{3}{2} \frac{bN_s A_s J_o G^{3/2} (t - t')^{1/2}}{V_s} \tag{3.74}$$

Which is the reaction rate (No.of moles/m^2/s) for cap shaped nuclei formed within the heterogeneous nucleation phenomenon. It takes in to account the nucleation rate and growth of nucleated cluster simultaneously. The number of moles can be converted to mass of hydrate formed which gives the mass of gas and water consumed.

Chapter 4

Mathematical Framework

In order to ascertain the flow field in the fluid dynamics and heat transfer problems, equations which describe the transport of conserved quantities such as mass, momentum, energy are required. These equations are mathematical expressions for the change of these conserved quantities in the computational domain and with time. Due to generality of the topics, the material presented in the chapter has largely been taken from the Fluent Users manual [42] and Comet Users manual [12] and describes the mathematical expressions required for complete description of the system.

4.1 Mixture Model Conservation Equations

The flows which are characterized by two or more phases intermixed such that phases can move at different velocities, but assume local equilibrium over spatial lengths can be modeled using the mixture model framework. Mixture flows can be observed widely in nature. The general classification of mixture model flows involve particle laden flows, gas mixture flows, slurry flows etc.

The mixture model of the commercial CFD code 'Fluent' [42] allows to model the flow a mixture of 'n' different phases through the flow domain [42]. The flow of fluid mixture if described by a set of continuity (for mixture and for each phase), momentum and energy conservation equations. To account for the effects of turbulence, the standard k-ϵ model [42] is included. The conservation equations describing a mixture of 'n' different phases are given below:

4.1.1 Continuity

The continuity equation is based on mass conservation law i.e mass can not be created nor destroyed. Mathematically:

$$\frac{\partial}{\partial t}\left(\rho_m\right) + \nabla \cdot \left(\rho_m \mathbf{u}_m\right) = 0 \tag{4.1}$$

where $\mathbf{u}_m$ is the mass averaged velocity of a number n phases in the mixture given as:

$$\mathbf{u}_m = \frac{\sum_{k=1}^{n} \alpha_k \rho_k \mathbf{u}_k}{\rho_m} \tag{4.2}$$

and ρ_m is the mixture density (of n phases) given as:

$$\rho_m = \sum_{k=1}^{n} \alpha_k \rho_k \tag{4.3}$$

where α_k represents the phase volume fraction of the 'kth' phase, so that:

$$\sum_{k=1}^{n} \alpha_k = 1$$

The first term in equation 4.1 is the transient (rate of change) term while the second term represents the net mass flux in each coordinate direction.

4.1.2 Momentum

The conservation of linear momentum equation for a mixture of 'n' phases is based on the Newtons second law of motion which states that the rate of change of linear momentum (of a body) is equal to the sum (resultant) of all the forces acting upon it. Considering a fluid element with n number of intermixed phases, the mathematical form of conservation of momentum can be written as:

$$\begin{aligned} \frac{\partial}{\partial t}\left(\rho_m \mathbf{u}_m\right) + \nabla \cdot \left(\rho_m \mathbf{u}_m \mathbf{u}_m\right) &= -\nabla p + \nabla \cdot \left[\mu_m \left(\nabla \mathbf{u}_m + \nabla \mathbf{u}_m^T\right)\right] + \rho_m \mathbf{g}, \\ &\quad + \mathbf{F} + \nabla \cdot \left(\sum_{k=1}^{n} \alpha_k \rho_k \mathbf{u}_{dr,k} \mathbf{u}_{dr,k}\right) \end{aligned} \tag{4.4}$$

μ_m is the viscosity of the mixture, mathematically:

$$\mu_m = \sum_{k=1}^{n} \alpha_k \mu_k$$

$\vec{u}_{dr,k}$ represents the drift velocity of the kth phase with respect to the mass averaged velocity mathematically as:

$$\mathbf{u}_{dr,k} = \mathbf{u}_k - \mathbf{u}_m$$

In equation 4.4, the first term on the left hand side represents that rate of change of momentum of the mixture with time and the second term describes the rate of change in momentum due to net convection. The right hand side

represents the forces acting on the fluid element. The first term on the right side represents the forces due pressure gradient, second term represents viscous forces, third term gives the forces due to gravity, fourth term represents all the other body forces and the last term represents force due to drift of phases.

4.1.2.1 Source term in Momentum equation

In the source term in the momentum equation, forces due to gravity are given by [42, 43]:

$$\mathbf{f_B} = \rho_\mathbf{m}\mathbf{g} \tag{4.5}$$

where ρ represents the density and $\mathbf{g}$ represents the acceleration due to gravity.

4.1.3 Energy

The energy equation for the mixture of n phases is based on the first law of thermodynamics which states that energy can be neither created nor destroyed but only converted to other useful forms. The energy conservation equation for the mixture is given as:

$$\frac{\partial}{\partial t}\sum_{k=1}^{n}(\alpha_k\rho_k h_k) + \nabla\cdot\sum_{k=1}^{n}(\alpha_k\mathbf{u}_k\rho_k h_k) = \nabla\cdot[k_{eff}\nabla T] + S_h \tag{4.6}$$

where k_{eff} is the effective thermal conductivity.

In equation above the first term on the left hand side represents the temporal change in energy, the second term (under summation sign) represent changes in energy due to convection. Right hand side of the equation represent changes in energy due to diffusion processes and source terms S_h (heat sources, reactions etc.)

4.1.4 Volume Fraction equation for secondary phases

The continuity equation for each phase is defined in the mixture model. The equation is mathematically given as:

$$\frac{\partial}{\partial t}(\alpha_p\rho_p) + \nabla\cdot(\alpha_p\rho_p\mathbf{u}_m) = \sum_{q=1}^{n}(\dot{m}_{qp} - \dot{m}_{pq}) \tag{4.7}$$

The first term on the left hand side gives the temporal change of secondary phase q in the control volume. The second term is the convective term based on the mass averaged mixture velocity. The right hand side gives the source and sink terms for the secondary phase. In the equations, α represents the phase volume fraction and subscripts p and q represent secondary and primary phases respectively.

4.1.4.1 Sources due to phase change

While modeling a multicomponent mixture in which phase change as a result of a certain reaction is considered, the enthalpy of formation of the product (or the final phase) has to be accounted for in the energy equation. The source term contribution is given as [43]:

$$S_h = -\sum_{k=1}^{n} \alpha_k h_k R_k \tag{4.8}$$

where α_k represents the phase fraction of phase k, h_k represents the enthalpy of formation of the kth phase. R_k is equal to sum of the reaction sources over all the reactions n_R taking place in the solution domain. Mathematically:

$$R_{k,m} = \sum_{k=1}^{n_R} c_k R_{k,m} \tag{4.9}$$

where $R_{k,m}$ is the rate of creation/ destruction of phase k in reaction m and c_k is the mass fraction of any phase 'k' given as:

$$c_k = \frac{\alpha_k \rho_k}{\rho_m} \tag{4.10}$$

4.1.5 Relative and Drift Velocity

As the mixture consists of one primary phase and one or more secondary phases, there can be a considerable difference in the velocity of phases due to density differences and effect of forces. In order to incorporate the effect of slip between phases, the concept of relative velocity is used. Relative or slip velocity between a primary phase q and a secondary phase p is defined as:

$$\mathbf{u}_{pq} = \mathbf{u}_p - \mathbf{u}_q \tag{4.11}$$

The drift velocity of a secondary phase used in the mixture momentum equation is described in terms of relative velocity as;

$$\mathbf{u}_{dr,p} = \mathbf{u}_{pq} - \sum_{k=1}^{n} c_k u_{qk} \tag{4.12}$$

Fluent's mixture model makes use of the algebraic slip model. A relationship by Manninen et. al [42] is given as;

$$\mathbf{u}_{pq} = \frac{\tau_p}{f_{drag}} \frac{(\rho_p - \rho_m)}{\rho_p} a \tag{4.13}$$

In the equation above τ_p is defined as the particle relaxation time, which gives the average time scale of the particle of a secondary phase p without interaction. Mathematically, Particle relaxation time is defined as:

$$\tau_p = \frac{\rho_p d_p^2}{18\mu_q} \tag{4.14}$$

where d_p is the diameter of the particle of the second phase p, a is the acceleration of the secondary phase particle given as;

$$a = \mathbf{g} - (\mathbf{u}_m \cdot \nabla)\mathbf{u}_m - \frac{\partial \mathbf{u}_m}{\partial t} \tag{4.15}$$

f_{drag} is the drag function. The Schiller and Neumann definition [42] of the drag function is given as;

$$f_{drag} = \begin{cases} 1 + 0.15Re^{0.687} & \text{if } Re \leq 1000 \\ 0.0183 & \text{if } Re \geq 1000 \end{cases}$$

4.2 Turbulence Modelling

In most cases, fluid flows are not streamlined and are characterized by random fluctuations, irregular patterns and eddies in the flow stream. These fluctuations cause significant contribution to mass, momentum and energy transfer terms (mixing and energy dissipation), making them different from the regular stream lined (laminar) flows. In order to model the effect of these irregular contributions on the mean flow, turbulence modelling is necessary. To start the modelling process, the flow variables in a turbulent flow are assumed to be composed of mean and fluctuating components. The instantaneous value can be treated as fluctuating part superimposed on a mean part [11]. Mathematically:

$$\phi(t) = \Phi + \phi'(t) \tag{4.16}$$

Where $\phi(t)$ represents the instantaneous value, Φ the mean value and $\phi'(t)$ the fluctuating part of the flow variable. The situation is graphically described in figure 4.1 [11].

For most engineering purposes, it is not necessary to resolve the turbulent eddies, but only the mean flow behaviour. However, inserting the instantaneous values as described in equation 4.16 in Navier-Stokes (NS) equations and using an averaging procedure for the NS equations gives us the Reynold-Averaged Navier-Stokes (RANS) equations, which contain terms containing mean quantities, and certain extra terms which are products of fluctuating variables. These extra terms (product of fluctuating variables) have to be accounted for using some models as they have a significant effect on the mean flow properties. These terms are of the general form:

$$\rho\overline{u'\phi'}$$
$$\rho\overline{v'\phi'}$$
$$\rho\overline{w'\phi'}$$

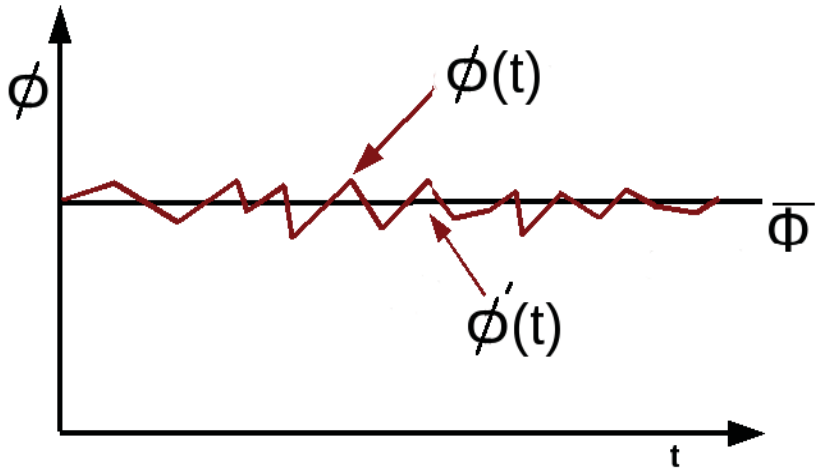

Figure 4.1: Instantaneous variation of ϕ in a turbulent flow [11]

where ϕ' can be velocity fluctuating components or some scalar components (such as temperature, density etc.). In case of the momentum equation, these terms are called Reynolds stresses. Reynold stresses are proportional to mean strain rates, as turbulence increases with the increase in the shear rate. Using suffix notation the mathematical form can be given as [11]:

$$\tau_{ij} = -\rho\overline{u'_i u'_j} = \mu_t \left(\frac{\partial U_i}{\partial x_j} + \frac{\partial U_j}{\partial x_i} \right) - \frac{2}{3}\rho k \delta_{ij} \tag{4.17}$$

where μ_t is known as eddy viscosity, Kronecker delta $\delta_{ij} = 1$ if $i = j$ and $\delta_{ij} = 0$ if $i \neq j$ [11].

In a similar manner, turbulent transport of scalar quantities is modelled as [11]:

$$-\rho\overline{u'_i \phi'_j} = \Gamma_t \frac{\partial \Phi}{\partial x_i} \tag{4.18}$$

where Φ represents the mean scalar quantity and Γ_t represents the turbulent diffusivity.

Typically, if the Reynolds Number of the flow exceeds a certain threshold value, transition from laminar to turbulent flow occurs. Turbulent flow characterized by eddies and vortices can cause additional mixing of particles resulting in more effective mixing/ transfer of mass, momentum and energy. This can cause higher diffusion coefficients of mass momentum and energy [11].

4.2.1 Mixture $k - \varepsilon$ Model

In order to model the effects of turbulence the k- ε model is used, where k represents the turbulent kinetic energy and ε represents turbulent kinetic energy dissipation term. The turbulent kinetic energy and its dissipation term

characterize the velocity and the length scale of the eddies of the turbulent flows as [11, 42]:

$$\vartheta = k^{1/2}$$
$$\ell = \frac{k^{3/2}}{\varepsilon}$$

where ϑ and ℓ are the characteristic velocity and length scale of the turbulent eddies of the flow respectively. Eddy viscosity of the mixture is given as [11, 42]:

$$\mu_{t,m} = C\rho\vartheta\ell = \rho C_\mu \frac{k^2}{\epsilon} \tag{4.19}$$

The mixture $k-\varepsilon$ model is a slight modification of standard $k-\varepsilon$ model. It makes use of mass averaged velocities and mixture densities for calculation of its transport variables. The respected transport equations are given as [11,42]:

$$\frac{\partial \rho_m k}{\partial t} + \nabla \cdot (\rho_m k \mathbf{u}_m) = \nabla \cdot \left[\frac{\mu_{t,m}}{\sigma_k}\nabla k\right] + 2\mu_{t,m} S_{ij,m} \cdot S_{ij,m} - \rho_m \varepsilon \tag{4.20}$$

$$\frac{\partial \rho_m \varepsilon}{\partial t} + \nabla \cdot (\rho_m \varepsilon \mathbf{u}_m) = \nabla \cdot \left[\frac{\mu_{t,m}}{\sigma_\varepsilon}\nabla \varepsilon\right] + C_{1\varepsilon}\frac{\varepsilon}{k} 2\mu_{t,m} S_{ij,m} \cdot S_{ij,m} - C_{2\varepsilon}\rho_m \frac{\varepsilon^2}{k} \tag{4.21}$$

where $S_{ij,m}$ represent the strain tensor. For $i \neq j$, the components of the tensor are given as [11, 42]:

$$S_{ij,m} = \frac{1}{2}\left(\frac{\partial u_{i,m}}{\partial x_j} + \frac{\partial u_{j,m}}{\partial x_i}\right)$$

for $i = j$, the components are given as:

$$S_{ii,m} = \frac{\partial u_{i,m}}{\partial x_i}$$

The mixture velocity and mixture density are given by equation 4.2 and 4.3 respectively.

The $k-\varepsilon$ model is a semi-empirical model with constants used in equations. Values of the constants for a wide range of flows need not to be fixed or adjusted. The constants used in the current work are given in table 4.1 [11].

C_μ	σ_k	σ_ϵ	$C_{1\epsilon}$	$C_{2\epsilon}$
0.09	1.00	1.30	1.44	1.92

Table 4.1: Values of $k - \varepsilon$ constants

4.2.1.1 Boundary Conditions

At the inlet, distribution of k and ε must be given. The values are approximated by formulae given below [42]:

$$k = \frac{2}{3}(U_{ref}T_i)^2$$

$$\varepsilon = C_\mu^{3/4}\frac{k^{3/2}}{\ell}, \textit{where } \ell = 0.07\,L$$

In the equations, T_i represents turbulent intensity, and is defined as the ratio of root mean square of velocity fluctuations u' to the mean flow velocity U_{mean}. Mathematically [**?**, a]

$$T_i = \frac{u'}{U_{mean}} = 0.16(Re)^{(-1/8)} \tag{4.22}$$

L represents the characteristic length of the duct, pipe etc. For instance, in case of a circular pipe, L is the diameter of the pipe. Re represents the Reynolds number of the mixture flow. The Reynolds number is a dimensionless number giving the ratio of inertial to viscous forces.

At outlets Neumann boundary conditions $\frac{\partial k}{\partial n} = 0$ and $\frac{\partial \varepsilon}{\partial n} = 0$ need to be fixed.

4.2.2 Physical properties

The physical properties of fluids dictate their response to different forces (mechanical, thermal etc.) applied to them. The most general properties that are used in the mathematical framework to describe a fluid are given below:

4.2.2.1 Specific heat

Specific heat is defined as the amount of heat required to raise the temperature of a unit mass of a substance by one degree. The specific heat (capacity) value depends on how the heat has been added to the system. Thermodynamically, there can be many ways heat is added to raise the temperature by a unit degree, but usually two specific heat capacities are defined and used widely i.e specific heat at constant volume and specific heat at constant pressure. Mathematically [43]:

$$C_p = \left(\frac{\partial h}{\partial T}\right)_p \tag{4.23}$$

$$C_v = \left(\frac{\partial u}{\partial T}\right)_v \tag{4.24}$$

where C_p and C_v represent specific heat at constant pressure and constant volume respectively, h and u represent the specific enthalpy and specific internal energy respectively. In case of a multicomponent mixture, the specific heat of the mixture is calculated as mass weighted average of the components. Mathematically [42]:

$$C_p = \frac{\sum_{k=1}^{n} \alpha_k \rho_k C_{pk}}{\sum_{k=1}^{n} \alpha_k \rho_k} \tag{4.25}$$

where C_{pi} represents the specific heat of the ith component of the mixture.

4.2.2.2 Thermal conductivity

Thermal conductivity of a material is defined as the ability to conduct heat. In case of a multi-component mixture fluid, thermal conductivity is calculated as [42]:

$$\kappa = \sum_{k=1}^{n} \alpha_k \kappa_k \tag{4.26}$$

where κ_k represents the specific heat of the kth mixture phase.

4.3 Numerical Method

It is important to note that all the conservation equations (except for the continuity equation) can be conveniently re-written in the form of the following generic transport equation:

$$\frac{d}{dt}\int_V \rho\phi dV + \int_S \rho\phi \mathbf{u}\cdot\mathbf{ds} = \int_{\mathbf{S}} \mathbf{\Gamma}_\phi \nabla\phi \cdot \mathbf{ds} + , \int_S \mathbf{q}_{\phi\mathbf{S}}\cdot\mathbf{ds} + \int_{\mathbf{V}} \mathbf{q}_{\phi\mathbf{V}}\mathbf{dV} \tag{4.27}$$

while the continuity equation is combined with momentum equation to obtain an equation for pressure or pressure correction. Here ϕ stands for the transported property, e.g. Cartesian components of the velocity vector in fluids $\mathbf{u}_i$, thermal energy e, etc. The meaning of the quantities are given in table 4.2. The term $\mathbf{q}_{\phi S}$ contains portions of mass or heat flux vector or the stress tensor which are not contained in $\Gamma_\phi \nabla\phi$ while $q_{\phi V}$ contains volumetric source terms.

The possibility to express all transport equations in the form of a single prototype equation 4.27 which together with the appropriate initial and boundary conditions forms the complete mathematical model greatly facilitates the discretization procedure.

ϕ	Γ_ϕ	$\mathbf{q}_\phi\mathbf{s}$	$\mathbf{q}_\phi\mathbf{v}$
$\mathbf{u}_i$	μ_{eff}	$[\mu_{eff}(\nabla\mathbf{u}_m)^T - p\mathbf{I}\cdot\mathbf{i_i}$	ρg
h	$\alpha_k(k_k + k_t)$	0	$S_h = -\sum_{k=1}^{n}\alpha_k h_k R_k$
k	$\frac{\mu_{t,m}}{\sigma_k}$	$2\mu_{t,m}S_{ij,m}\cdot S_{ij,m}$	$-\rho_m\varepsilon$
ϵ	$\frac{\mu_{t,m}}{\sigma_\varepsilon}$	$C_{1\varepsilon}\frac{\varepsilon}{k}2\mu_{t,m}S_{ij,m}\cdot S_{ij,m}$	$-C_{2\varepsilon}\rho_m\frac{\varepsilon^2}{k}$

Table 4.2: The meaning of terms in the generic transport equation for different conservation equations

4.4 Discretization Principles

All numerical methods, including the Finite Volume Methods (FVM), involve transforming the mathematical model into a system of algebraic equations. However, before an integration method for the generic transport equation 4.27 is attempted, several important decisions have to be made, concerning (1) the choice of vector and tensor components, (2) the space and time discretization procedure, and (3) the variable storage arrangement. An appropriate decision about these options is decisive for the stability, conservativeness, and efficiency of the numerical method. The following choices are made:

- Although the analysis is carried out in a coordinate-free (invariant) form (which enables any vector and tensor components to be used), vectors and tensors will be expressed through their Cartesian components. They lead to a strong conservation form of all equations (including momentum equation), and the method is not sensitive to mesh smoothness

- The space is discretized by an unstructured mesh with polyhedral control volumes (see figure 4.2). In order to allow the greatest flexibility in adapting the mesh to complex 3D geometries, polyhedra with any number of sides ($n \geq 4$) are allowed, and cells of different topology may be used in the same problem. However, for accuracy reasons the hexhedra are preferred and used wherever possible. This also facilitates the local (cell-wise) grid refinement, which is essential for accuracy reasons.

- All dependent variables are stored at the cell center, i.e. a co-located variable arrangement is used. This requires only one set of control volume to be generated, which facilitates implementation of boundary conditions, multigrid methods, and local grid refinement.

Equation 4.27 when written for the control volume in figure 4.2, gets the following form:

$$\underbrace{\frac{d}{dt}\int_V \rho\phi dV}_{\text{Rate of change}} + \underbrace{\sum_{j=1}^{n_f}\int_{S_j}\rho\phi\mathbf{u}\cdot\mathbf{ds}}_{\text{Convection}} = \underbrace{\sum_{j=1}^{n_f}\int_{S_j}\Gamma_\phi\nabla\phi\cdot ds}_{\text{Diffusion}} + \underbrace{\sum_{j=1}^{n_f}\int_{S_j}\mathbf{q}_{\phi\mathbf{S}}\cdot\mathbf{ds} + \int_{\mathbf{V}}\mathbf{q}_{\phi\mathbf{V}}\mathbf{dV}}_{\text{Sources}}, \tag{4.28}$$

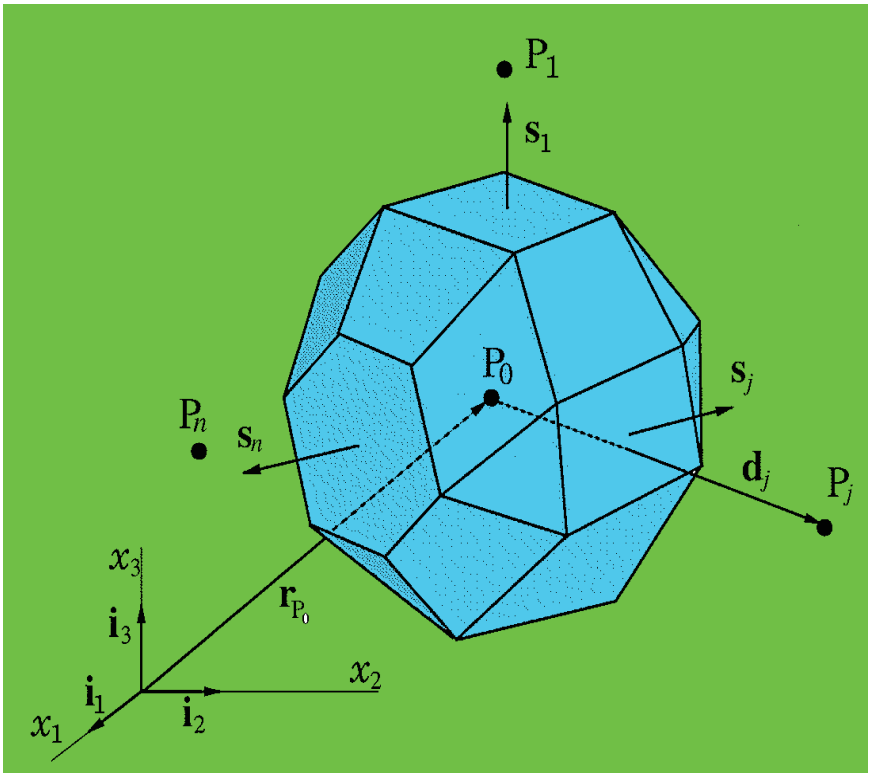

Figure 4.2: Arbitrary control volume (CV) [12]

where n_f is the number of faces enclosing the CV. Equation 4.28 has four distinct parts: transient rate change, convection, diffusion and sources. The equation is exact, i.e. no approximation has been introduced so far. However, in order to evaluate integrals in the above equation, the following steps need to be performed:

- generation of a numerical grid and calculation of geometric data needed for evaluation of surface and volume integrals
- choice of quadrature approximations for surface and volume integrals

- choice of interpolation functions for spatial distribution of variables
- choice of numerical differentiation approximations
- choice of time integration schemes
- some means of determining surface velocities $\mathbf{v_s}$ has to be provided.

4.4.1 Numerical Grid

The solution domain is subdivided into a finite number contiguous CVs by a numerical grid. The CVs are defined by their vertices, which are joined by straight edges, since the curvature plays no role in the present discretization method. The edges define CV faces, which form a CV surface.

4.4.1.1 Surface vector

Since the edges of the CV are straight lines, the projections of the faces onto Cartesian coordinate surfaces are independent of the actual shape of the surface. They represent the Cartesian components of the surface vector, which are calculated by subdividing the cell face into triangles (whose surface vectors are easily computed):

$$s_j = \frac{1}{2}\sum_{i=3}^{n_j^v}[(r_{i-1} - r_1) \times (r_i - r_1)] \tag{4.29}$$

where n_j^v represents the number of vertices in cell face j and $\mathbf{r}_i$ is the position vector of the vertex i. Note that there are n_j^{v-2} triangles. The choice of the common vertex ($\mathbf{r}_1$) is not important.

4.4.1.2 Cell Volume

The volume of an arbitrary control volume can be calculated using Gauss' Theorem:

$$\int_V \nabla \mathbf{r}\, \mathbf{dV} = \int_{\mathbf{S}} \mathbf{r} \cdot \mathbf{ds} \Rightarrow \mathbf{V_{P_o}} = \frac{\mathbf{1}}{\mathbf{3}}\sum_{\mathbf{j=1}}^{\mathbf{n_f}} \mathbf{r_j} \cdot \mathbf{s_j} \tag{4.30}$$

where $\mathbf{r_j}$ denotes the position vector of the cell face center j and $\mathbf{s_j}$ is the cell face surface vector. The surface integral is approximated using midpoint rule. In order to avoid overlapping of CVs, the cell-face center and its surface vector have to be uniquely defined.

4.4.1.3 Computational and Boundary Nodes

Computational nodes at which the variable values are to be calculated are placed at the center of each CV, while boundary nodes-necessary for the specifications of the boundary conditions-are placed at the centers of boundary faces.

4.4.2 Calculation of Integrals

The surface and volume integrals in equation 4.28 have to be evaluated using some quadrature approximations. Two levels of approximation are involved: (i) the integral is expressed as a function of the integrand value at one or more locations within the integration domain, and (ii) these values have to be expressed through the values at computational points (CV centers) in order to obtain an algebraic equation system.

The simplest integral approximation of second order is the midpoint rule. The integral is approximated by the product of the integrand at the center of the integration domain and the surface or volume of the domain.

$$\int_{S_j} \mathbf{f} \cdot \mathbf{ds} \approx \mathbf{f_j} \cdot \mathbf{s_j}, \int_{\mathbf{V}} f \, \mathbf{dV} \approx f_{\mathbf{P_o}} \, \mathbf{V_{P_o}} \tag{4.31}$$

where $\mathbf{f}$ and f are arbitrary vector and scalar, respectively.

4.4.3 Spatial Variation

Variable values and fluid properties are available at the computational nodes which lie at the CV centers. However, often these quantities are needed at locations other than cell centers. For this, interpolation has to be used. Any kind of shape function could be used; here the simplest second-order approximation, namely linear distribution is chosen:

$$\psi(\mathbf{r}) = \psi_{\mathbf{P_o}} + (\nabla\psi)_{\mathbf{P_o}} \cdot (\mathbf{r} - \mathbf{r_{P_o}}) \tag{4.32}$$

where ψ stands for the dependent variable ϕ, physical properties of continuum, or gradient of ϕ; $\mathbf{r_{P_o}}$ is the position vector of CV center P_o.

4.4.3.1 Cell-face values

In order to calculate surface integrals, variable values at cell-face centers are required. Since the expression 4.32 would lead to a different value at the cell-face center when applied in CVs on wither side of the face, a unique symmetric expression is used when cell-face values are calculated:

$$\psi_j = \frac{1}{2}(\psi_{P_o} + \psi_{P_j}) + \frac{1}{2}[(\nabla\phi)_{P_o} \cdot (\mathbf{r_j} - \mathbf{r_{P_o}}) + , \\ (\nabla\phi) \cdot (\mathbf{r_j} - \mathbf{r_{P_j}}))] \tag{4.33}$$

In the equation above $\mathbf{r_j}$ is the position vector of the cell-face center. P_j denotes the center of the neighbour CV. The first term on the right-hand side gives the value at the location midway between cell centers on a straight line connecting P_o and P_j. The second term provides correction which takes into account that the cell-face center may not lie on the line connecting cell centers and / or not lie at the midpoint.

4.4.3.2 Gradient Calculation

A simple and efficient way of calculating gradients at CV centers to within second-order accuracy is based on the Gauss' divergence theorem and the midpoint-rule integral approximation:

$$\int_V \nabla\psi dV = \int_S \psi \mathbf{ds} \Rightarrow (\nabla\psi)_{\mathbf{P_o}} \approx \frac{\mathbf{1}}{\mathbf{V_{P_o}}} \sum_{\mathbf{j=1}}^{\mathbf{n_f}} \psi_{\mathbf{j}} \mathbf{S_j} \tag{4.34}$$

where ψ_j is the value of ψ at the cell-face center j.

4.4.4 Time Integration

Equation 4.28 can be rearranged into the following form:

$$\frac{d\Psi}{dt} = F(\phi) \tag{4.35}$$

where,

$$\Psi = \int_V \rho\phi dV \approx (\rho\phi)_{P_o} V_{P_o} and\, \phi = \phi(\mathbf{r}, \mathbf{t}) \tag{4.36}$$

The left hand side of equation 4.35 can be integrated from t_{m-1} to t_m (where $t_m = t_{m-1} + \delta t$). The right hand side requires an approximation of mean value of F over the interval δt_m.

4.4.4.1 Euler Implicit Scheme

This scheme uses the current value of F. Thus, the quantity Ψ at time t_m is calculated as:

$$\Psi^m = \Psi^{m-1} + F^m \delta t_m \tag{4.37}$$

where $F^m = F(\phi^m)$ and $\phi^m = \phi(\mathbf{r}, \mathbf{t_m})$. This is a first-order fully-implicit approximation. The convective, diffusive, and source terms are evaluated at the new time level.

4.5 Derivation of Algebraic Equation Systems

In this section the step by step derivation of the algebraic equation system as a discrete approximation of the conservation equation 4.28 will be described, using principles introduced in the preceding section.

4.5.1 Rate of Change

The estimated value of the rate of change term in equation 4.28 depends on the discretization scheme used.

4.5.1.1 Euler Implicit Scheme

The transient term in equation 4.28 in the case of the Euler implicit scheme is approximated as:

$$\frac{d}{dt}\int_V \rho\phi dV \approx \frac{(\rho\phi V)_{P_o} - (\rho\phi V)_{P_o}^{m-1}}{\delta t_m} \tag{4.38}$$

4.5.2 Convective flux

The convective flux of the variable ϕ through the internal cell-face j represents the rate at which it is transported into (or our of) the control volume by the fluid motion relative to CV boundary. This term is nonlinear and requires linearization prior to solution:

$$C_j = \int_{S_i} \rho\phi\mathbf{u}\cdot d\mathbf{s} \approx \dot{m}_j\phi_j^*, \tag{4.39}$$

Where ϕ_j^* stands for the value at the cell-face center and $\dot{m}_j$ is the mass flux through the cell face:

$$\dot{m}_j = \int_{S_i} \rho\mathbf{u}\cdot d\mathbf{s} \approx \rho_j^*\mathbf{u}_j^*\cdot s_j \tag{4.40}$$

The way in which the cell-face values of the convected variable ϕ_j^*, density ρ_j^*, and velocity $\mathbf{v}_j^*$, are calculated has a strong influence on both the accuracy and stability of the numerical method. The calculation of ϕ_j^* is described next, while $\mathbf{v}_j^*$ and ρ_j^* are obtained from special interpolation practices which ensure strong coupling of velocity, density, and pressure and lead to a stable solution procedure.

4.5.2.1 First-order Upwind Differencing

The upwind scheme (UD) relies on the donor-acceptor concept. According to it, the value of the dependent variable ϕ at the cell-face j is equal to the value of the upstream cell center:

$$\phi_j^{UD} = \begin{cases} \phi_{P_o} & \text{when the flow is from } P_o \text{ to } P_j \\ \phi_{P_j} & \text{when the flow is from } P_j \text{ to } P_o \end{cases}$$

According to the scheme, the donor cell gives to the acceptor cell what it has as a mean value. The approximation is based on transported property of flow and always results in solutions which are bounded. However, the scheme undermines the complex spatial variation of dependent variables which is rarely constant within a cell. This results in the first-order accuracy of the scheme and an excessive numerical diffusion.

4.5.2.2 Second-order Central Differencing

The assumption of a linear variation of the dependent variable leads to a second-order discretization scheme. The cell-face value based on the expression.

$$\phi_j^{CD} = \frac{1}{2}(\phi_{P_o} + \phi_{P_j}) + \frac{1}{2}\left[(\nabla\phi)_{P_o} \cdot (\mathbf{r_j} - \mathbf{r_{P_o}}) + (\nabla\phi)_{\mathbf{P_j}} \cdot (\mathbf{r_j} - \mathbf{r_{P_j}})\right] \quad (4.41)$$

This second order accurate and corresponds to the standard central difference (CD) approximation on structured grids.

4.5.3 Diffusive Flux

Diffusive flux D_j of ϕ through am internal cell-face j can be approximated as (using midpoint rule approximation of the surface integral):

$$D_j = \int_{S_j} \Gamma_\phi \nabla\phi \cdot ds \approx \Gamma_{\phi,j}(\nabla\phi)_j^* \cdot \mathbf{s_j} \quad (4.42)$$

where $\Gamma_{\phi,j}$ stands for the value of the diffusivity at the cell-face center, obtained using interpolation formula 4.32. The approximations of the gradient of ϕ based on expression 4.34 are second-order space-centered and as such cannot sense the oscillations which have the period twice the characteristic length of the numerical mesh. As as result, once induced unphysical oscillatory profile(which might happen during iterations) remains superimposed onto the otherwise smooth spatial variation of the dependent variable. Because of this, a third-order dissipative term is added to the interpolated value:

$$(\nabla\phi)_j^* = (\nabla\phi)_j + \left(\frac{\phi_{P_j} - \phi_{P_o}}{|\mathbf{d_j}|} - \frac{\overline{\nabla\phi} \cdot \mathbf{d_j}}{|\mathbf{d_j}|}\right)\frac{|\mathbf{d_j}|\mathbf{s_j}}{\mathbf{d_j} \cdot \mathbf{s_j}} \quad (4.43)$$

where the over bar denotes arithmetic average of values calculated at nodes P_o and P_j and the value $(\nabla\phi)_j$ is calculated using second-order formula 4.32. This additional term represents the difference between second-order central difference approximation of the derivative in the direction of vector $\mathbf{d}_j$ and the

value obtained by interpolating cell-center gradients. It vanishes if the spatial variation of ϕ is linear or quadratic; otherwise, its magnitude is proportional to the second-order truncation error of the scheme and reduces accordingly with grid refinement. The correction term detects and smooths out any unphysical oscillations that might occur in the iteration process.

While the terms in brackets in equation 4.43 adds up to a small value when the variation of ϕ is smooth, each term on the right hand side is actually of the same order. The first term in brackets involves only the nearest neighbour and its contribution is treated implicitly. The other two terms represent together the contribution due to the component of the gradient vector normal to the distance vector $\mathbf{d}_j$ (the so-called cross-diffusion), which vanishes when the grid if orthogonal. It is small compared to the so-called 'normal diffusion' if the grid non-orthogonality is not severe and is treated explicitly. This is also a kind of deferred correction approach, aimed at using only the nearest neighbours in the coefficient matrix.

The geometric factor multiplying the terms in brackets in equation 4.43 is chosen to recover the discretized diffusion flux obtained in the case of discretization in general curvilinear coordinates on structures grids, which correctly reflects the covariant nature of the diffusion flux vector.

4.5.4 Source Terms

4.5.4.1 Surface integral

The surface integrals involving the vector $\mathbf{q}_{\phi S}$ are calculate explicitly over each cell face using the midpoint rule and have the form:

$$Q_{\phi S} = \int_S \mathbf{q}_{\phi S} \cdot s\mathbf{s} \approx \sum_{j=1}^{nf} \left(\left[\mu_{\text{eff}} (\nabla \mathbf{u})^T - p\mathbf{I} \right]_j \cdot \mathbf{i}_i \right) \cdot \mathbf{s}_j \tag{4.44}$$

where $\mathbf{i}_i$ $(i = 1, 2, 3)$ are the Cartesian base vectors. It may also be beneficial, form stability and efficiency point of view, to take some parts of the source $Q_{\phi S}$ into account implicitly.

4.5.4.2 Volume Integral

The part of the source term coming from the true, volume sources is integrated using the midpoint rule, which is equivalent to assuming a linear variation of the source over the CV:

$$Q_{\phi V} = \int_V \mathbf{q}_{\phi V} dV \approx (\mathbf{q}_{\phi V})_{P_o} V_{P_o} \tag{4.45}$$

The volumetric source term $Q_{\phi V}$ is often a non-linear function of ϕ. If it can be linearized so that a positive contribution to the coefficient of ϕ_{P_o} is obtained in the final algebraic equation, one part is treated implicitly.

4.5.5 Boundary and Initial Conditions

The expressions for the evaluation of the convective and diffusive fluxes described above are valid for all interior cell faces. On the faces coinciding with the boundary of the solution domain S , boundary conditions have to be applied. All boundary conditions can be classified as being Dirichlet or Neumann type. In any case, the integrals over boundary surface are expressed as a function of the known boundary data and unknowns from the interior.

In the case if Dirichlet boundary conditions, the convective fluxes are calculated by replacing ϕ_j^* in 4.39 by the boundary value ϕ_B, and diffusive fluxes by replacing ϕ_{P_j} in 4.43 and in calculating $(\nabla\phi)_{P_o}$ by the boundary value ϕ_B. On the boundary region where Neumann boundary conditions are prescribed, the diffusive fluxes can be calculated directly, while the variable values at the boundary are obtained from the discretized gradient approximation.

4.5.6 Resulting algebraic equations

After assembling all the terms featuring in equation 4.27, there results one linear algebraic equation per CV and unknown which links the value of the dependent variable ϕ at the CV center with its values at the centers of the neighbour CVs:

$$a_{\phi_o}\phi_{P_o} - \sum_{j=1}^{n_i} a_{\phi j}\phi_{P_j} = b_\phi \tag{4.46}$$

where n_i is the number of internal cell faces surrounding cell $\mathbf{P}_o$ and the right hand side b_ϕ contains source terms and contributions from boundary faces and convective and diffusive fluxes which are for the sake of computational efficiency treated explicitly using deferred correction approach:

$$a_{\phi_j} = \Gamma_{\phi_j}\frac{\mathbf{s}_j \cdot \mathbf{s}_j}{\mathbf{d}_j \cdot \mathbf{s}_j} - min(\dot{m}_j, 0),$$

$$a_{\phi_o} = \sum_{j=1}^{n_f} a_{\phi j} + a_{\phi t}$$

$$b_\phi = \sum_{j=1}^{n_f} \Gamma_{\phi_j}\Big((\nabla\phi)_j \cdot \mathbf{s}_j - \overline{\nabla\phi} \cdot \mathbf{d}_j \frac{\mathbf{s}_j \cdot \mathbf{s}_j}{\mathbf{d}_j \cdot \mathbf{s}_j}\Big) -$$

$$\sum_{j=1}^{n_f} \frac{\gamma_\phi}{2}\dot{m}_j\Big((\mathbf{r}_j - \mathbf{r}_{P_o}) \cdot (\nabla\phi)_{P_o} + (\mathbf{r}_j - \mathbf{r}_{P_j}) \cdot (\nabla\phi)_{P_j} +$$

$$(\phi_{P_j} - \phi_{P_o})sgn(\dot{m}_j)\Big) + q_{\phi S} + q_{\phi V} + \sum_{B=1}^{n_B} a_{\phi_B} + q_{\phi_t}$$

where $n_B = n_f - n_i$ is the number of boundary faces surrounding cells $\mathbf{P}_o$ and a_{ϕ_t} and q_{ϕ_t} are defined as (for Euler implicit scheme):

$$a_{\phi_t} = \frac{(\rho V)^m_{P_o}}{\delta t_m}$$

$$q_{\phi_t} = \frac{(\rho V \phi)^{m-1}_{P_o}}{\delta t_m}$$

for all conservation equations.

4.5.7 Calculation of Pressure

In the above described procedure the pressure, featuring in the source term of the fluid momentum equation, has remained unknown, while at the same time no use has been made of the continuity equation. The problem lies in the fact that the pressure does not feature explicitly in the continuity equation which consequently can not be considered as 'an equation for pressure' and the continuity equation for incompressible flows acts just as an additional constraint on the velocity field. This constraint can be satisfied only by adjusting the pressure field. However, pressure is not a conserved property and does not have its governing transport equation, so it is not obvious how this adjustment of pressure is to be performed. At the same time, the pressure source term in the momentum equation is calculated using the second order space centered scheme. As mentioned earlier, such a scheme can produce a correct pressure gradient field, even if the under laying pressure field is contaminated by unphysical oscillations. In order to calculate the pressure field and to couple it properly to the velocity field, a pressure-correction method of SIMPLE-type is used.

4.5.7.1 Cell-face Velocity and Density

The simple and yet efficient way of getting around of the aforementioned problem of pressure oscillation is to calculate the fluid velocity at a cell face in the following manner:

$$\mathbf{u}^*_j = \mathbf{u}_j - \overline{\left(\frac{V_{P_o}}{a_{vo}}\right)} \left(\frac{p_{P_j} - p_{P_o}}{|\mathbf{d}_j|} - \frac{\overline{\nabla p} \cdot \mathbf{d}_j}{|\mathbf{d}_j|}\right) \frac{|\mathbf{d}_j|\mathbf{s}_j}{\mathbf{d}_j \cdot \mathbf{s}_j} \tag{4.47}$$

where $\mathbf{u}_j$ is the spatially interpolated velocity and the rest is a third-order pressure diffusion term which acts as a correction of the interpolated velocity. This correction is negligible if the pressure variation is smooth but becomes large if oscillations in pressure field are present. It introduces pressure in to continuity equation in a manner that allows an easy construction of the pressure -correction equation. The third-order pressure diffusion term in expression 4.47 is analogous to the term introduced by expression 4.43 while the diffusive transport of the variable ϕ was discussed. The correction term vanishes if the

pressure varies linearly or quadratically in space, and is otherwise proportional to the third derivative and the square of mesh spacing. It is thus reducing with grid refinement consistently with other second-order discretization errors.

4.5.7.2 Predictor stage; pressure-correction equation

The so-called predictor stage values of $\mathbf{u}$ and p (featuring in expression for u_j^*), which satisfy the linearized momentum equation, do not necessarily satisfy the continuity equation, which can be, by using the expressions for the rate of change (equation 4.38) and for the mass flux (4.40), written in the following form (for Euler implicit scheme):

$$\frac{(\rho V)_{P_o} - (\rho V)_{P_o}^{m-1}}{\delta t_m} + \sum_{j=1}^{n_\mathrm{f}} \dot{m}_j = 0 \tag{4.48}$$

By employing the colocated version of the SIMPLE algorithm, an equation for pressure correction p' is obtained from the requirement that corrected mass fluxes satisfy the continuity equation:

$$a_{p'_o} p'_{p_o} - \sum_{j=1}^{n_f} a_{p'_j} p'_{p_j} = b_{p'}$$

with the coefficients:

$$a_{p'_j} = \rho \overline{\left(\frac{V_{P_o}}{a_{vo}}\right)} \frac{\mathbf{s_j} \cdot \mathbf{s_j}}{\mathbf{d_j} \cdot \mathbf{s_j}}$$

$$a_{p'_o} = \sum_{j=1}^{n\mathrm{f}} \hat{a}_{P'_j}$$

$$b_{p'} - \sum_{j=1}^{n\mathrm{f}} \dot{m}_j - (pV)_{P_o} - (pV)_{P_o}^{m-1}$$

where all variables have their predictor stage values and a_{vo} is the corresponding momentum equation central coefficient , $\hat{a}_{P'_j}$ is the conjugate of $a_{P'_j}$, i.e. the coefficient related to the cell-face j when P_o and P_j exchange their roles (when the pressure correction equation for cell P_j is constructed).

4.5.7.3 Corrector stage

After the pressure correction p' is obtained, the velocity and pressure are corrected via:

$$\mathbf{u}_{P_o} = \mathbf{u}_{P_o,pred} + \mathbf{u}'_{P_o}$$
$$p_{P_o} = p_{P_o,pred} + \beta_p p'_{P_o}$$

In the equation β_p is the under-relaxation factor. The under-relaxation of pressure correction is necessary because the approximations introduced in deriving the pressure-correction equation in the SIMPLE method result in overestimating the magnitude of p', which in turn leads to slow convergence or divergence of the solution procedure. In the final step, mass fluxes satisfying the continuity equation are calculated as:

$$\dot{m}_j = \dot{m}_{j,pred} + \dot{m'} = \dot{m}_{j,pred} - a_{p'j} p'_{P_j} + a_{\hat{p'}j} p'_{P_o} \tag{4.49}$$

They are used to compute the convective fluxes in the next iteration.

4.5.7.4 Boundary Conditions

The boundary conditions for the pressure correction equation depend on the boundary conditions for the momentum equations. On those portions of the boundary where the velocity is prescribed, its correction is zero which implies a zero-gradient boundary conditions on the pressure correction. If the pressure is prescribed at the boundary, than its correction is zero, leading to a Dirichlet boundary condition for the pressure correction. In the case of incompressible flows, the mass flow rate is usually prescribed so the pressure-correction equation has a Neumann boundary conditions on all boundaries and the sum of sources is equal to zero; the equation them has an infinite number of solutions, all deferring by a constant. This causes no problem since for such flows the absolute pressure level is unimportant-only the gradient is important. The pressure is fixed to a reference value at one cell center and only the differences relative to this node are calculated.

4.5.8 Solution Procedure

Equations of the form 4.46 are obtained for each variable . Due to the non-linearity of the under laying equations, the solution of this system of algebraic equations has to be sought by iterative methods. The equations are also coupled, i.e in each equation more than one unknown appears. One could take the coupling into account by solving the coupled system, but this is rarely done due to the excessive storage and computing time requirements. For this reason the segregated algorithm is adopted.

Equations 4.46 are linearized and temporarily decoupled by assuming that coefficients a_{ϕ_j} and source terms b_ϕ are known (calculated by using dependent variable values from the previous time step). As a result, a subset of linear algebraic equations for each dependent variable is obtained, which can be written in the familiar matrix notation:

$$A_\phi \phi = \mathbf{b}_\phi \tag{4.50}$$

Here A_ϕ is an $N \times N$ matrix vector ϕ contains values of dependent variable ϕ at N nodal points (CV centers) and $\mathbf{b}_\phi$ is the source vector. The linear ma-

trix equation 4.50 usually is solved by iterative methods such as very efficient preconditioned conjugate gradient (CG) methods [44].

Chapter 5

Assessment of Hydrate Formation Model

5.1 Conceptual Picture of the Scenario

Pipelines carrying natural gas with some moisture content are at risk of hydrate formation at some point and time. Figure 5.1 shows a conceptual picture of the phenomena that can occur inside such a pipeline. If the medium surrounding the pipeline is considered to be an infinite heat sink, the temperature of pipe wall and bulk fluid in the pipeline drops. Water vapour in the gas stream condenses at the wall resulting in wetting of the wall and accumulation at the bottom. If the temperature of the thin gas-saturated liquid film drops below the hydrate formation temperature, the hydrate nuclei begin to appear in the thin (condensed water)film. Sloan et al. [1, 7] state their observations during the experiments performed by them, that the hydrate formation phenomena is primarily within the thin layer of water in proximity of the gas. The reason given is that water impregnation by gas is maximum in the thin water layer next to gas. On this pretext, it is fair to assume that the water condensed at the walls (very thin layers) and accumulated at the bottom of the pipe is saturated with natural gas. Due to proximity of the thin layer to the pipe wall, the heterogeneous mode of nucleation will be favoured. The thin layer of liquid attains the wall temperature and nucleation may start but eventually as the water trails merge in to accumulated water at the bottom of the pipe, the hydrate nuclei will flow along.

Various mechanisms of hydrate and ice formation and deposition have been addressed by different authors [18,45–48]. While the hydrate (or ice) formation phenomena through orifices, chokes and restrictions primarily is the case of homogeneous nucleation and the hydrate (or ice) particles are entrained in the bulk flow until they get deposited on the walls, the hydrate formation phenomenon in the case considered (as in figure 5.1) is due to heterogeneous nucleation and happens at the walls. The hydrate particles form in the water (at walls) and flow along with the water film.

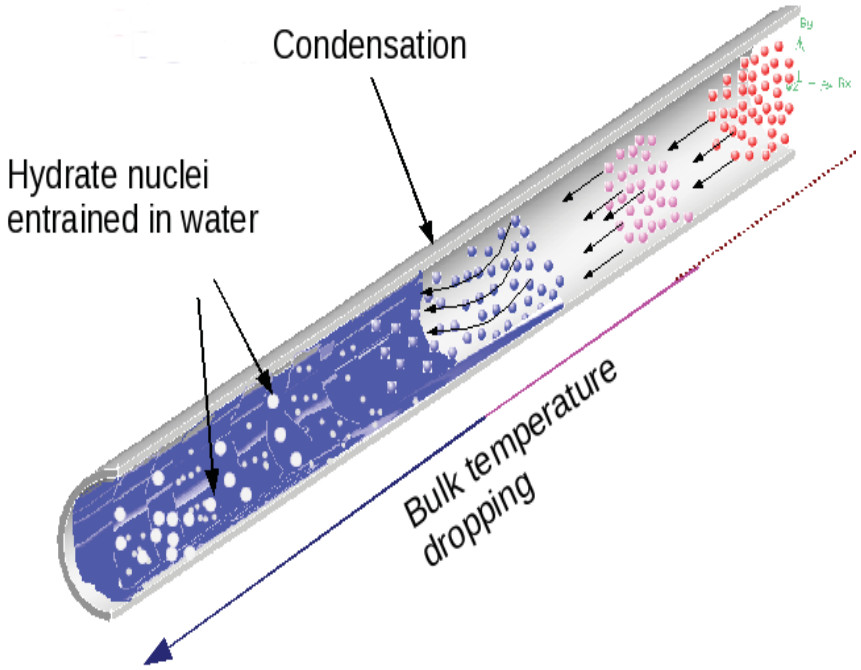

Figure 5.1: Conceptual picture of stages of hydrate buildup and blockage for the present model

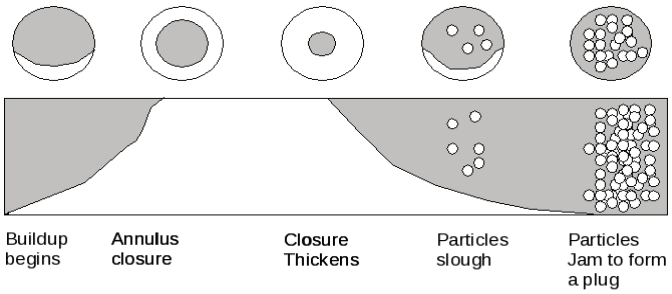

Figure 5.2: Conceptual picture of stages of hydrate buildup and blockage by Sloan et. al [1]

5.2 Thermodynamic Reference Conditions

In a pipeline carrying gas from the wells, there is always some moisture content in varying amounts due to proximity of gas with water (inside formations) while being extracted from wells. If the pipe temperature falls below the dew point of the water vapour corresponding to its partial pressure, the condensation may ensue. In order to model condensation at walls in Fluent [42] an expression developed by DeSchepper et al. [49, 50] is used.

$$M_{water} = 0.1 \times \alpha_{vapour} \times \rho_{vapour} \mid T_{sat} - T_{wall} \mid / T_{sat} \tag{5.1}$$

where α_{vapour} is the vapour volume fraction and $\rho_{vapour}$is the density of vapour. Here the rate of condensation, M_{water} $(kg/m^3 - s)$ depends on the degree of sub-cooling i.e. the difference in the saturation and fluid temperature at the wall. The value of T_{sat} corresponding to the partial pressure of vapour is obtained through a correlation derived from the steam table.

The condensation model takes in to account the amount of water vapour conversion based on the degree of subcooling (corresponding to the partial pressure). The expression to ascertain saturation temperature T_{sat} is derived from steam tables for a particular range of pressure and is given as:

$$T_{sat} = 37.28 \times ln\left(P_{vapour}\right) - 94.04 \tag{5.2}$$

The vapour pressure is calculated by the product of system pressure in the pipe with the vapour volume fraction. As the pipe geometry is divided in to small computational cells (control volumes), during the calculation, the equations are applied to each control volume. During the calculation with a finite volume method, the above correlations are used for each computational cell. Therefore, mass transfer in each computational cell is calculated with time and used in the phase continuity equation mass transfer terms.

The condensation process results in water deposition at the walls and accumulation at the low points in the pipeline. If the temperature falls further, there is a probability of hydrate nuclei to crystallize, as the water is saturated with hydrocarbon gas due to continuous contact at high pressure.

For the cases under consideration, a gas mixture of methane and propane gas was assumed to flow through the pipe section. The equilibrium curve for the mixture is obtained through CSM-Hyd [7], a software for obtaining hydrate equilibrium curve in case of various gas compositions. the graph is shown in figure 5.3.

If the temperature of the water (saturated with gas) at the walls falls below the equilibrium hydrate formation temperature, the probability of hydrate formation increases as the (water-gas) solution is forced in to a metastable state. The degree of subcooling is given as:

$$\Delta T = T_e - T \tag{5.3}$$

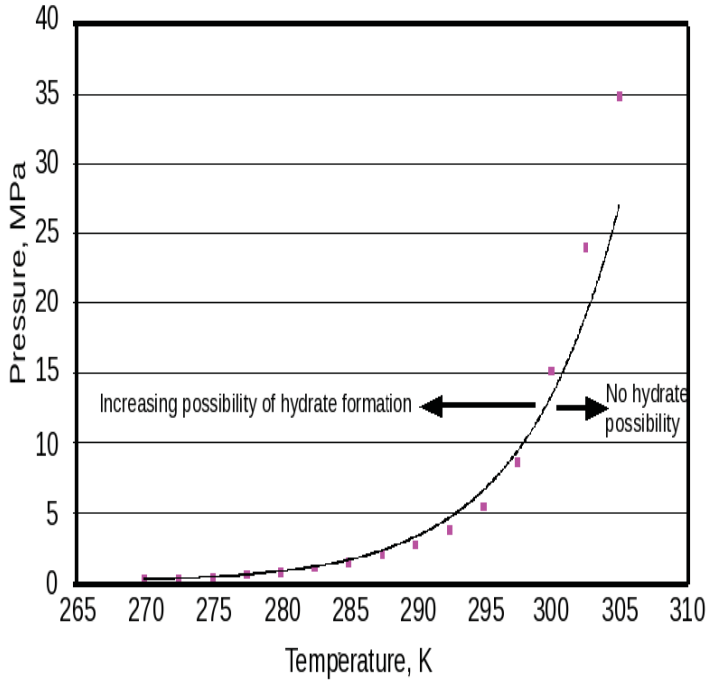

Figure 5.3: Hydrate equilibrium curve for methane and propane mixture

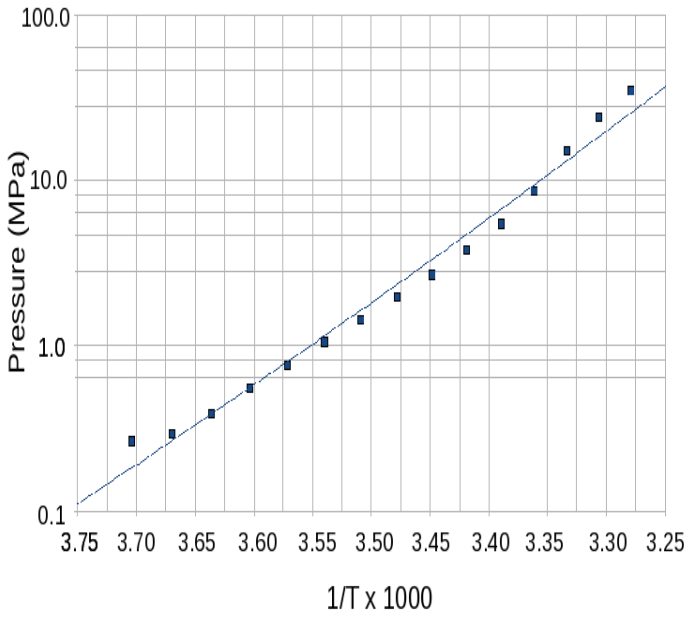

Figure 5.4: Logarithm of pressure versus inverse of absolute temperature for methane-propane mixture

where T_e represents equilibrium temperature and the expression for the driving force is given by (equation 3.17):

$$\Delta\mu = -\frac{\Delta h_e}{T_e}\Delta T \tag{5.4}$$

where Δh_e is obtained from equation 3.27 with the procedure given in section 3.4. Graph is plotted (figure 5.4) for *log* of pressure against inverse of temperature in order to insert in (equation 3.24):

$$\frac{\mathrm{d}ln\,P}{\mathrm{d}(1/T)} = -\frac{\Delta h_e}{zR} \tag{5.5}$$

In order to obtain compressibility factor for the gas mixture, a correlation (equation 5.5) was obtained for compressibility as a function of temperature using the method for gas mixtures by Redlich-Kwong and Soave [40]. The procedure is outlined in section 3.4 and the plot is given in appendix A.

The equation of compressibility factor as a function of temperature was obtained by fitting a curve to the data from using Soave-Redlich-Kwong method. The equation is given as:

$$z = 1.16 \times lnT - 5.92; \tag{5.6}$$

Once the driving force (equation 5.4) is high enough, so that there is a high probability that the sub-critical nuclei surmount the activation barrier (given by equation 3.37 and also below), :

$$\Delta G^*_{het} = \psi(\theta)\frac{16\pi\sigma^3 v_c^2}{3\Delta\mu^2}$$

the nucleation process starts with the nucleation rate as given by expression given by equation 3.58, which in simplified form is given as:

$$J_o = Ae^{\frac{-\Delta\mu+\Delta G^*_{het}}{kT}} \tag{5.7}$$

where A is a pre-factor incorporating all the physics of diffusion phenomena, attachment, detachment etc. as discussed in section 3.6.3.

The nuclei which are born (i.e attain the critical size) not only cross the activation barrier, but grow also in size beyond the critical size. So effectively, there is a rate of increase of hydrate mass by birth of new nuclei, and also by growth of existing nuclei. The growth is dependent again on the degree of metastability (subcooling). The total rate expression for hydrates incorporating rate of nucleation and growth is given by equation 3.72 and the theory explained in section 3.7. The equation is given again below:

$$R(t) = \frac{3}{2}\frac{bN_sA_sJ_oG^{3/2}(t-t')^{1/2}}{V_s}$$

The total rate of hydrate formation can be converted to mass of hydrate formed as discussed in section 3.7.

As the hydrate mass fraction in water grows, the water hydrate slurry thickens. To incorporate the rheological effects of the increase of suspension in the solution, the relationship given below was used [19, 51]. The slurry (mixture of water and hydrate) viscosity is an increasing function of hydrate volume fraction. However, in a cell, the 'effective molecular viscosity' is a volume fraction weighted average of all the species in the cell.

$$\mu_{slurry} = \mu_{water} \left(1 - \alpha_{hyd}\right)^{-2.5} \tag{5.8}$$

where μ represents viscosity and α represents volume fraction.

5.3 Process Flowchart

All the sub-models, i.e the condensation model, the hydrate formation model (nucleation and growth rate) and the rheological model were incorporated making use of User Defined Functions hooked to the main Fluent code. A flow chart describing the decision process for hydrate formation is shown in figure 5.5.

The boundary conditions as depicted in table 5.1 are applied to the domain of the problem. A set of conservation equations are solved in order to ascertain various state variables such as pressure, temperature velocity etc. With the help of the relationships presented in section 5.2, decisions regarding the state of the fluid being in the hydrate prone region (and/or condensation prone region) is done. If the state of the fluid is such that it lies in the regions for hydrate formation or condensation from vapours, the corresponding 'condensation ' and /or 'hydrate' formation subroutine calculates the mass transfer. The hydrate formation decision is further interlocked with the condition of presence of water in the particular computational cell. The amount of hydrate and water formation effects the viscosity of the fluid the effect of which is incorporated in to the transport equations.

For vapour condensation in to water, a further check is made whether the particular computational cell is in the wall region or otherwise. If the cell is in the wall region , and the pressure/ temperature conditions are favourable, the condensation proceeds. In this way, because of the presence of water in the wall region, the hydrate formation is only possible in the proximity of the walls.

It is possible that the temperature of the cell is such that there is only condensation and no hydrate formation, then the rheological model only returns the viscosity of water.

The mass transfer decision mechanism described in the flow chart is applied to each computational cell of the flow domain for each time increment in a transient calculation.

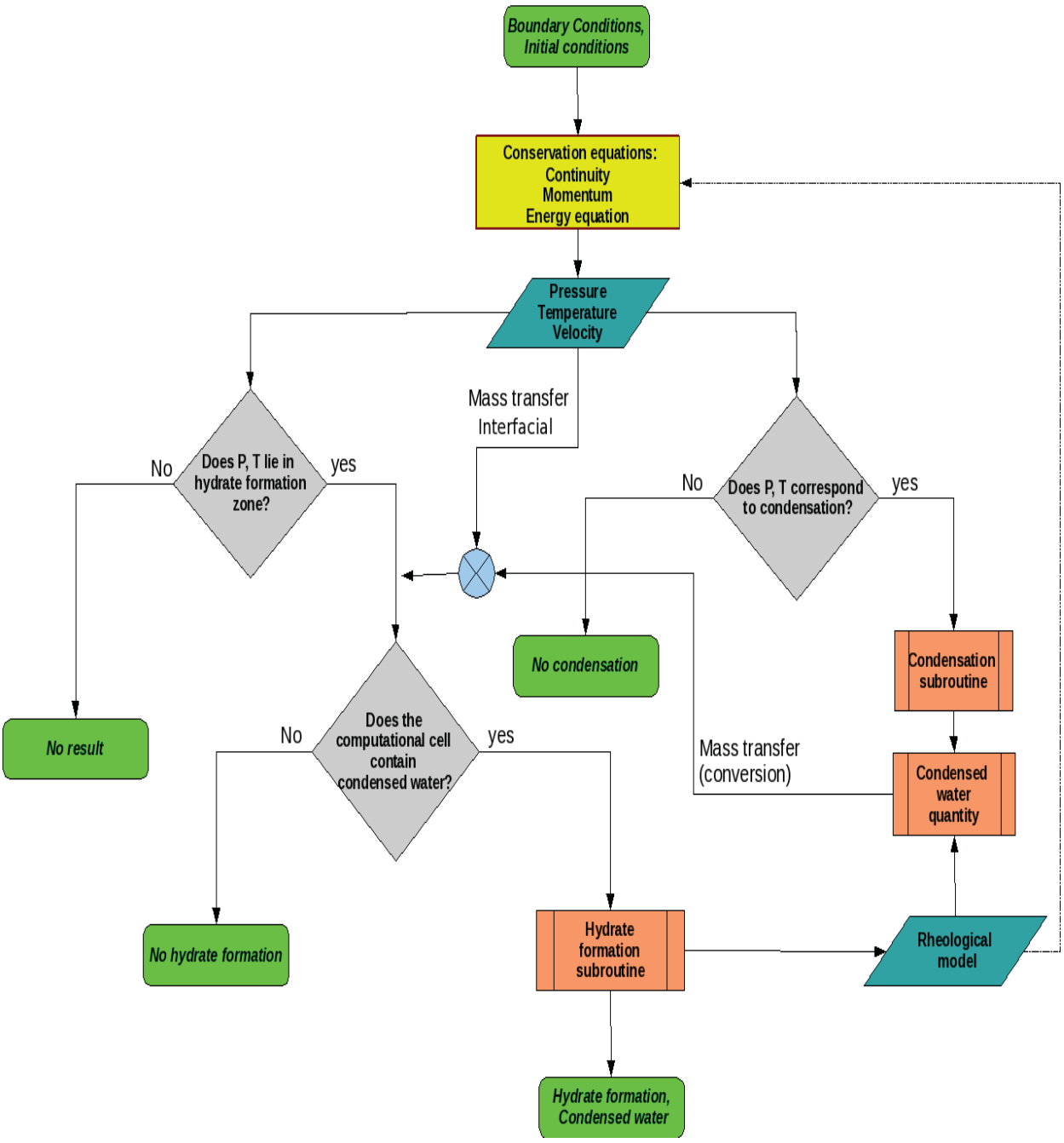

Figure 5.5: Flow chart showing decision process for the User Defined Functions.

5.4 Assessment of The Model

In order to assess the capabilities of the hydrate formation model, an arbitrary pipe line section was considered the pipe geometry and boundary conditions as given in the following sections.

5.4.1 Boundary Conditions

The boundary conditions for the arbitrary pipe section and geometrical properties are given in the table below:

Table 5.1: Model parameters

No.	*Model parameter*	*Value*
1.	Pipe diameter	0.25m
2.	Inlet velocity	2m/s
3.	Water vapor volume fraction	0.1
4.	Inlet temperature	315K
5.	Operating pressure	6.0Mpa
6.	Species	73-27 percent methane-propane mixture
7.	No. of computational cells	250206
8.	Heat flux on pipe walls	-200 W/m^2

5.4.2 Case of Arbitrary Pipeline Section

In order to model hydrate formation in a natural gas pipeline, an arbitrary pipeline section was considered. Figures 5.6 and 5.7 depict the geometrical properties of the pipeline. The pipeline section consists of an inlet section, a lowered section and an outlet section. Furthermore, with respect to the main flow direction the pipeline was assumed to be straight so that a symmetry condition could be applied and only a half section of the pipeline had to be computed. This clearly reduced the computational effort required significantly.

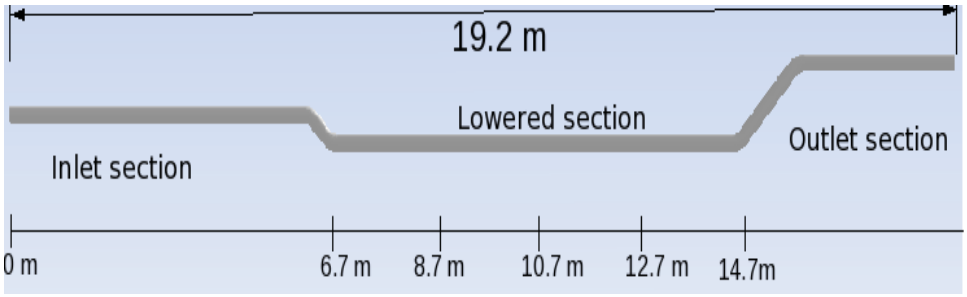

Figure 5.6: Pipe dimensions

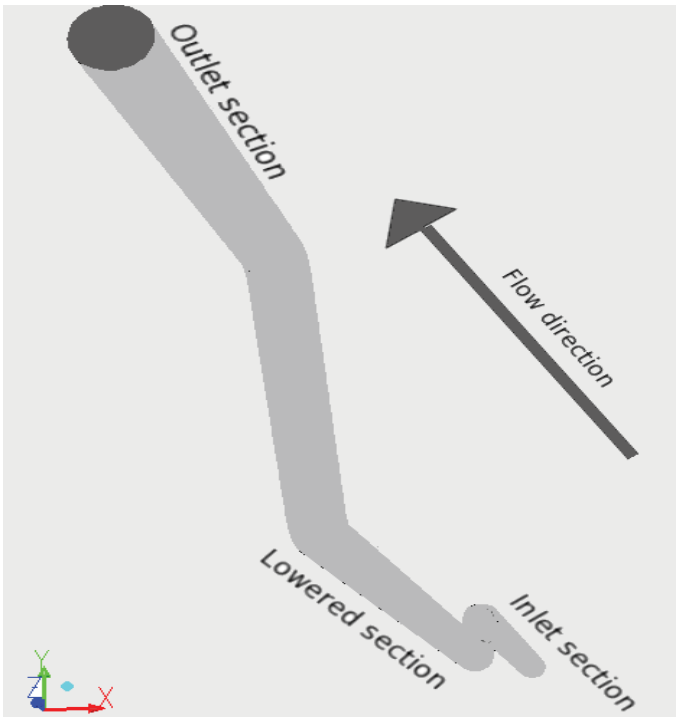

Figure 5.7: Natural gas pipeline

5.5 Results and Discussion

The mixture of gases (natural gas and water vapour) flows along the pipe and at the point where the temperature of the gas near the pipe wall falls below the saturation temperature according to the partial pressure of the gas, the condensation of water vapour occurs. The partial pressure of the vapour is calculated as the product of operating pressure and the vapour fraction.

The driving force for the rate of condensation (eq. 5.5) is the relative temperature difference between the saturation temperature and the wall temperature. The rate of condensation is also dependent on the vapour volume fraction. As the vapour fraction in the gas depletes along the length of the pipe, the partial pressure of the vapour becomes less so that the saturation temperature decreases. Thus, in event of vapour depletion , the rate of condensation along the length decreases or ceases if the temperature drop of the pipe wall is insufficient.

Where in the pipeline, condensation starts, and where it ceases is an important factor with respect to hydrate formation, because it might be that initially as there is enough vapour, there is more condensation and water accumulation in the initial section. Then as the vapour is depleted in the mixture stream and the wall temperature is just equal to or greater than the saturation temperature corresponding to the prevalent partial pressure, the condensation is minimal and the vapour travels along the gas till the time that the drop in the temperature of the gas is enough for the condensation to start again.

The depletion of vapour from the gas stream along the lowered section of the pipeline (and enrichment of hydrocarbon gas) is shown in figure 5.8.

The vapour volume fraction contours are shown on the iso-surface along Z-axis (axial direction) and placed below the pipe-line section for clear visibility. It can be clearly seen that the depletion front of water vapour from the gas mixture marches along the length of the pipe. The volume fraction reduces from 0.1 at the inlet to about 0.098 which means a corresponding drop in the partial pressure of water vapour.

The mutual relation of hydrocarbon gas and water vapour along the lowered section of the pipe is shown in figure 5.9. The figure depicts that the vapour depletes and the hydrocarbon gas is enriched along the length. The drastic changes in the curves from 6.7 m to 7 m and beyond 14.5m is due to vicinity of the wall (due to change in wall direction). The steep slopes in the curves show that due to high rate of condensation, the vapour concentration in the vicinity of the walls is low and high hydrocarbon concentration is present. Vladimir et. al [52] in their work have highlighted the effect of condensation on the accumulation (enrichment) of the non- condensible gases.

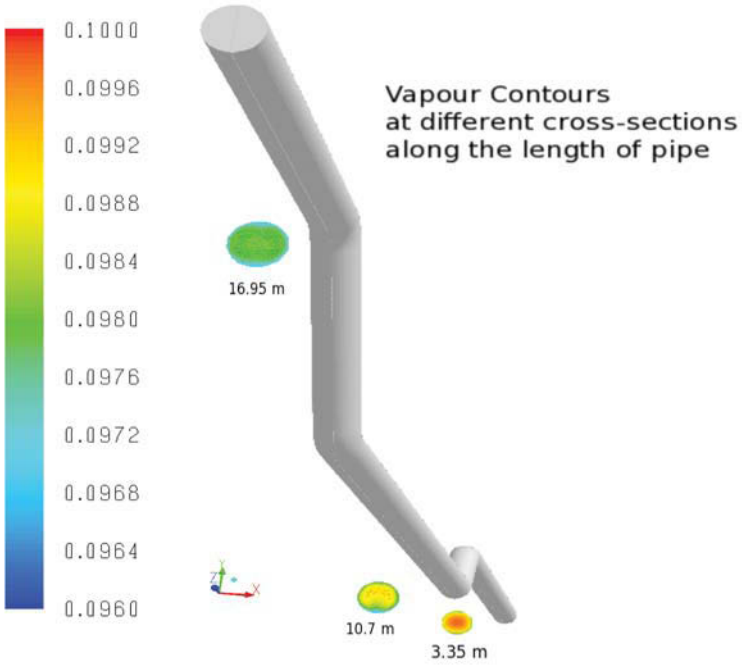

Figure 5.8: Vapour depletion along the length of the pipe (vapour volume fraction)

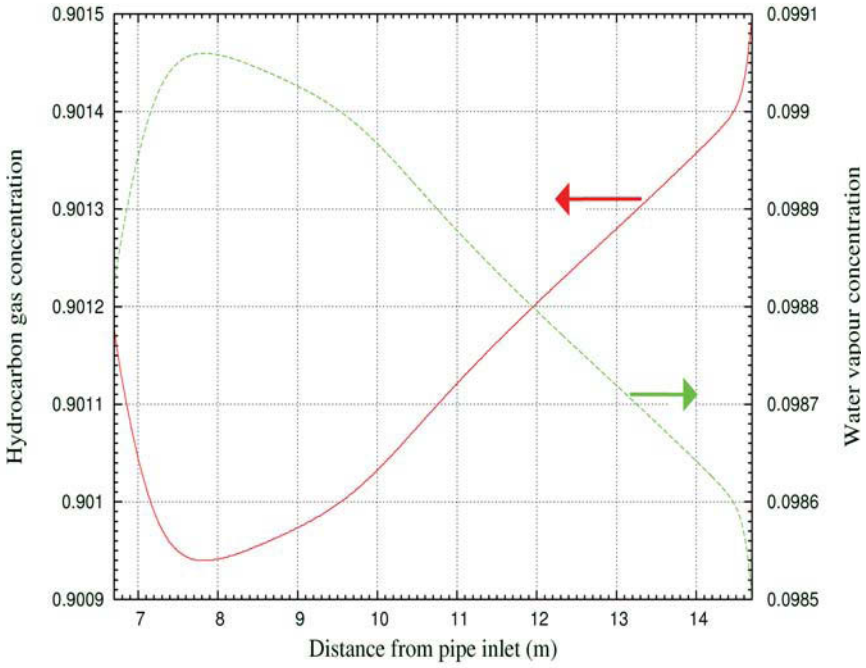

Figure 5.9: Vapour depletion and hydrate enrichment along the lowered section section of the pipe

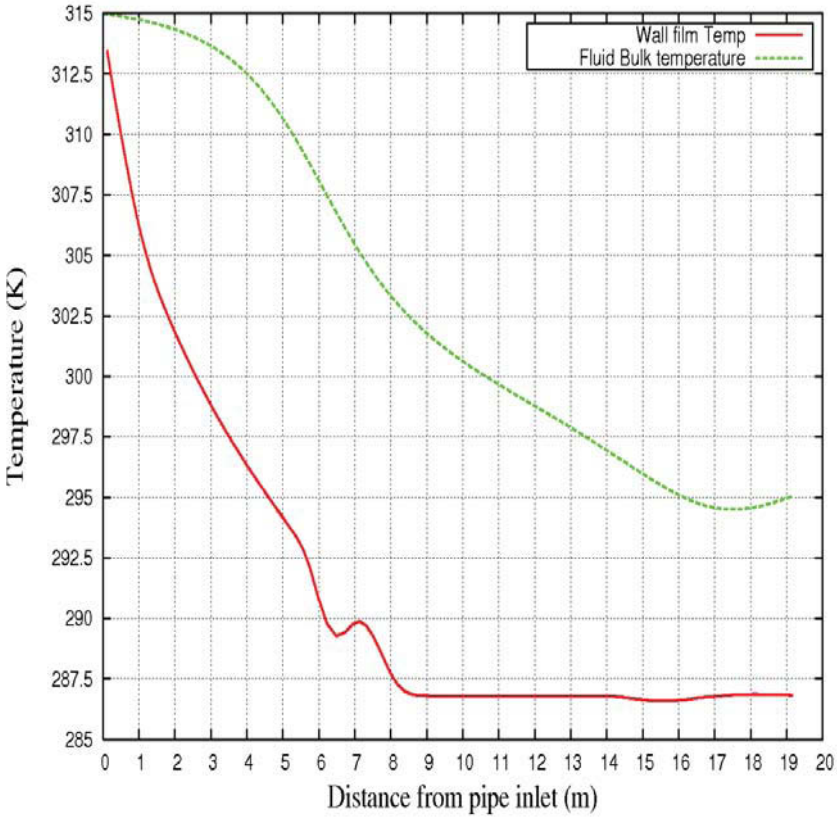

Figure 5.10: Temperature variation along the pipe

Figure 5.10 shows the fluid temperature profiles along the length of the pipe. The two curves represent temperature at the center of the pipe and at the wall (thin film of fluid near wall vicinity approximately at wall temperature) where condensation occurs. The wall film temperature has a steep slope starting from inlet till about 8 m from pipe inlet. The temperature drops at a rate of about $\approx 3.2K/m$, and then stabilizes at about 287 K. The centerline (bulk) temperature experiences a continuous drop from 315 K to about a minimum of 294.8 K. The condensation starts just at about the inlet and continues through out the pipe.

As the condensation proceeds, the water starts to accumulate at the bottom section of the pipe (at 6'o clock) position. In addition to accumulation at the bottom of the pipe, there is an increased accumulation at the base of rising section as depicted in figure. 5.11. While the accumulation at the bottom of the pipe is self evident, the increased accumulation at the base of the rising section is due to the fact that water flowing along the pipe feels a drag force near position where there is an abrupt change in pipe direction thus the direction of the resultant force on the fluid element becomes more steep towards the bottom of the pipe resulting in increased accumulation.

The effects of condensation and water accumulation at the base of the uphill section of the pipe can be clearly seen. In addition to water accumulation at the base of the uphill section, increased water volume fraction can be observed just after the end of the uphill section. This is attributed to water being transported from the base of the uphill section in spurts and then sudden change in the flow direction resulting in increased water mass at the bottom of the pipe just beyond the end of uphill section. As time proceeds, due to condensation and water accumulation the mass of water in the pipe increases. If the water is present at the walls and the temperature is below the hydrate equilibrium temperature, there is a possibility of hydrate formation.

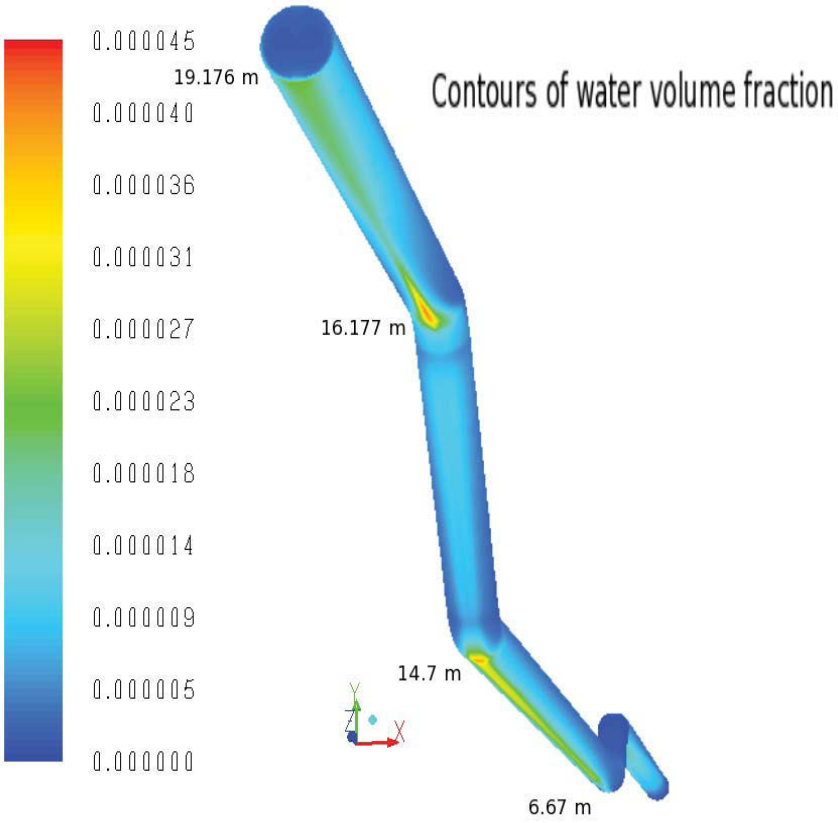

Figure 5.11: Water accumulation at pipe bottom

Figure 5.12 shows mixture velocity (at pipe center) along the length of the pipe. Observing figure 5.11 and 5.12 shows that the position , the slope of the mixture velocity curve starts to increase, water accumulation starts to increase as well. The increase in the slope may be due to the change in pipeline directions, but the reason for water accumulation at certain points and change in the slope of water is the same.

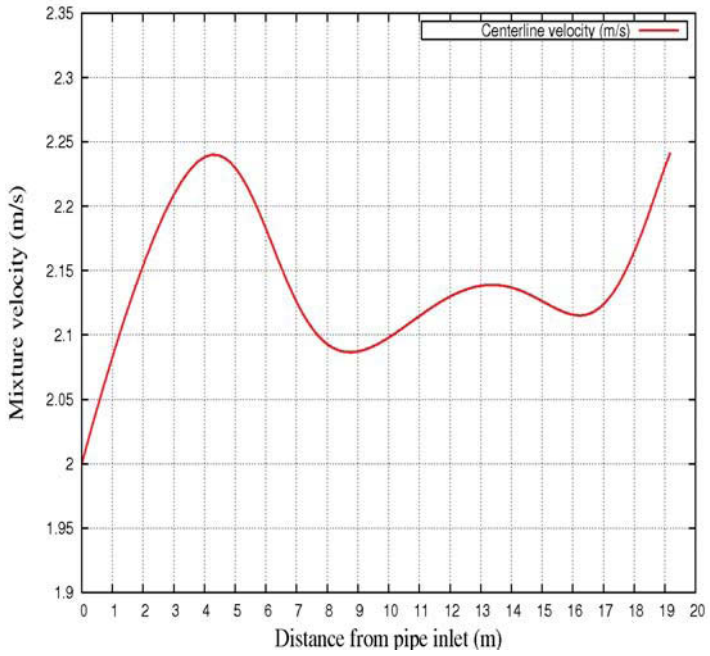

Figure 5.12: Mixture fluid velocity at pipeline center (m/s)

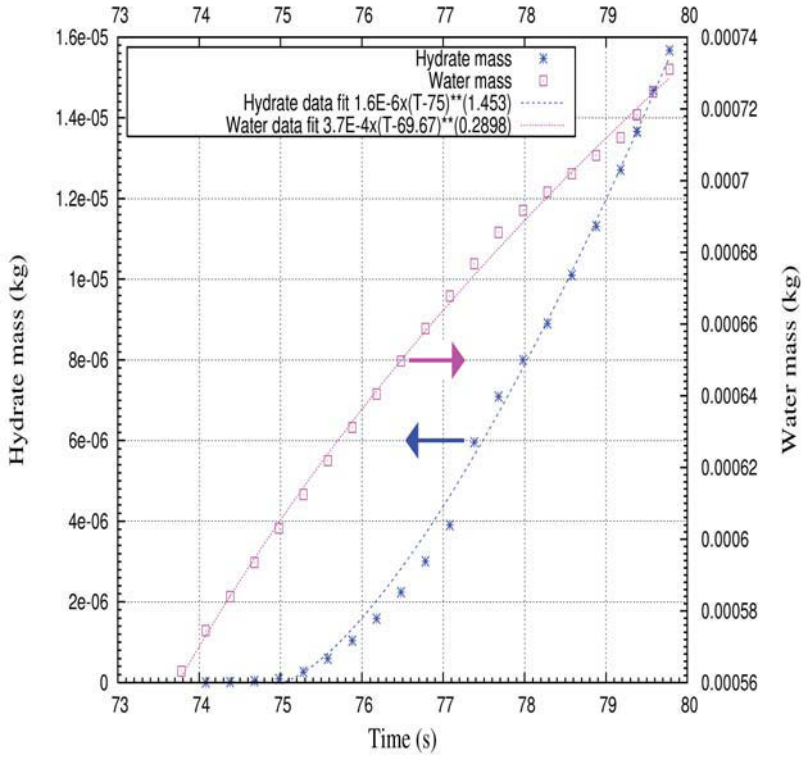

Figure 5.13: Temporal evolution of hydrate and water in pipe volume

The temporal evolution of total masses of water and hydrate in the pipe is shown in figure 5.13. The least square fit for the increase of water mass with time yields the equation;

$$M_w(t) = 3.7 \times 10^{-4}(\tau - 69.67)^{0.29} \tag{5.9}$$

A least square fit for the increase of hydrate mass with time yields to:

$$M_h(t) = 1.6 \times 10^{-6}(\tau - 75)^{1.453} \tag{5.10}$$

where τ is the time since the start of the calculation. It is observed that the hydrate follows a trend $\propto t^{1.453}$ where as the water obeys the trend $\propto t^{0.29}$ where t is the time elapsed since the hydrate nucleation begins. Kaschiev et al. [41] in development of their theory have captured analytically the details of initial hydrate crystallisation and identified the initial rate $\propto t^{1.5}$ for instantaneous nucleation. At later stage the hydrate formation rate is ever increasing (progressive nucleation), for example rates $\propto t^{2.5}$ have also been mentioned as the nucleation progresses forward in time [41]. It is clear that the hydrate formation trend observed is in good qualitative agreement with the instantaneous nucleation rate mentioned by Kaschiev et al.

It must be pointed out here that while Kaschiev et al. [41] have considered the hydrate kinetics in a static (from mechanics point of view) system, the system under consideration consists of moving fluids. The rate of increase of mass shown in the curves for the pipeline section is less than it would be in a static system (or a very long pipeline section) since the hydrate and water mass are being produced in the pipe section and also convected out from the outlet. It can be safely deduced that if the rate of increase of hydrate mass follows the same trend over time and is more than the rate of increase of water, it can result in conversion of all the water mass into hydrate. This is the case of instantaneous nucleation where, due to high rate of heterogeneous nucleation, all the nuclei form instantaneously.

The hydrate nucleation and growth is limited by presence of water [7], so it is natural for hydrate (formation and accumulation trend) to follow the trend followed by water to some extent.

Figure 5.14 shows the hydrate contours in the hydrate water slurry. It can be seen that the maximum hydrate concentration is in the bulk of the liquid accumulated at the base of the lowered section of the pipe. One striking thing to note is that hydrate formation is also considerable near 3'o clock (and 9'o clock) positions. It may be due to the fact that the temperature of the thinner water layers (due to downward flow) approach the wall temperature faster and thus results in more nucleation and growth. Eventually the hydrate nucleated at the walls during initial stages flow along with water to the bottom of the pipe. If the same scenario is considered at later times, when the solidification at the bottom has started, these nuclei flowing down may get stacked on already solidified mass. A hypothetical picture (figure 5.10) of the scenario has been presented by Sloan et al. [1]. As presence of water is the limiting factor in the

hydrate formation phenomenon, it is most likely that the maximum hydrate concentration is at the base of the pipe.

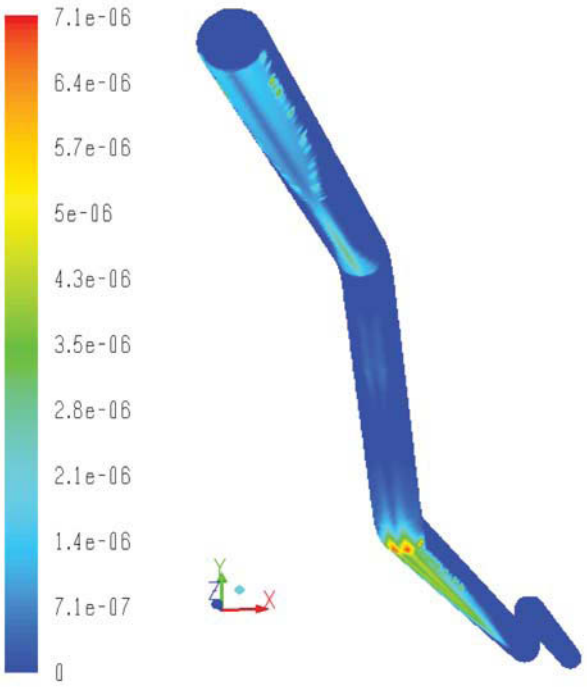

Figure 5.14: Hydrate volume fraction along the pipe wall

Figure 5.15 shows water and hydrate volume fractions along cross-sections along the lowered section of the pipe. The gradual effect of water accumulation can be seen in the sequential cross-sections. While the water tends to accumulate at the bottom , the hydrate shows a different picture. Higher hydrate concentrations at the walls circumferentially point towards higher formation rates near 3'clock (and 9'o clock) positions.

In the event of rapid nucleation (at an advanced stage of nucleation) where the nuclei agglomerate and crystallise rapidly, the hypothetical picture of hydrate crust formation would be a crust layer which is thicker climbing up circumferentially along the pipe walls. This conceptual picture of the hydrate blockage in 'arterio-stenosis' style has been discussed by Sloan et. al [1] (see figure 5.2).

The 'crusting' may continue until it completely covers the pipe wall cir-

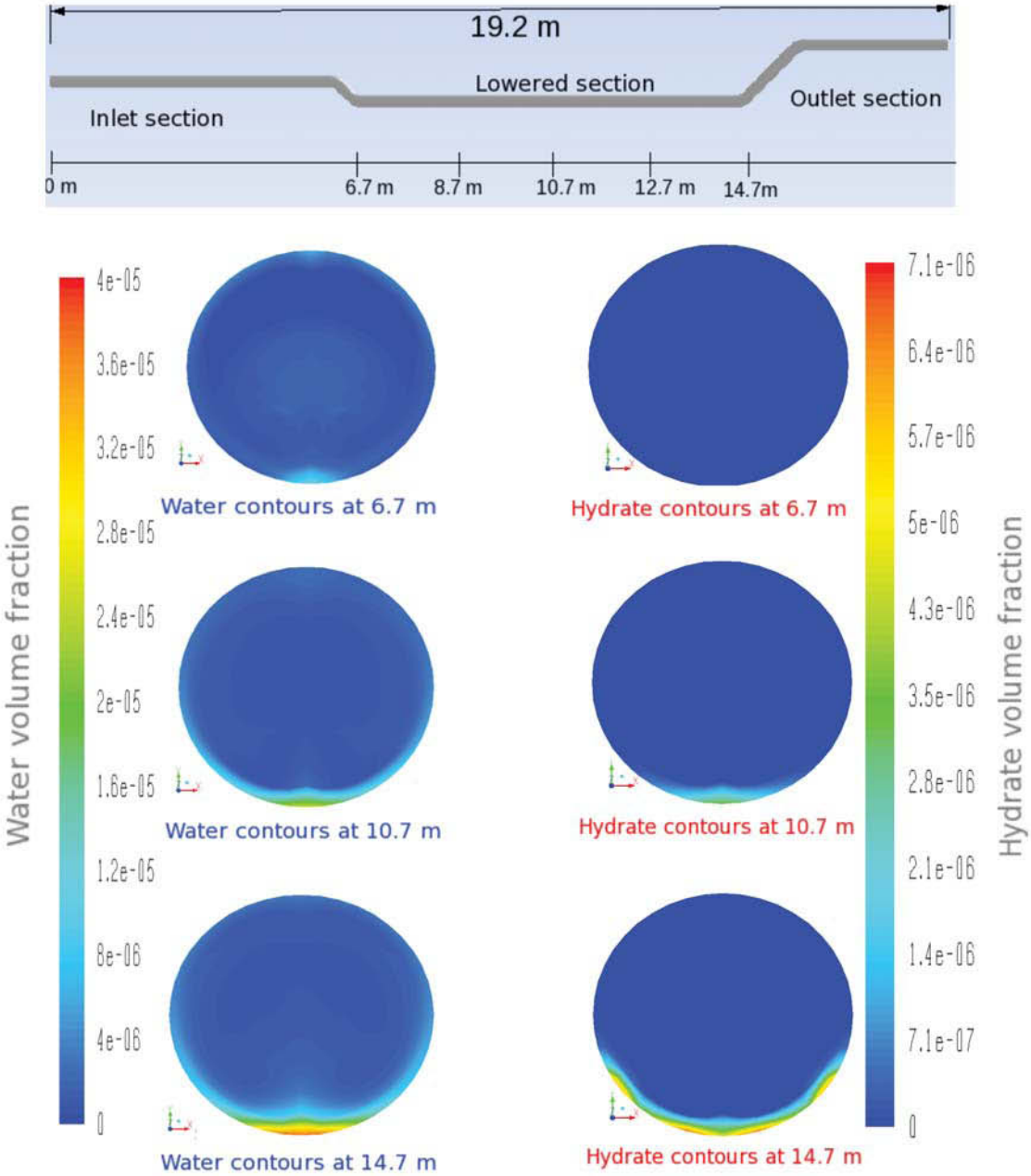

Figure 5.15: Left column from top to bottom showing water volume fraction at 6.7m, 10.7m and 14.7m and right column from top to bottom showing hydrate volume fraction at 6.7m, 10.7m and 14.7m

cumferentially. With increasing time the crust may get thicker reducing the effective pipe cross-section. In addition to circumferential deposition, the deposition may be along the length of the pipe line as well. In this regard Joseph et. al [17] in their work have divided the phenomenon in to three steps i.e. wall growth, wall sloughing and pipe plugging. According to the authors, the deposition in the gas pipelines begin with deposition at the walls, the deposits grow and make the cross-section area of the pipe narrow and then the deposit may sloughen blocking the pipe at bends etc.

In order to assess the variation of species along the bottom of the lowered section of the pipe, the following results in figure 5.16 are displayed along a line positioned at 6'o clock in axial direction.

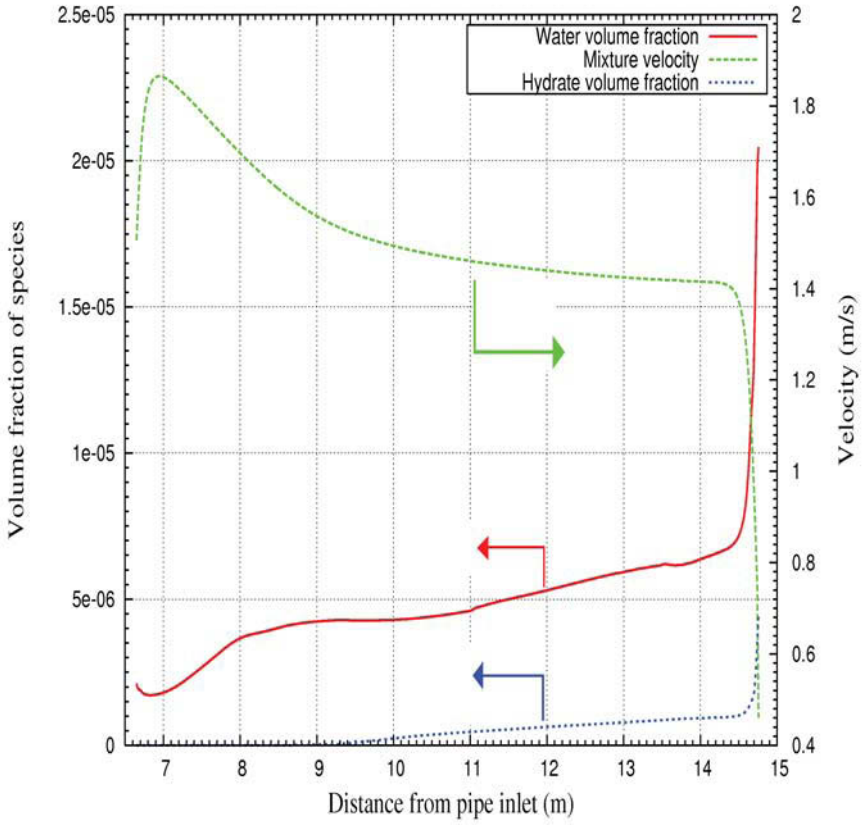

Figure 5.16: Water and hydrate volume fractions along bottom of the lowered section of the pipe

It is evident that at the point where the axial velocity drops significantly, the hydrate and water water concentrations start to increase. The hump in the velocity curve at about 7m is due to the impingement of down coming fluid on the wall, which is matched with the decrease in water volume fraction at about the same position. The hydrate volume fraction starts to increase at about 9m and shows stable gradual increase.

Temporal evolution of species can be seen in figure 5.17. The increase in the total water mass in the pipe with time is the result of condensation. It can be seen that the mass of water and hydrate increase with time and have the same trend. The trends of hydrocarbon gas and water vapour shows a very slight decreasing trend which shows their accumulation in the pipe.

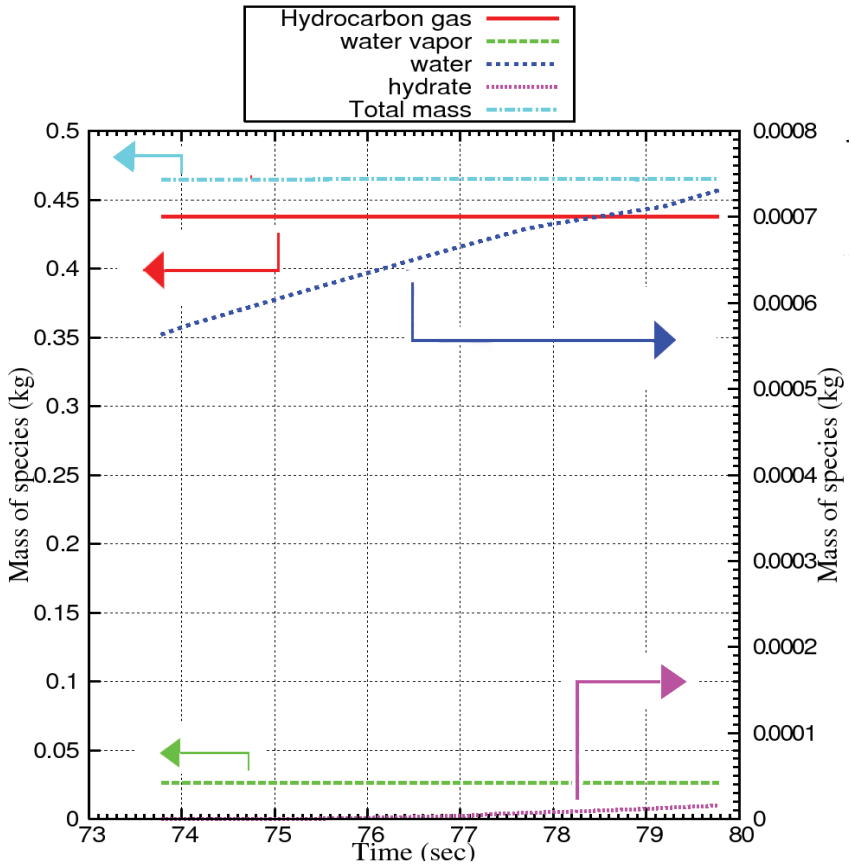

Figure 5.17: Temporal variation of species with time

5.6 Case of Three Pipeline Sections With Lowered Sections at Different Angles

5.6.1 Materials and Methods

For the sake of comparison, three pipeline sections were considered with an inlet section, a middle (lowered section) and an outlet section as depicted in table 5.2. The pipe consists of an inlet section of 15 m each, a middle section with pipe length 10 m each where the pipes have an inclination with the horizontal at different angles as shown in the figures in table 5.2, and an outlet section each with a length of 2.5 m. The aim of case of three pipes with

the setup is to see the effect of inclination on the rate of hydrate formation and accumulation etc.

Table 5.2: Pipelines with different angle of inclinations

No.	*Schematic*
a.	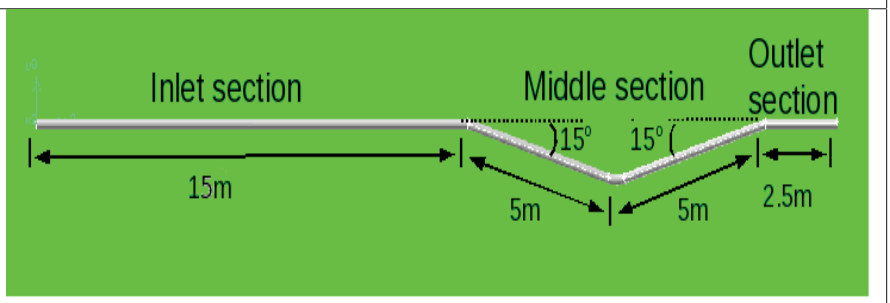
b.	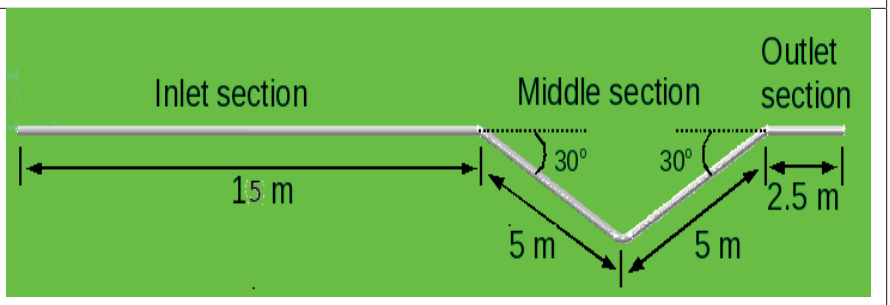
c.	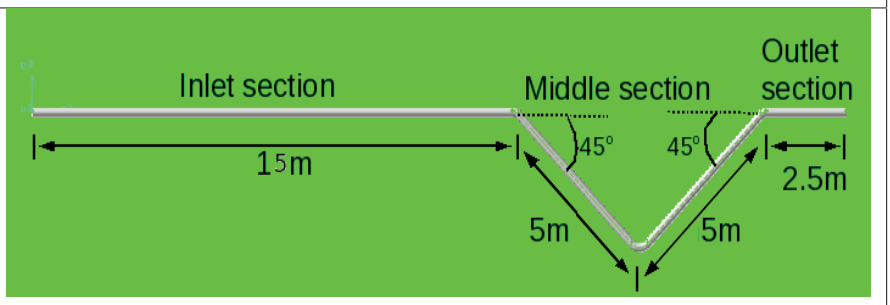

The various inputs and pipeline parameters for all the pipes are same as given in the table 5.1 except for the heat flux which is $-300W/m^2$.

5.6.2 Results and Discussion

Water and hydrate accumulate generally at the bottom of the pipe. The hydrate and hydrate-water slurry contours for all the pipe sections (i.e with $15^o, 30^o$ and 45^o inclinations) are shown in figures 5.18 and 5.19 respectively. The pipe section are shown from the bottom in order to see the contours of hydrate and hydrate-water slurry. Furthermore, the pipeline sections are scaled down in length in order for the contours to be more visible.

The rate of condensation is determined by the degree of supercooling below the saturation temperature of the bulk fluid as given by equation 5.1. When the

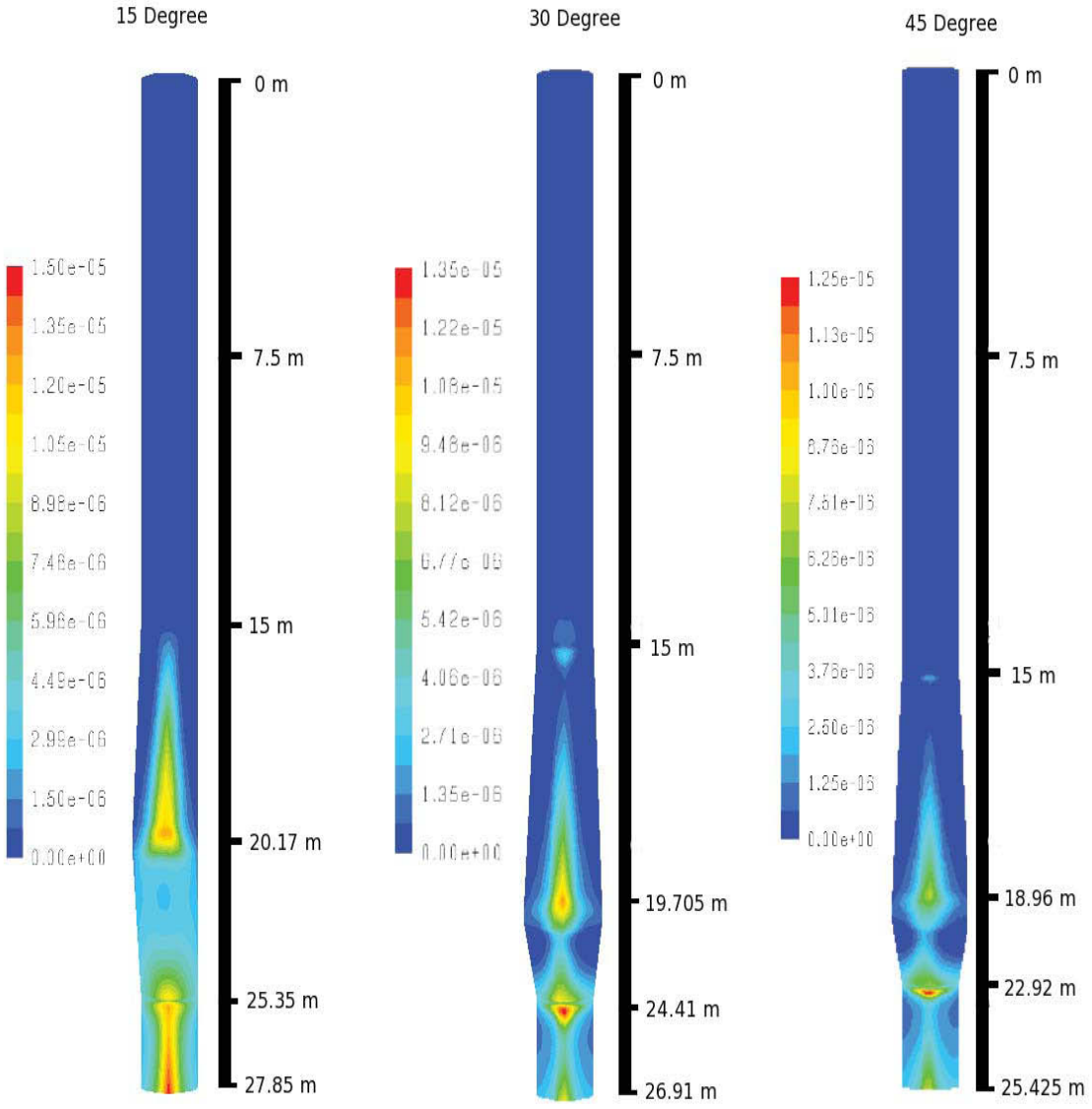

Figure 5.18: Hydrate contours in 15^o, 30^o, 45^o pipe

temperature falls below the saturation temperature corresponding to partial pressure of vapour, the vapour condenses to water. As discussed in previous sections, the condensed water tends to accumulate at the bottom (6'o clock position) of the pipe, primarily at low points in the pipe.

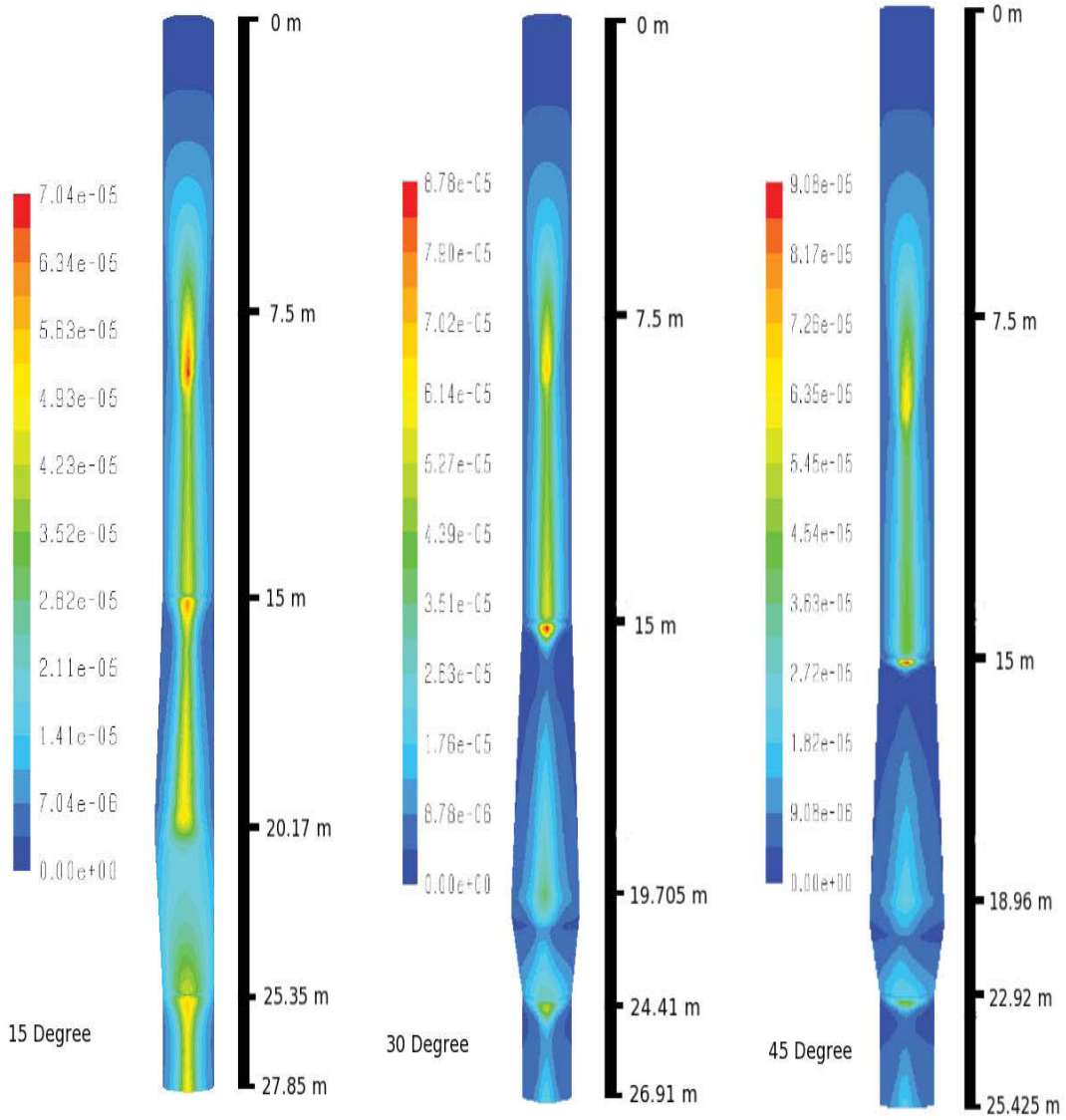

Figure 5.19: Hydrate-water slurry contours in 15^o, 30^o, 45^o pipe

As the hydrate form in the water film along the pipe walls, the water and hydrate generally show up at the bottom of the pipe. In all the pipe sections, one striking thing to be noted is that while the distribution of water contours is all along the pipe bottom, hydrate contours show at the low point of the middle section and beyond (i.e outlet section). This is due to the temperature

drop along the length of the pipe sections, as the fluid at the pipe wall attains the hydrate equilibrium temperature farther away from the position in the pipe where the fluid temperature drops below the dew point, and also due to the fact that the more the temperature drops below the threshold temperature , more is the driving force for nucleation and consequently the rate of hydrate formation (see equation 5.4 and 5.7) . As the gas stream travels forward along the pipe, the bulk fluid temperature drops further. For this reason, at increasing distance from the inlet of the pipe (starting from the position the fluid reaches hydrate equilibrium temperature), the driving force for the hydrate formation increases resulting in an increase in the hydrate formation rate. A graph of wall film temperature is given in figure 5.20.

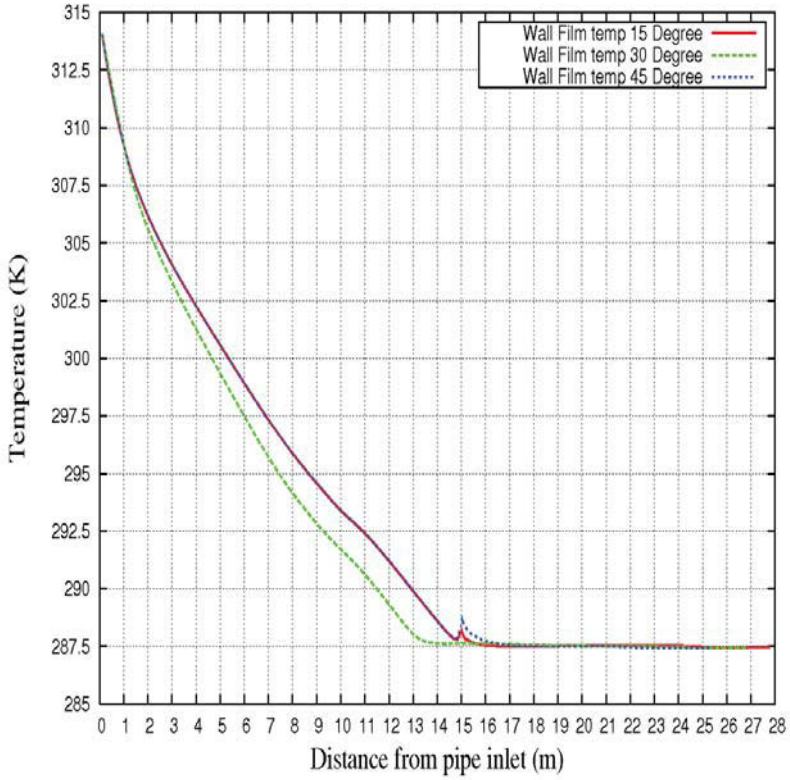

Figure 5.20: Wall film temperatures along length of the pipe

As seen from the figure, there is a steep drop in temperature of the fluid at walls till the fluid attains nearly wall temperature. Figure 5.21 shows the bulk temperatures for the pipe sections which follow the same trend and approach the wall temperature along the length of the pipe. Before the first bend i.e about 15m from the pipe inlet for all the pipes, the bulk temperature drop is about the same, while after about 15 m, the drop in bulk temperature for

45^o is more than that of the other pipes. The reason for this is, more effective mixing in pipes with steeper bends.

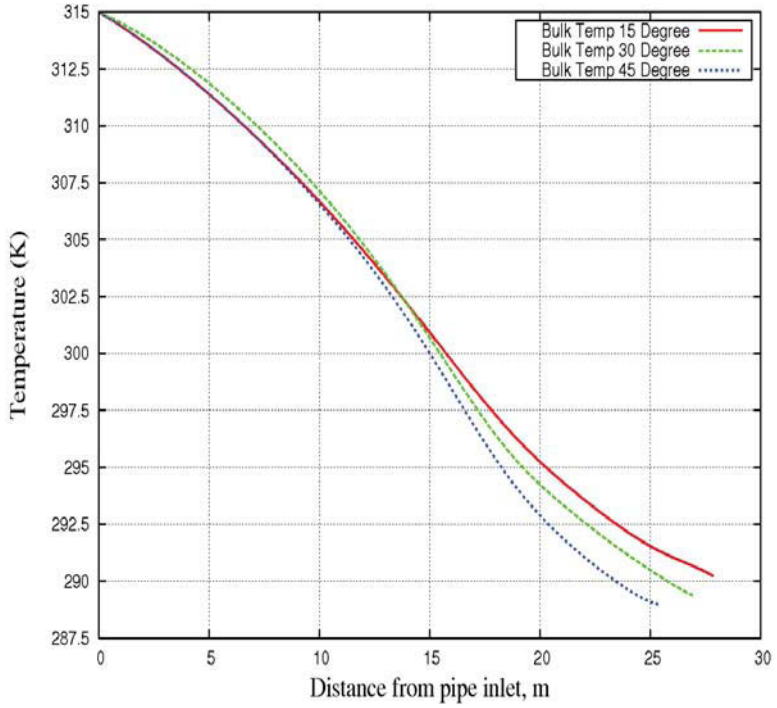

Figure 5.21: Change of bulk temperature along the length for 15^o, 30^o and 45^o pipes

Figures 5.23-25 show combined centerline and wall film temperature along the length of the pipe. All the figures show that the bulk temperature approaches the wall temperature along the length of the pipelines.

Figure 5.19 shows that the hydrate-water slurry is generally concentrated at the bends. Comparing figures 5.19 and 5.22 shows that the slope of the velocities for 15 degree, 30 degree and 45 degree pipes sections and intermittent high concentration of the slurry are correlated or have a common cause as when the slope of the velocity is increasing, so is the concentration of the accumulated hydrate water slurry.

It was expected that at the lowest point of the middle section, the accumulation of the hydrate-water would be high due to gravity, but at such low concentration of condensed fluid, the drag of the bulk phase is high enough to push the fluid at the low points further down stream. Furthermore, in pipe with steeper inclinations, the rate of change of velocity (at the fluctuation sites) sites is higher than for less steep inclination pipes. A comparison of the mass flux of hydrate and water at outlet of all the pipes (when they have approached steady state) show that the more hydrate water slurry is being pushed out from the steeper inclination pipes. The results are depicted in table 5.3:

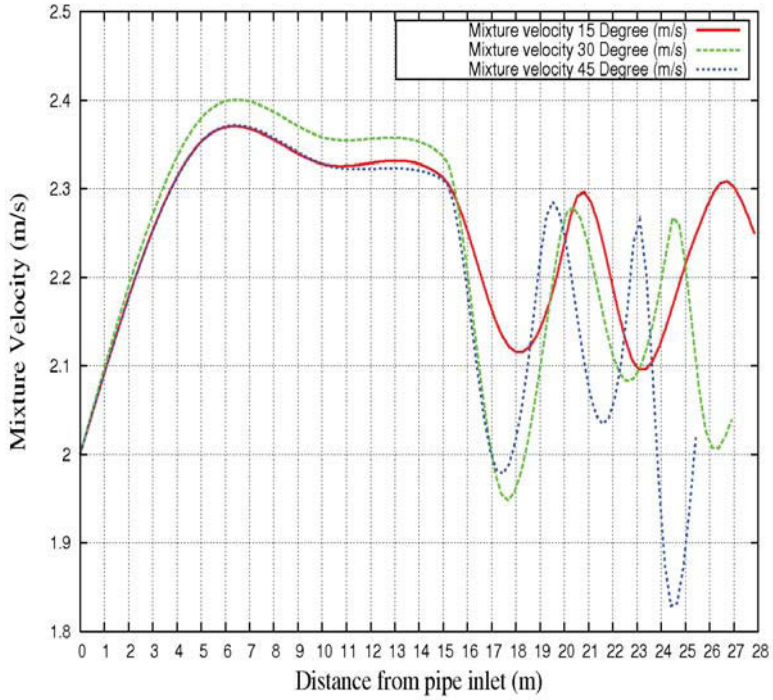

Figure 5.22: Velocity variation along pipe (15^o, 30^o and 45^o) centerline

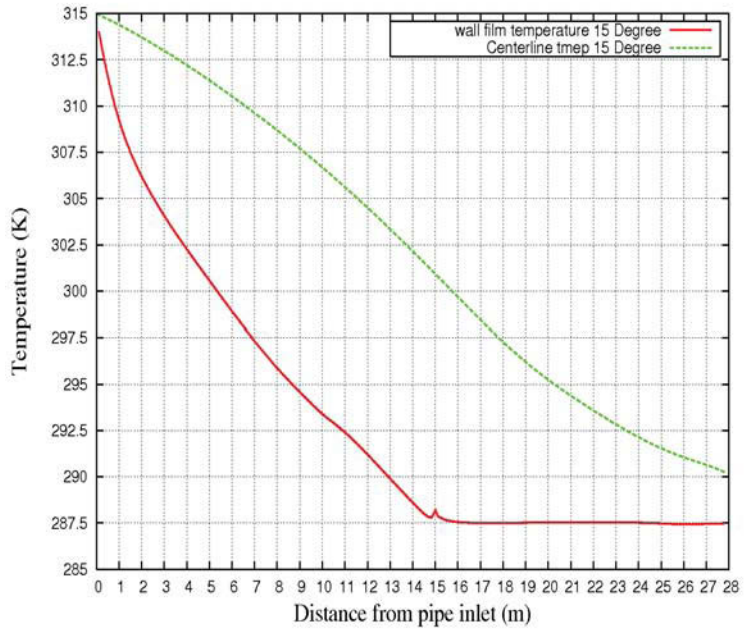

Figure 5.23: Centerline and wall film temperature variation for 15^o pipe

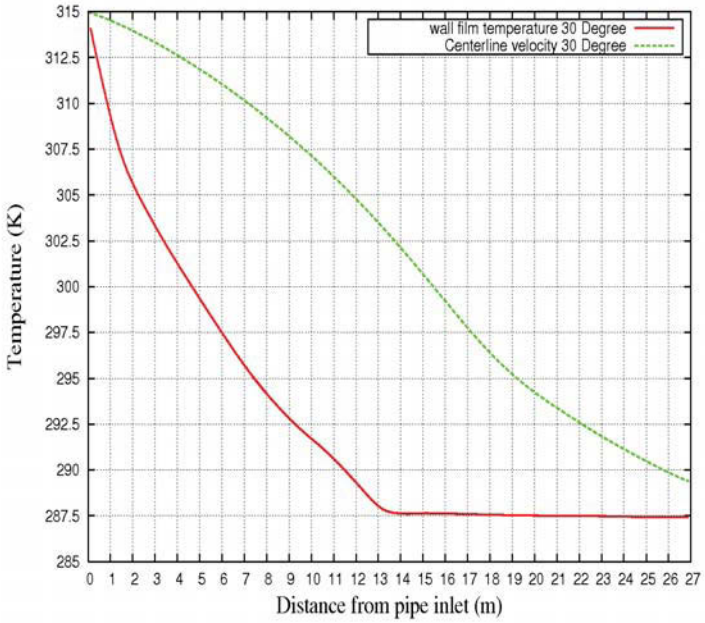

Figure 5.24: Centerline and wall film temperature variation for 30^o pipe

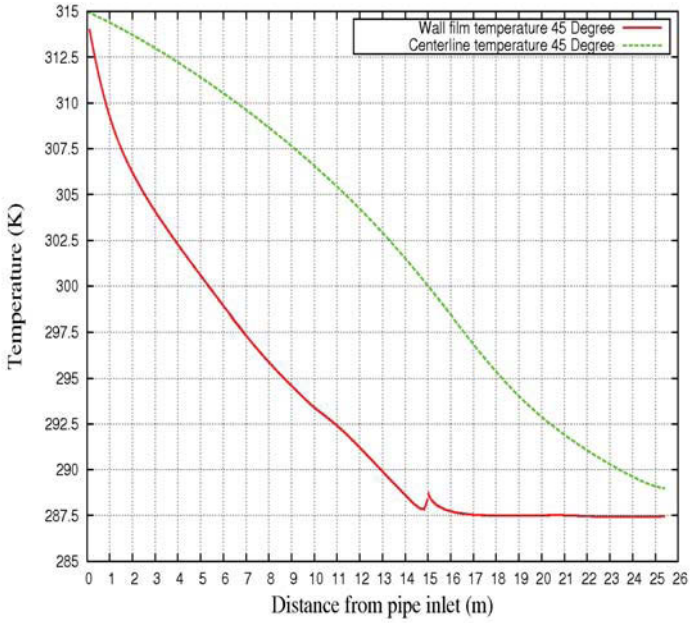

Figure 5.25: Centerline and wall film temperature variation for 45^o pipe

Table 5.3: Mass flux of species.

$Pipe$	$Hydratekg/s$	$Waterkg/s$	$Totalkg/s$
15^o	5.25E-5	2.008E-4	2.5346E-4
30^o	5.23E-5	2.016E-4	2.5389E-4
45^o	5.15E-5	2.026E-4	2.5460E-4

The table clearly shows that the as more water mass is being flushed out from the higher inclination pipes, the hydrate production rate may decrease, as water is the precursor for hydrate formation.

For the cases of all the pipe sections $15^o, 30^o$ and 45^o, the condensation starts at the inlet section as the temperature falls below the saturation point, while the hydrate is non-existent. The hydrate formation starts at the middle section and continues beyond it. This shows an important result that the presence of water at a section does not automatically guarantees the presence of hydrate as the hydrate start to form only when the temperature is sufficiently below the hydrate equilibrium temperature so that stable hydrate nuclei start forming.

Figure 5.26 and 5.27 shows the hydrate and water mass in pipe with time. The hydrate mass increase in pipeline with time shows sigmoidal trend for all the pipes. As the negative heat flux applied is very high, the fluid temperature drops below hydrate equilibrium temperature very quickly and hydrate formation starts almost instantaneously. The initial hydrate formation rate is very high and hydrate mass keeps on increasing, until a plateau is reached after which the hydrate increase in pipe just ceases to increase. Figures 5.26 and 5.27 just show the steady state region of the hydrate and water respectively in pipe.

The initial increase is due to the initial nucleation rate (incipience of critical nuclei), which grows according to the rate (t^m) where t is the time elapsed after the incipience of hydrate formation and $m > 1$ is a number as discussed in section 5.4.

However, the increase is not permanent and starts to diminish when the limiting factors start to appear. The limiting factors in our case involve, a decrease in water volume fraction, (due to conversion in to hydrates). The water increase may also be limited due to vapour depletion in pipe along the length which results in decrease in condensation rate. The rate of condensation may also be limited due to a decrease in direct impingement of water vapour on the walls due to presence of water film along the wall.

Another limiting factor for hydrate increase in pipe is the convection of hydrate formed out of pipeline section under consideration. The effect is evident at about 18 seconds after which the increase is slowed down.

Figure 5.27 shows water mass in pipe with time and for all the time pipeline

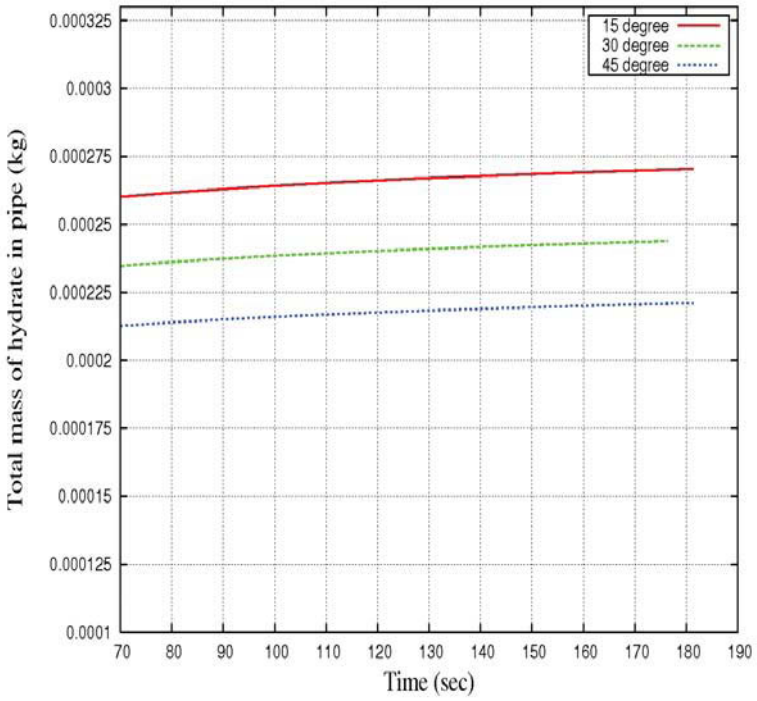

Figure 5.26: Change in Hydrate mass in pipeline section

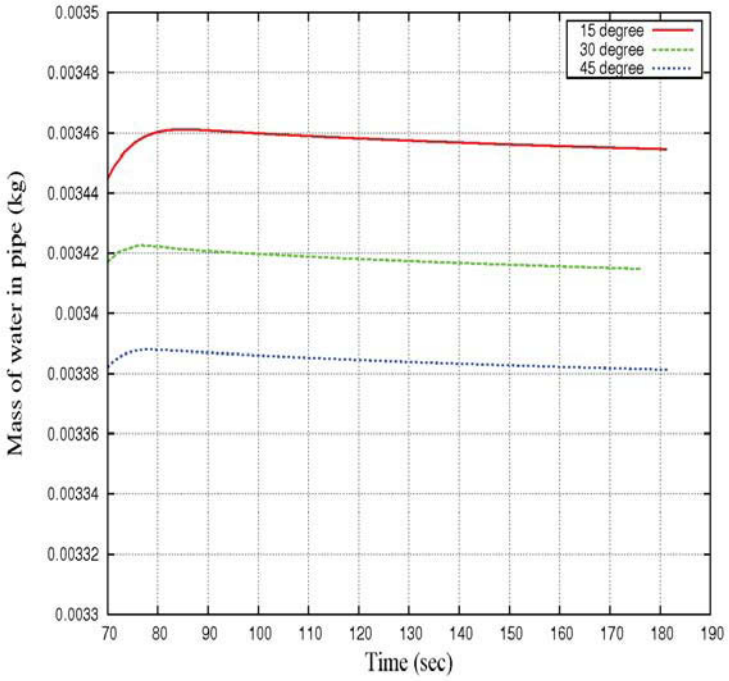

Figure 5.27: Change in water mass in pipeline section

sections show similar trend, with an initial rise, which starts to decline and finally reaches a plateau. Among the limiting factors for increase of water mass all the depletion of water vapour, inhibiting effect of water film which decreases the direct impingement of vapours on cold pipe wall and convection of water out from the pipeline section.

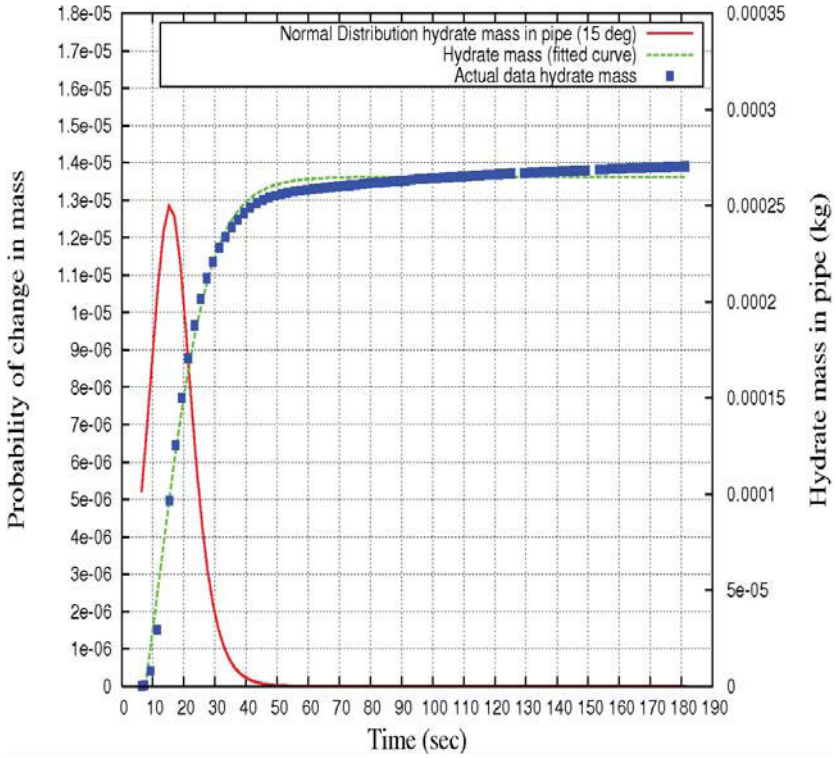

Figure 5.28: Fitted hydrate mass increase with time (15 degree)

Figures 5.28- 5.30 shows the graph with the data for increase in hydrate mass in pipe with time and the fitted curve for data. The fitted curve shows that the behaviour follows typical sigmoidal trend with the expression of the form:

$$m(t) = A + \frac{B - A}{1 + (exp(-Ct) + D)} \tag{5.11}$$

Where A, B, C and D are fitting constants with each one having a specific meaning.

This behaviour (of sigmoidal trend) is observable in many natural and industrial processes specially regarding population (birth, death and growth of species etc.). Differentiating the expression for sigmoidal gives us the normal distribution curve. The differential function corresponding to each fitted curve is plotted in figures (3.28-3.30).

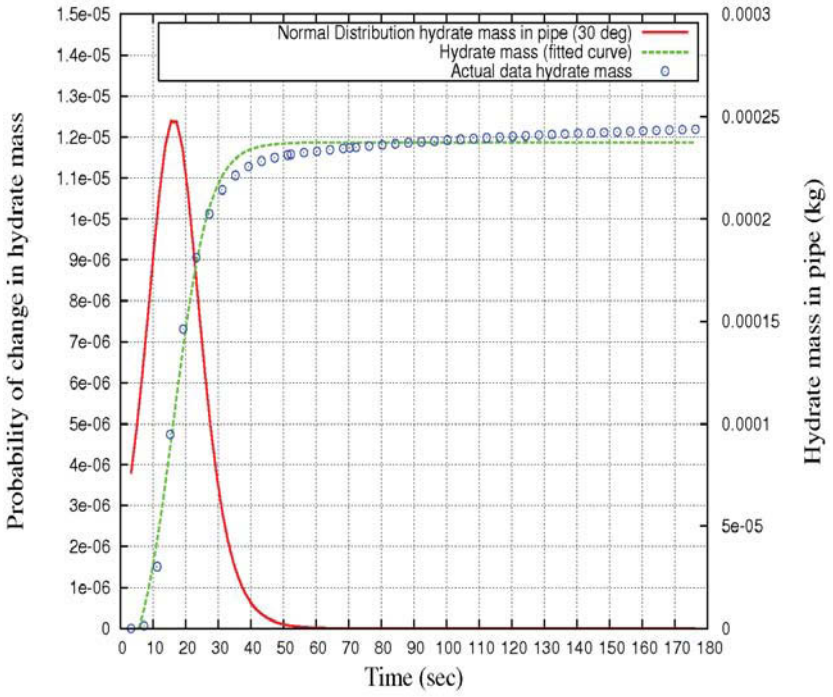

Figure 5.29: Fitted hydrate mass increase with time (30 degree)

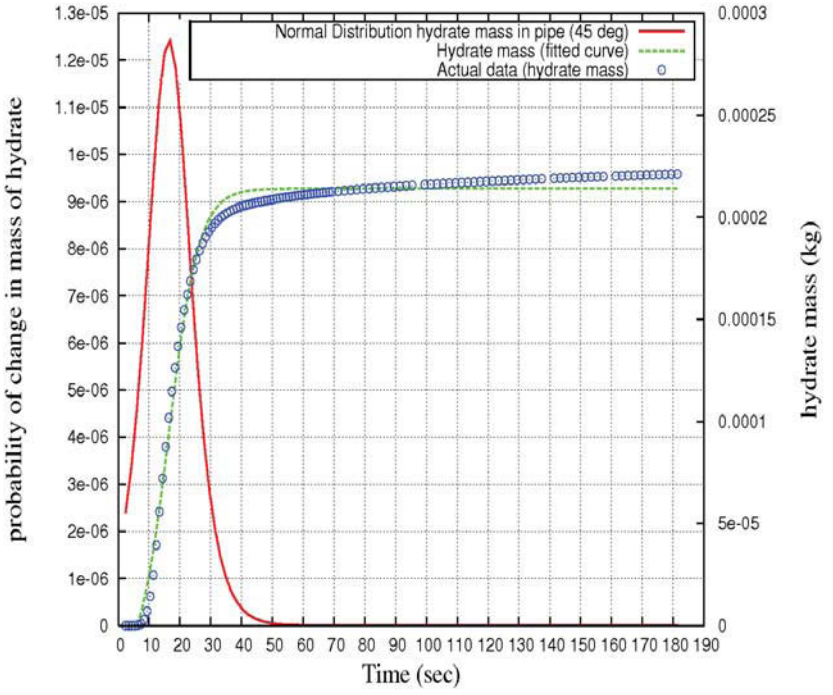

Figure 5.30: Fitted hydrate mass increase with time (45 degree)

The initial rising branch of the normal distribution curve shows the rate of increase of hydrate in pipe with the point of inflection showing a decline in the rate of increase. The descending branch of the curve is indication of the mass of hydrate approaching a plateau or steady state condition . The 15^o , 30^o and 45^o reach steady state at about the same time i.e. about 40 sec but differ in the height of inflection point. The height of inflection point of 15^o pipe is highest and of 45^o pipe is lowest.

The areas under the curve of the normal distribution curve for a period of time gives the hydrate mass formed in the pipe for that particular time.

The results for small pipeline sections as considered can be generalized for very long pipe and can be helpful in predicting the behaviour in long pipelines. For a very long pipe line, if we integrate the mass of hydrate in pipe over time, it is expected to show the same (sigmoidal)trend, due to the factors giving rise to exponential increase, and at the same time, appearance of the limiting factors resulting in total mass of hydrate in pipe approaching an asymptotic value. However independently, for each segment of pipeline, the situation may not be uniform, as, discussed in section 5.4, the water vapour depletes from the bulk gas stream due to condensation resulting in drop in the partial pressure of the vapour. If the temperature profile along the pipe is such that the temperature at pipe wall is not below the saturation temperature corresponding to the (new, dropped) partial pressure, condensation of vapour to water will cease. While the water already condensed in the previous pipe section along with the hydrates may flow in to this new section, new hydrate formation will be limited due to decrease in condensation.

In this way, the gas will travel along the pipe, and if it gets cooled down continuously (assuming an infinite cold reservoir surrounding the pipe), at some point and time, the condensation (and hydrate formation) may start again if the temperature gets below the dew point. In this way, there may be very long, wet, hydrate prone regions of the pipe, followed by dry regions which again is followed by wet regions.

The scenario presented above has much more dimensions to it, such a overall system pressure drop, which may cause shift (again) in dew point and hydrate equilibrium temperature (corresponding to the new pressure), slip between phases which may cause vapour or hydrocarbon gases concentration to vary along the pipe etc. Moreover the assumption here has been that the temperature consistently along the pipe, however, there may be a case so that the pipe passes through geographical formations with varying heat capacities, thermal properties, and the temperature may fluctuate so that hydrate formed previously dissociates, or condensed water vaporises again.

The results indicate that the lowered sections with greater angles of inclination may not result in higher rate of hydrate or water accumulation at such low rates of water (and hydrate) concentrations, as the dynamic pressure fluctuations causes the hydrate-water slurry to be flushed downstream.

Chapter 6

Summary Outlook and Conclusions

6.1 Summary

A brief summary of the literature that has been surveyed and the model capabilities that has been developed is given below:

- Hydrates are an important area of research for the oil and gas industry due to their prospects of being a huge energy resource. Study of hydrates is also necessary in order to avoid pipeline blockages, leading to revenue losses and possible damage to equipment and personnel.
- Hydrates are present in large quantities in the earths crust and in permafrost region, but thermodynamic and kinetic behaviour of hydrates must be determined to minimize the probability of accidents and damage to the environment.
- In gas pipelines, hydrate formation is detrimental to the flow assurance by blocking pipelines, and may even cause accidents. So it is necessary to avoid hydrate formation in the first place (by thermodynamic inhibitors etc), or if hydrate avoidance is not cost effective, then to manage hydrate with help of kinetic inhibitors.
- There is a lot of literature containing charts, tables, nomographs available through the work of researchers, that can be used to assess the thermodynamic conditions for hydrate formation for user specific purposes.
- There are new software tools available, based on rigorous statistical thermodynamics to calculate hydrate formation conditions that can be used for hydrate formation conditions ascertation with different compositions.

- Ascertation of relevant hydrate properties and behaviour is of utmost importance in order to exploit them to reap the benefits, or to avoid the risk and potential losses.
- Hydrates though similar to ice , when formed have a complex formation mechanism. Hydrates formation can be delayed and the system can remain in metastable state even if the pressure, temperature conditions are conducive. Hydrates require a certain minimum driving force for their formation. The hydrate dissociation process on the other hand starts once the conditions cross the hydrate equilibrium conditions.
- The system considered for the case studies consists of gas pipeline with moisture, which condenses and hydrate forms in the condensed water. The condensed water is also gas saturated. Thermodynamical assessment gives the driving force as the degree of subcooling. Furthermore, the heterogeneous mode of hydrate formation is considered due to proximity to the pipeline wall.
- The hydrate formation phenomenon can be modeled with CFD by employing a set of conservation equations of mass, momentum and energy, and incorporating the rate of hydrate formation expressions in the phase continuity equations.
- The nucleation rate expression developed is based on the particular scenario, and takes in to account the physics of hydrate attachment and detachment mechanisms and the probability of the attachment events based on the driving force and activation barrier. It ascertains the rate of formation of critical sized nuclei.
- The rate of growth expression takes in to account the growth of the critical nucleus by the mechanism of attachment and links the rate of growth with time elapsed since the birth of nuclei. It incorporates the nucleation rate expression as well, giving the total rate of increase of hydrate.
- The expression of rate of growth gives the hydrate formation rate in moles, which is converted to kg with the help of formula of for the building block of a single hydrate building unit.
- All the additional equations for the rate of condensation, driving force for hydrate formation, rate of hydrate formation expression can be incorporated in to the main Fluent code with the help of user defined functions.
- In this way a bridge between the hydrate formation mechanisms at molecular level and macro state variables ascertained through CFD computations can be made to determine the hydrate formation rates in gas pipelines.

6.2 Conclusions

The hydrate formation model is applied to the case of arbitrary pipeline section, and a case of three pipelines with different inclinations in order to have an insight to the three dimensional hydrate formation mechanism. Some key results have emerged from the study:

- Hydrate formation in gas pipelines requires presence of free water, so a system with a gas having some moisture content is prone to hydrate formation. However, the condensation temperature and hydrate formation temperature at a certain pressure in the pipe line may differ, so even though there may be condensed water present at a certain pipeline section , it is not necessary that hydrate formation starts there. However, the condensed water when it travels downstream at the position where the conditions are met, then hydrate formation may begin.

- The condensation results in a decrease of the volume fraction of vapour in the gas, which results in a drop in partial pressure of the vapour, so even though if condensation may start at some point in a pipe line, after a certain point downstream , the condensation may cease owing to the fact that the saturation temperature required for condensation is much lower than the prevalent temperature.

- At a position in the pipe line, where sufficient water is present, and the thermodynamic conditions favour hydrate formation, hydrate nucleation may start based on the strength of the driving force. Nucleation may start at a place, but it may not show as a deposit due to low volume fraction, and furthermore, the nucleated hydrate may travel downstream with the main flow.

- Water generally accumulates at low points/ base of the rising sections in the pipe lines, so, the probability of hydrate formation/ initiation is maximum at those places. However, as discussed above, if the driving force here is not high enough for instant crystallization, the hydrates initiated at these places may travel downstream.

- In case of inclined pipes with valley sections at these initial stages of increase of hydrate nuclei population, there is no significant difference in the water and hydrate accumulation in 15^o, 30^o and 45^o pipe sections. It was expected that the accumulation would be more in 45^o pipeline sections , however, it was revealed that whereas the heat transfer may be more effective, the water is flushed out more effectively in the 45^o pipe.

- There is no significant advantage of more inclination at the walls as the wall temperatures for all the pipes follow the same trend (almost the

same values) but the bulk temperature in a pipe with greater inclination angle will follow greater temperature drop due to more effective mixing.

- The increase of hydrate mass in a pipeline section follows a sigmoidal trend, with a dramatic initial rate of increase and thereafter a decrease in the rate, until the system reaches steady state. The system reaches steady state once the factors causing the increase and the limiting factors balance each other out.

6.3 Future Directions and Recommendations

The work performed opens the door to take a brief look into the initial phase of hydrate formation mechanism. However, three dimensional computations, for realistic pipeline sections are still not feasible due to hardware limitations (CPU speed and memory). In order to exactly pin point the hydrate deposition the following recommendations are advised:

- It is proposed that for a complete analysis of complete pipelines, a hybrid approach to hydrate formation be adopted, which uses the strengths of both one-dimensional calculations (where we are just passing pressure, temperature information downstream) and three-dimensional CFD methods.

- In order to address the deposition of hydrates in pipes, advanced crystallization theory addressing the deposition mechanisms in detail may be adopted to ascertain the morphology of deposits at the pipe walls.

- The hydrate dissociation should also be taken in to account while dealing with actual pipelines, since once hydrates are formed, they may dissociate along their way if the pipe section passes through warmer formations.

For a complete model applicable to simulate the prevailing conditions along the complete pipeline with respect to hydrate formation at any time and to give the operator of the pipeline system the possibility and chance to react, some additional influences have to be taken into consideration :

- Change of reservoir fluid composition and properties (of short duration because of reservoir and/or well behaviour and with production time or cumulative production respectively)

- Short term changes of production rate because of operational needs.

- Accelerated accumulation of liquids because of malfunction of separator or vice versa an evacuation of the pipe by pigging.

- Potential influences of pipe insulation (model could also be used as a tool for investment decisions).

- Influence of changing separator efficiency and other fluid treatment (e.g. methanol injection, heating).

As a vision, all above included in a real time model could lead to a fully automated and controlled "**hydrate free**" system.

Appendix A

Caculation of Compressibity factor

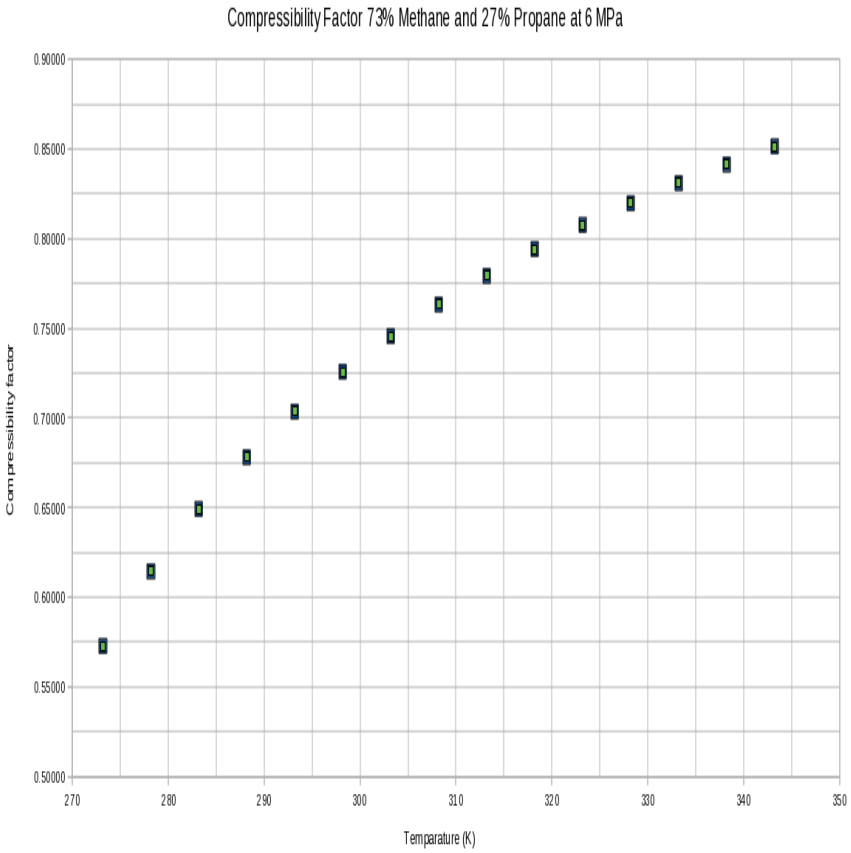

Figure A.1: change of phase from old (liquid) to new phase (solid)

Bibliography

[1] Dendy Sloan, A.K.S., Carolyn Koh, *Natural Gas Hydrates in Flow Assurance*. Gulf Professional Publisher, 2011.

[2] NTNU, http://www.chem.ntnu.no/nonequilibrium-thermodynamics/.

[3] CO2CRC, http://www.co2crc.com.au/.

[4] USGS, http://marine.usgs.gov/fact-sheets/gas-hydrates/title.html.

[5] GZG, http://peggy.uni-mki.gwdg.de/.

[6] UB, http://www.marum.de/en/.

[7] E. Dendy Sloan, K.A.K., *Clathrate Hydrates of Natural Gases*, 2008.

[8] Kashchiev, D., *Nucleation:BASIC THEORY WITH APPLICATIONS*. Bitterworth-Heinemann, 2000.

[9] http://en.wikipedia.org/wiki/nucleation.

[10] Markov, I.V., *Crystal Growth for Beginners*. World Scientific, 2004.

[11] H K Versteeg, W.M., *An Introduction to Computational Fluid Dynamics*. Pearson Education, Ltd., 2007.

[12] *Comet User Manual (n. d.), ICCM Institute of Computational Continuum Mechanics GmbH, Hamburg, Germany, available at: www.iccm.de.*

[13] Makogon, Y.F., *Hydrates of Hydrocarbons*. PennWell Books, 1997.

[14] W.M. Deaton, J., E.M. Frost, Gas hydrates and their relation to the operation of natural-gas pipe lines. Technical report, United States Department of the Interior, Bureau of Mines, July 1946.

[15] P.Raj Bishoni, V.N., Formation and decomposition of gas hydrates. *Fluid Phase Equilibria*, **117**, pp. 168–177, 1996.

[16] Jr., C.P.R. & Lage, P.L., Modelling of hydrate formation kinetics: State-of-the-art and future directions. *Chemical Engineering Science*, **63(8)**, pp. 2007 – 2034, 2008.

[17] Joseph W. Nicholas, J.P.C.A.K., Ryan R. Inman & Sloan, E.D., A modelling approach to hydrate wall growth and sloughing in a water saturated gas pipeline. *Proceedings of the 6th International Conference on Gas Hydrates (ICGH 2008)*, 2008.

[18] Jassim, E., Abdi, M.A. & Muzychka, Y., A new approach to investigate hydrate deposition in gas-dominated flowlines. *Journal of Natural Gas Science and Engineering*, **2(4)**, pp. 163 – 177, 2010.

[19] B.V. Balakin, P., A.C. Hoffmann, Experimental study and computational fluid dynamics modeling of deposition of hydrate particles in a pipeline with turbulent water flow. *Chemical Engineering Science*, 22 November 2010.

[20] Ahmadi, G., Ji, C. & Smith, D.H., Numerical solution for natural gas production from methane hydrate dissociation. *Journal of Petroleum Science and Engineering*, **41(4)**, pp. 269 – 285, 2004.

[21] Gong, J., Shi, B. & Zhao, J., Natural gas hydrate shell model in gas-slurry pipeline flow. *Journal of Natural Gas Chemistry*, **19(3)**, pp. 261 – 266, 2010.

[22] John Boxall, J.N.C.K., Simon Davies & Sloan, E.D., Hydrate blockage potential in an oil-dominated system studied using a four inch flow loop. *Proceedings of the 6th International Conference on Gas Hydrates (ICGH 2008)*, 2008.

[23] UT, http://www.tuhfp.utulsa.edu/.

[24] Davies, S.R., Boxall, J.A., Dieker, L.E., Sum, A.K., Koh, C.A., Sloan, E.D., Creek, J.L. & Xu, Z.G., Predicting hydrate plug formation in oil-dominated flowlines. *Journal of Petroleum Science and Engineering*, **72(3-4)**, pp. 302 – 309, 2010.

[25] Javanmardi, J., Nasrifar, K., Najibi, S. & Moshfeghian, M., Economic evaluation of natural gas hydrate as an alternative for natural gas transportation. *Applied Thermal Engineering*, **25(1112)**, pp. 1708 – 1723, 2005.

[26] Hao, W., Wang, J., Fan, S. & Hao, W., Evaluation and analysis method for natural gas hydrate storage and transportation processes. *Energy Conversion and Management*, **49(10)**, pp. 2546 – 2553, 2008.

[27] Zhang, J., Yedlapalli, P. & Lee, J.W., Thermodynamic analysis of hydrate-based pre-combustion capture of. *Chemical Engineering Science*, **64**, pp. 4732 – 4736, 2009.

[28] Tajima, H., Yamasaki, A. & Kiyono, F., Energy consumption estimation for greenhouse gas separation processes by clathrate hydrate formation. *Energy*, **29(11)**, pp. 1713 – 1729, 2004.

[29] Rouher, O.S. & Barduhn, A.J., Hydrates of iso- and normal butane and their mixtures. *Desalination*, **6(1)**, pp. 57 – 73, 1969.

[30] Hirai, S., Okazaki, K., Tabe, Y. & Kawamura, K., Co2 clathrate-hydrate formation and its mechanism by molecular dynamics simulation. *Energy Conversion and Management*, **38, Supplement**, pp. S301 – S306, 1997.

[31] Kashchiev, D. & Firoozabadi, A., Nucleation of gas hydrates. *Journal of Crystal Growth*, **243(3-4)**, pp. 476 – 489, 2002.

[32] Lederhos, J., Long, J., Sum, A., Christiansen, R. & Jr, E.S., Effective kinetic inhibitors for natural gas hydrates. *Chemical Engineering Science*, **51(8)**, pp. 1221 – 1229, 1996.

[33] Sloan, E. & Fleyfel, F., Hydrate dissociation enthalpy and guest size. *Fluid Phase Equilibria*, **76(0)**, pp. 123 – 140, 1992.

[34] Radhakrishnan, R., Demurov, A., Herzog, H. & Trout, B.L., A consistent and verifiable macroscopic model for the dissolution of liquid co2 in water under hydrate forming conditions. *Energy Conversion and Management*, **44(5)**, pp. 771 – 780, 2003.

[35] Kvamme, B. & Frrisdahl, O.K., Polar guest-molecules in natural gas hydrates. effects of polarity and guest-guest-interactions on the langmuir-constants. *Fluid Phase Equilibria*, **83(0)**, pp. 427 – 435, 1993.

[36] Carroll, J.J., *Natural Gas Hydrate: A Guide for Engineers*. Elsevier Science, 2003.

[37] Barrer, R. & Bratt, G., Non-stoichiometric hydratesi: Sorption equilibria and kinetics of water loss for ion-exchanged near-faujasites. *Journal of Physics and Chemistry of Solids*, **12(2)**, pp. 130 – 145, 1960.

[38] Schmelzer, J.W.P., (ed.) *Nucleation Theory and Applications*. WILEY-VCH Verlag GmbH & Co.KGaA, 2005.

[39] Firoozabadi, A., *Thermodynamics of Hyrocarbon Reservoirs*. McGrawHill, 1999.

[40] Beggs, H.D., *Gas Production Operations*. OGCI Publications, 1984.

[41] Kashchiev, D. & Firoozabadi, A., Induction time in crystallization of gas hydrates. *Journal of Crystal Growth*, **250(3-4)**, pp. 499 – 515, 2003.

[42] *Fluent 6.3 Users Guide*.

[43] UBC, https://circle.ubc.ca/bitstream/handle/2429/1133/5434.pdf.

[44] P.B. Patil, U.P.V., *Numerical Computational Methods*. Narosa publishers, 2006.

[45] Fu, P. & Farzaneh, M., A cfd approach for modeling the rime-ice accretion process on a horizontal-axis wind turbine. *Journal of Wind Engineering and Industrial Aerodynamics*, **98(45)**, pp. 181 – 188, 2010.

[46] Myers, T. & Hammond, D., Ice and water film growth from incoming supercooled droplets. *International Journal of Heat and Mass Transfer*, **42(12)**, pp. 2233 – 2242, 1999.

[47] Myers, T. & Charpin, J., A mathematical model for atmospheric ice accretion and water flow on a cold surface. *International Journal of Heat and Mass Transfer*, **47(25)**, pp. 5483 – 5500, 2004.

[48] G.F. & Naterer, Multiphase transport processes of droplet impact and ice accretion on surfaces. *Cold Regions Science and Technology*, **65(1)**, pp. 5 – 12, 2011.

[49] Schepper, S.C.D., Heynderickx, G.J. & Marin, G.B., Modeling the evaporation of a hydrocarbon feedstock in the convection section of a steam cracker. *Computers & Chemical Engineering*, **33(1)**, pp. 122 – 132, 2009.

[50] Alizadehdakhel, A., Rahimi, M. & Alsairafi, A.A., Cfd modeling of flow and heat transfer in a thermosyphon. *International Communications in Heat and Mass Transfer*, **37(3)**, pp. 312 – 318, 2010.

[51] P.Mills, Non-newtonian behaviour of flocculated suspensions. *JPhysLett*, **46**, pp. L301–L309, 1985.

[52] Stevanovic, V.D., Stosic, Z.V. & Stoll, U., Three-dimensional numerical simulation of non-condensables accumulation induced by steam condensation in a non-vented pipeline. *International Journal of Heat and Mass Transfer*, **49(1516)**, pp. 2420 – 2436, 2006.